Synthesis and Surface Modification of Luminescent Nanoparticles
for Imaging and Sensing of Oxygen Using
Near-Infrared Excitation

vorgelegt von

Daniela Eva Achatz
aus Bogen
(Landkreis Straubing-Bogen)
im April 2012

Synthesis and Surface Modification of Luminescent Nanoparticles
for Imaging and Sensing of Oxygen Using
Near-Infrared Excitation

Doctoral Thesis

by

Daniela Eva Achatz

Diese Doktorarbeit entstand in der Zeit von Oktober 2008 bis April 2012 am Institut für Analytische Chemie, Chemo- und Biosensorik an der Universität Regensburg.

Die Arbeit wurde angeleitet von Prof. Dr. Otto S. Wolfbeis.

Promotionsgesuch eingereicht am: April 2012
Kolloquiumstermin: 24.04.2012
Prüfungsausschuss:
Vorsitzender: Prof. Frank-Michael Matysik
Erstgutachter: Prof. Dr. Otto S. Wolfbeis
Zweitgutachter: Prof. Dr. Joachim Wegener
Drittprüfer: Prof. Dr. Achim Göpferich

Danksagung

Table of Contents

1.   Introduction

1.1. Motivation and Aim of Work

In the last three decades, nanomaterials (Greek νᾰνος; Latin nanus: dwarf) have attracted great attention in science and research and also have become part of every day life. The threshold for a particle to be regarded as "nano" is usually set at 100 nm but sometimes the definition is extended to 1000 nm.[1] It is commonly known by now that the self-cleaning or lotus effect of paintings is due to nanoparticles (NPs), just like the whitening effect of toothpaste or the ultraviolet (UV) filter in suntan lotions. There are also discussions whether or not NPs constitute an ecological menace or are hazardous to health as there is a lack of substantial knowledge about risks and possible long-time effects after exposure or incorporation.[2,3] Nevertheless, nanomaterials are considered to offer new possibilities and perhaps solve problems in diverse fields of industry and research.[1]

Gold and other metal NPs were already used in ancient times to color glass or to obtain a glaze on pottery,[4] without knowledge about the scientific background of these effects. In 1857 Michael Faraday described the spectral properties of gold colloids depending on the size of the particles[5] and by the middle of the 20th century it was well known how to produce magnetic fluids[6] and colloidal silica.[7] But it was not before the mid 1980s that nanotechnology as an independent as well as interdisciplinary field of research has gained momentum. At this time instruments like the scanning tunneling microscope[8] and all new particles like fullerenes[9] or semiconductor quantum dots (QDs) were discovered. What renders nanomaterials very attractive is the fact that their physical and chemical properties often differ substantially from the corresponding bulk phases. This is due to their high surface-to-volume ratio and their small dimensions approaching the molecular and atomic level where quantum effects become apparent. Surface atoms exert a dominating influence on the properties of the NPs, the interaction with the surrounding medium

and with other materials. These characteristics allow for new applications in various fields like water treatment and purification,[10,11] cosmetics,[12,13] catalysis,[14] or medicine[15,16] and biology.[17]

Luminescent based techniques have been widely used in bioanalytical research since they are non-invasive, posses a broad dynamic range and allow for very sensitive detection down to femtomolar concentrations. Hence, it is not surprising that especially QDs and upconverting luminescent nanoparticles (UCLNPs) are novel nanomaterials that have attracted great attention in recent years. As already mentioned above, QDs were discovered at the beginning of the 1980s.[18,19] Their unique optical and electrical properties are applied to solar cells,[20] optoelectronics,[21,22] medicine and biology.[23] Their superior brightness and stability compared to conventional organic dyes renders QDs an interesting tool for *in vivo* and *in vitro* imaging, cell-tracking, gene and drug delivery.[23,24] Their emission wavelength can be tuned continuously from UV to near-infrared (NIR) by varying the particle size and a single light source is sufficient for the excitation of these diverse colored QDs. Usually, excitation is realized via UV light but also two-photon excitation (TPE) using a short-pulsed NIR light source is possible.[25] Nevertheless, they suffer from two major drawbacks: fluorescence intermittency and a high cytotoxicity due to the content of heavy metal ions.[26,27] UCLNPs have become available more recently. They have emerged from well known and frequently used rare-earth (RE) doped bulk phosphors and were first synthesized in nanosize about 10 years ago.[28] The optical phenomenon of upconversion luminescence itself has already been known since the 1960's and was discovered independently by Auzel[29,30] and Ovsyankin and Feofilov.[31] It means the emission of anti-Stokes fluorescence in the visible spectral range following excitation in the NIR.[32] Upconversion mainly occurs with RE doped solids, but also with doped transition-metal systems and combinations of both.[33,34] It relies on the sequential absorption of two or more NIR photons by the dopants. The bulk materials have found application in lasers,[35,36] infrared quantum counters,[37] three dimensional

displays,[38] spectral converters for solar cells[39] or physical sensors.[40] One general drawback of the derived nanoscale upconverting crystals is the considerable lower efficiency compared to their bulk counterparts. Nontheless, UCLNPs have found applications in security and brand protection,[41,42] imaging and photodynamic therapy.[43,44,45] Their outstanding features are highly interesting for bioanalytical and biophysical studies. Since photoexcitation of UCLNPs occurs in the NIR, the background fluorescence that often interferes in conventional fluorometry of biological samples is minimized if not zero. Also NIR light penetrates tissue much deeper than more shortwave light, and the laser intensities usually applied do not substantially damage tissue. Unlike conventional fluorophores, they do not suffer from photobleaching at all. Further, the emission bands of UCLNPs are narrow and the color of the emitted light can be tuned by different RE doping ratios.[46,47] Hence, UCLNPs exhibit the advantageous characteristics of QDs but unlike those they do not blink,[26] nor did recent studies reveal a high cytotoxicity.[48,49,50]

Excitation with NIR light is also applied in multi- or two-photon spectroscopy. Upconversion in lanthanide doped solids is based on the sequential absorption of NIR photons and can be achieved using low-cost continuous wave (CW) lasers.[51] In contrast, two-photon excitation (TPE) of chromophores[52] or QDs[25] depends on the almost simultaneous absorption of two coherent photons and can only be accomplished using pulsed lasers in which the photons are packed in short temporal intervals. The effect was first discussed by Goeppert-Mayer in 1931.[53] Kaiser and Garrett experimentally proved this postulate in 1961[54] after invention of the laser that offered the high light intensity needed for TPE. At first it was used for studying excited molecular states[55,56,57] but its combination with laser scanning microscopy[58] led to increased biomedical applications.[59,60] The advantages of two-photon laser scanning microscopy (TPLSM) compared to one-photon laser scanning confocal microscopy (LSCM) are extended sample penetration, less scattering and reduced photodamage

of fluorophores and specimen due to the use of NIR photons as excitation source.[61]

Based on excitation in the NIR, both upconversion and TPE offer the possibility of high contrast imaging, deep tissue penetration,[59,60,62] and a good signal separation in labeling and sensing applications.[62,63] Within this work UCLNPs were provided for labeling, imaging and sensing. Therefore, nanophosphors were synthesized via a co-precipitation method followed by thermal treatment or alternatively a thermal decomposition method. The surface of the UCLNPs was modified via ligand exchange reactions to achieve solubility in various solvents or covered with diverse coatings to enhance brightness and to create multicolor labels with different functionalities. Particles were chosen from this pool and investigated for multicolor imaging of cells and used for the design of the first oxygen sensor based on UCLNPs. Further, the oxygen probe $[Ru(dpp)_3]TMSPS_2$ (ruthenium(II) tris(4,7-diphenyl-1,10-phenanthroline) di(trimethylsilylpropansulfonat))[64] was entrapped in polystyrene nanoparticles (PSNPs) and for the first time applied in direct two-photon absorption (TPA) based oxygen sensing.

1.2. References

1   Cademartiri L, Ozin GA (2009) *Concepts of Nanochemistry.* Wiley-VCH Verlag GmbH & Co. KGaA, Weinheim
2   Nohynek GJ, Dufour EK, Roberts MS (2008) *Nanotechnology, Cosmetics and the Skin: Is There a Health Risk?* Skin Pharmacol Physiol 21:136-149
3   Buzea C, Blandino IIP, Robbie K (2007) *Nanomaterials and nanoparticles: Sources and toxicity.* Biointerphases 2:MR17-MR172
4   Wagner FE, Haslbeck S, Stievano L, Calogero S, Pankhurst QA, Martinek K-P (2000) *Before striking gold in gold-ruby glass.* Nature 407:691-692
5   Faraday M (1857) *The Bakerian Lecture: Experimental Relations of Gold (and Other Metals) to Light.* Philos T Roy Soc 147:145-181
6   Elmore WC (1938) *Ferromagnetic Colloid for Studying Magnetic Structures.* Phys Rev 54:309-310
7   Iler RK (1955) *The colloid chemistry of silica and silicates.* Cornell Univ Pr, Ithaca, NY
8   Binnig G, Rohrer H (1986) *Scanning Tuneling Microscopy.* Surf Sci 126:236-244
9   Kroto HW, Heath JR, O'Brien SC, Curls RF, Smalley RE (1985) *C_{60}: Buckminsterfullerene.* Nature 318:162-163

10 Tiwari DK, Behari J, Sen P (2008) *Application of Nanoparticles in Waste Water Treatment.* World Appl Sci J 3:417-433

11 Theron J, Walker JA, Cloete TE (2008) *Nanotechnology and Water Treatment: Applications and Emerging Opportunities.* Crit Rev Microbiol 34:43-69

12 Müller RH, Radtke M, Wissing SA (2002) *Solid lipid anoparticles (SLN) and nanostructured lipid carriers (NLC) in cosmetic and dermatological preparations.* Adv Drug Deliver Rev 54:S131-S155

13 Wissing SA, Müller RH (2003) *Cosmetic applications for solid lipid nanoparticles (SLN).* Int J Pharm 254:65-68

14 Astruc D, Lu F, Aranzaes JR (2005) *Nanoparticles as Recyclable Catalysts: The Frontier between Homogeneous and Heterogeneous Catalysis.* Angew Chem Int Ed 44:7852-7872

15 Sanvicens N, Marco MP (2008) *Multifunctional nanoparticles-properties and prospects for their use in human medicine.* Trends Biotechnol 26:425-433

16 Zhang L, Gu FX, Chan JM, Wang AZ, Langer RS, Farokhzad OC (2008) *Nanoparticles in Medicine: Therapeutic Applications and Developments.* Clin Pharmacol Ther 83:761-769

17 Salata OV (2004) *Applications of nanoparticles in biology and medicine.* J Nanobiotechnol 2:3-8

18 Ekimov AI, Onushchenko AA (1981) *Quantum size effect in three-dimensional microscopic semiconductor crystals.* JETP Lett 34:345-349

19 Rossetti R, Brus L (1982) *Electron-Hole Recombination Emission as a Probe of Surface Chemistry in Aqueous CdS Colloids.* J Phys Chem 86:4470-4472

20 Nozik AJ (2002) *Quantum dot solar cells.* Physica E 14:115-120

21 Coe-Sullivan S (2009) *Optoelectronics: Quantum dot developments.* Nat Photonics 3:315-316

22 Bhattacharya P, Ghosh S, Stiff-Roberts AD (2004) *Quantum Dot Opto-Electronic Devices.* Annu Rev Mater Res 34:1-40

23 Bailey RE, Smith AM, Nie S (2004) *Quantum dots in biology and medicine.* Physica E 25:1-12

24 Michalet X, Pinaud FF, Bentolila LA, Tsay JM, Doose S, Li JJ, Sundaresan G, Wu AM, Gambhir SS, Weiss S (2005) *Quantum Dots for Live Cells, In Vivo Imaging, and Diagnostics.* Science 307:538-544

25 Larson DR, Zipfel WR, Williams RM, Clark SW, Bruchez MP, Wise FW, Webb WW (2003) *Water-Soluble Quantum Dots for Multiphoton Fluorescence Imaging In Vivo.* Science 300:1434-1436

26 Nirmal N, Dabbousi BO, Bawendi MG, Macklin JJ, Trautman JK, Harris TD, Brus LE (1996) *Fluorescence intermittency in single cadmium selenide nanocrystals.* Nature 383: 802-804

27 Hardman R (2006) *A Toxicologic Review of Quantum Dots: Toxicity Depends on Physicochemical and Environmental Factors.* Environ Health Persp 114:165-172

28 Tessari G, Bettinelli M, Speghini A, Ajò D, Pozza G, Depero LE, Allieri BG, Sangaletti L (1999) *Synthesis and optical properties of nanosized powders: lanthanide-doped Y_2O_3.* Appl Surf Sci 144-145:686-689

29 Auzel F (1966) *Computeur quantique part transfer d'energie de Yb^{3+} and Tm^{3+} dans un tungstate mixte et dans un verre germanate.* CR Acad Sci 262:1016-1017

30 Auzel F (1966) *Stimulated emission of Er1s in a fluorophosphate glass.* CR Acad Sci 263B: 819-820

31 Ovsyankin V, Feofilov PP(1966*) Mechanism of Summation of Electronic Excitations in Activated Crystals.* JETP Lett 3:322-323

32 Auzel F (2004) *Upconversion and Anti-Stokes Processes with f and d Ions in Solids.* Chem Rev 104:139-173

33 Suyver JF, Aebischer A, Biner D, Gerner P, Grimm J, Heer S, Krämer KW, Reinhard C, Güdel HU (2005) *Novel materials doped with trivalent lanthanides and transition metal ions showing near-infrared to visible photon upconversion.* Opt Mater 27:1111-1130

34 Gamelin DR, Güdel HU (2001) *Upconversion Processes in Transition Metal and Rare Earth Metal Systems.* Top Curr Chem, Springer-Verlag, Berlin, Heidelberg, Vol. 214:1-56

35 Johnson LF, Guggenheim HJ (1971) *Infrared-Pumped Visible Laser.* Appl Phys Lett 19:44-47

36 Joubert MF (1999) *Photon avalanche upconversion in rare earth laser materials.* Opt Mater 11:181-203

37 Brown MR, Shand WA (1964) *Infrared Quantum Counter Action in Er-Doped Fluoride Lattices.* Phys Rev Lett 12:367-369

38 Rapaport A, Milliez J, Bass M, Cassanho A, Jenssen H (2006) *Review of the Properties of Up-Conversion Phosphors for New Emissive Displays.* J Display Technol 2:68-79

39   Van der Ende BM, Aarts L, Meijerink A (2009) *Lanthanide Ions as Spectral Converters for Solar Cells.* Phys Chem Chem Phys 11:11081-11095

40   Berthou H, Jörgensen CK (1990) *Optical-fiber temperature sensor based on upconversion-excited fluorescence.* Optics Letters 15:1100-1102

41   Muth O, Brockmann H, Schmidt W, Bailleu A, Brauer G, Paeschke M, Ahlers B, Franz-Burgholz A, Zerbel H (2002) Eur. Pat. 1.241.021

42   Kim WJ, Nyk M, Prasad PN (2009) *Color-coded multilayer photopatterned microstruc-tures using lanthanide(III) ion co-doped NaYF$_4$ nanoparticles with upconversion luminescence for possible applications in security.* Nanotechnology 20:185301-185307

43   Chatterjee DK, Fong LS, Zhang Y (2008) *Nanoparticles in photodynamic therapy: an emerging paradigm.* Adv Drug Deliver Rev 60:1627-1637

44   Bechet D, Couleaud P, Frochot C, Viriot ML, Guillemin F, Barberi-Heyob M (2008) *Nanoparticles as vehicles for delivery of photodynamic therapy agents.* Trends Biotechnol 26:612-621

45   Wang F, Banerjee D, Liu Y, Chen X, Liu X (2010) *Upconversion nanoparticles in biological labeling, imaging, and therapy.* Analyst 135:1839-1854

46   Wang F, Liu X (2008) Upconversion Multicolor *Fine-Tuning: Visible to Near-Infrared Emission from Lanthanide-Doped NaYF$_4$ Nanoparticles.* J Am Chem Soc 130:5642-5643

47   Chen G, Liu H, Somesfalean G, Liang H, Zhang Z (2009) *Upconversion emission tuning from green to red in Yb^{3+}/Ho^{3+}-codoped NaYF$_4$ nanocrystals by tridoping with Ce^{3+} ions.* Nanotechnology 20:1-6

48   Hilderbrand SA, Shao F, Salthouse C, Mahmood U, Weissleder R (2009) *Upconverting luminescent nanomaterials: application to in vivo bioimaging.* Chem Comm: 4188-4190

49   Xiong L, Yang T, Yang Y, Xu C, Li F (2010) *Long-term in vivo biodistribution imaging and toxicity of polyacrylic acid-coated upconversion nanophosphors.* Biomaterials 31:7078-7085

50   Wang M, Mi CC, Wang WX, Liu CH, Wu YF, Xu ZR, Mao CB, Xu SK (2009*) Immunolabeling and NIR-Excited Fluorescent Imaging of HeLa Cells by Using NaYF$_4$:Yb,Er Upconversion Nanoparticles.* ACS Nano 3:1580-1586

51   Li Z, Zhang Y, Jiang S (2008) *Multicolor Core/Shell-Structured Upconversion Fluorescent Nanoparticles.* Adv Mater 20:4765-4769

52   Bestvater F, Spiess E, Stobrawa G, Hacker M, Feurer T, Porlow T, Berchner-Pfannschmidt U, Wotzlaw C, Acker H (2002) *Two-photon fluorescence absorption and emission spectra of dyes relevant for cell imaging.* J Microsc 208:108-115

53   Goeppert-Mayer M (2009) *Elementary processes with two quantum transitions.* Ann Phys (Berlin) 18:466-479

54   Kaiser W, Garrett CGB (1961) *Two-Photon Excitation in CaF$_2$:Eu^{2+}.* Phys Rev Lett 7:229-231

55   Friedrich DM (1982) *Two-photon molecular spectroscopy.* J Chem Educ 59:472-481

56   Goodman L, Rava RP (1984) *Two-photon spectra of aromatic molecules.* Acc Chem Res 17:250-257

57   Castellano FN, Malak H, Gryczynski I, Lakowicz JR (1997) *Creation of Metal-to-Ligand Charge Transfer Excited States* Inorg Chem 36:5548-5551

58   Denk W, Strickler JH, Webb WW (1990) *Two-Photon Laser Scanning Fluorescence Microscopy.* Science 248:73-76

59   Piston DW (1999) *Imaging living cells and tissues by two-photon excitation microscopy.* Trends Cell Biol 9:66-69

60   Levi V, Ruan Q, Gratton E (2005) *3-D Particle Tracking in a Two-Photon Microscope: Applications to the Study of Molecular Dynamics in Cells.* Biophys J 88:2919-2928

61   Denk W, Svoboda K (1997) *Photon Upmanship: Why Multiphoton Imaging is More than a Gimmick.* Neuron 18:351-357

62   Mader HS, Kele P, Saleh SM, Wolfbeis OS (2010) *Upconverting luminescent nanoparticles for bioconjugation and bioimaging.* Curr Opin Chem Biol 14:582-596

63   Achatz DE, Ali R, Wolfbeis OS (2011) *Luminescent Chemical Sensing, Biosensing and Screening using Upconverting Nanoparticles.* Top Curr Chem, Springer-Verlag, Berlin, Heidelberg, Vol. 300:29-50

64   Klimant I, Wolfbeis OS (1995) *Oxygen-Sensitive Luminescent Materials Based on Silicone-Soluble Ruthenium Diimine Complexes.* Anal Chem 67:3160-3166

2. Fundamentals

2.1. Upconverting Luminescent Nanoparticles

2.1.1. Mechanism of Photonic Upconversion

Lanthanide ions Ln^{3+} posses a $[Xe]4f^n$ (n = 0-14) electronic configuration. Their 4f electrons are shielded by filled $5s^2 5p^6$ atomic orbitals reducing external interactions and mixing with surrounding orbitals in a chemical environment. According to the *Laporte's parity selection rule* 4f-4f electron transitions are forbidden. Despite the shielding of the 4f orbitals, a ligand field or a crystal lattice acts as a small perturbation. This makes the transition partially allowed, i.e. there is a low probability for it. The results are long-living narrow emission bands which exhibit only weak intensities when the lanthanide ions are excited directly. The emission intensity can be increased by coupling the ions with a sensitizer and exploiting an "antenna effect" for energy transfer to the emitting lanthanides.[1] The three main processes causing upconversion emission in RE doped materials are excited state absorption (ESA), energy transfer upconversion (ETU), and photon avalanche (PA). All these processes are based on the sequential absorption of two or more NIR photons by the dopants. The energy is stored in existing intermediate levels and the combined energies of the pump photons prompt the emission of higher energy light i.e. in the VIS spectral range.[2,3,4]

ESA occurs in one single ion that successively absorbs two photons (Figure 2.1a). The first absorption process occurs at the energetic ground state (G) and is induced by a resonant photon (ground state absorption/ GSA). It leads to the population of the metastable and long-living level E1. The second resonant absorption promotes the ion from E1 to the higher level E2, from which the emission corresponding to the transition E2 → G occurs.

The principle of ETU is similar, but an energy transfer between two adjacent ions is involved (Figure 2.1b). Both ions are excited via GSA to

their E1 level. Subsequently, the excited state energy from one ion is transmitted to another one in close proximity by resonant energy transfer. The donor ion relaxes to its ground state G while the acceptor ion is promoted to the excited state E2. This is again followed by an emissive transition E2 → G.

The third process (PA) is based on an unconventional mechanism that occurs only when a critical excitation power is exceeded. In the first step, weak non-resonant GSA occurs in many ions, followed by a resonant ESA at one ion which thus is promoted to energy level E2 (Figure 2.1c). A cross-relaxation energy transfer to an adjoining ion in its ground state results in both ions occupying E1. The "avalanche" effect is caused by further resonant ESA and cross-relaxation energy transfers that exponentially increase the population of E2 and therefore upconversion emission intensity.
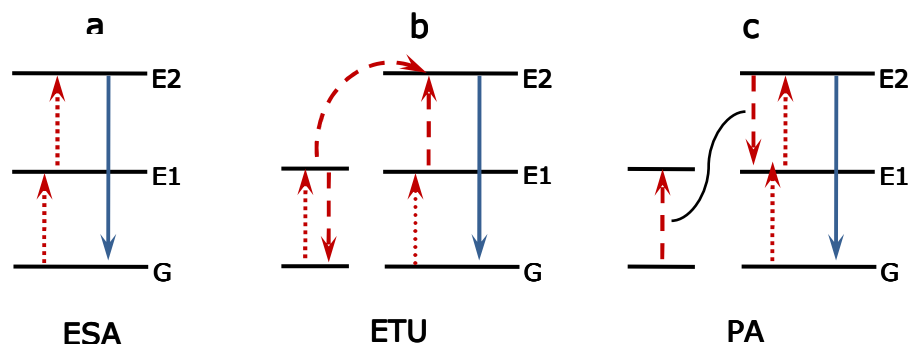
Figure 2.1: Schematic representation of the three main processes causing upconversion in rare earth doped materials. (a) Excited state absorption; (b) energy transfer upconversion; (c) photon avalanche. The dotted lines refer to photon excitation, dashed lines to non-radiative energy transfer, and full arrows to emissive processes, respectively.

The upconversion efficiency achievable by the three processes varies strongly. ESA generates the weakest emission due to the reasons stated above. ETU and PA utilize sensitization resulting in a higher efficiency. PA is the most efficient process but depends on the pump power and has a slow (up to several seconds) response to excitation due to the ESA and cross-relaxation looping cycles. ETU is independent of pump power and occurs without delay after excitation. [1-4]

2.1.2. Materials

Generally, upconverting phosphors are composed of an inert host lattice doped with lanthanide ions (Ln^{3+}). Essential requirements for the host material are chemical stability and low phonon energies to avoid a loss in efficiency via non-radiative energy transfer. Besides glasses (bulk or fibre),[5,6,7] upconversion emission of lanthanide ions is observed in oxides of zirconium and titanium, the fluorides, oxides, phosphates, oxysulfates and oxyfluorides of the trivalent lanthanides (Ln^{3+}), and similar compounds that additionally may contain alkaline earth ions.[4,8] $NaYF_4$ is the host material regarded as one of the most efficient lattices both for bulk phosphors and nanocrystals.[3,9] This is due to the generally low phonon energies in fluorides (~ 350 cm^{-1} opposed to > 500 cm^{-1} in oxides for example) and the similar ion radii of Na^+, Y^{3+}, and Ln^{3+} causing less crystal defects upon doping. These qualities reduce non-radiative relaxation and hence promote efficient upconversion.[10] It has to be distinguished between the cubic (α-$NaYF_4$) and the hexagonal (β-$NaYF_4$) modification, whereas upconversion efficiency is found to be about one order of magnitude higher in doped hexagonal phase $NaYF_4$.[11,12] Besides $NaYF_4$ the very similar $NaGdF_4$ is a frequently used host material. It exhibits the same qualities for efficient upconversion but by exchanging Y^{3+} for paramagnetic Gd^{3+} the particles can simultaneously act as contrast agent in magnetic resonance imaging.[13,14]

The crystal lattice mainly determines the position of the emitting dopants and their spatial arrangement. The impact on the 4f orbitals of enclosed lanthanides is rather low due to shielding by the filled 5s and 5p orbitals. This results in a low energy splitting of the 4f orbitals and ladder-like energy levels with small energy gaps. Thus, absorption of more than one photon from a single monochromatic light source at comparatively low excitation densities via long-living metastable energy levels is possible.[4,10] Consequently, the color of the emitted light for a certain ion is distinct and largely independent of the host lattice. The energy levels for RE ions in crystals were first published in 1968 in the form of what is now known as

"Dieke diagram".[15] Very common emitters (also called activators) are Er^{3+}, Tm^{3+}, and Ho^{3+}. In single-doped host lattices upconversion is mostly accomplished by ESA (Figure 2.1a) which is the least efficient of the processes described above. In principle, emission in such systems can be enhanced by increasing the amount of activator ions. Yet, above a critical concentration (up to 3% for Er^{3+}/ Ho^{3+}, 0.5% for Tm^{3+})[10] there is also a bias towards non-radiative cross-relaxation between the dopants. A good alternative is co-doping with a second lanthanide, a so-called sensitizer, which is used to exploit the more efficient processes ETU and PA (Figure 2.1b, c). This significantly increases the upconversion efficiency as stated above.
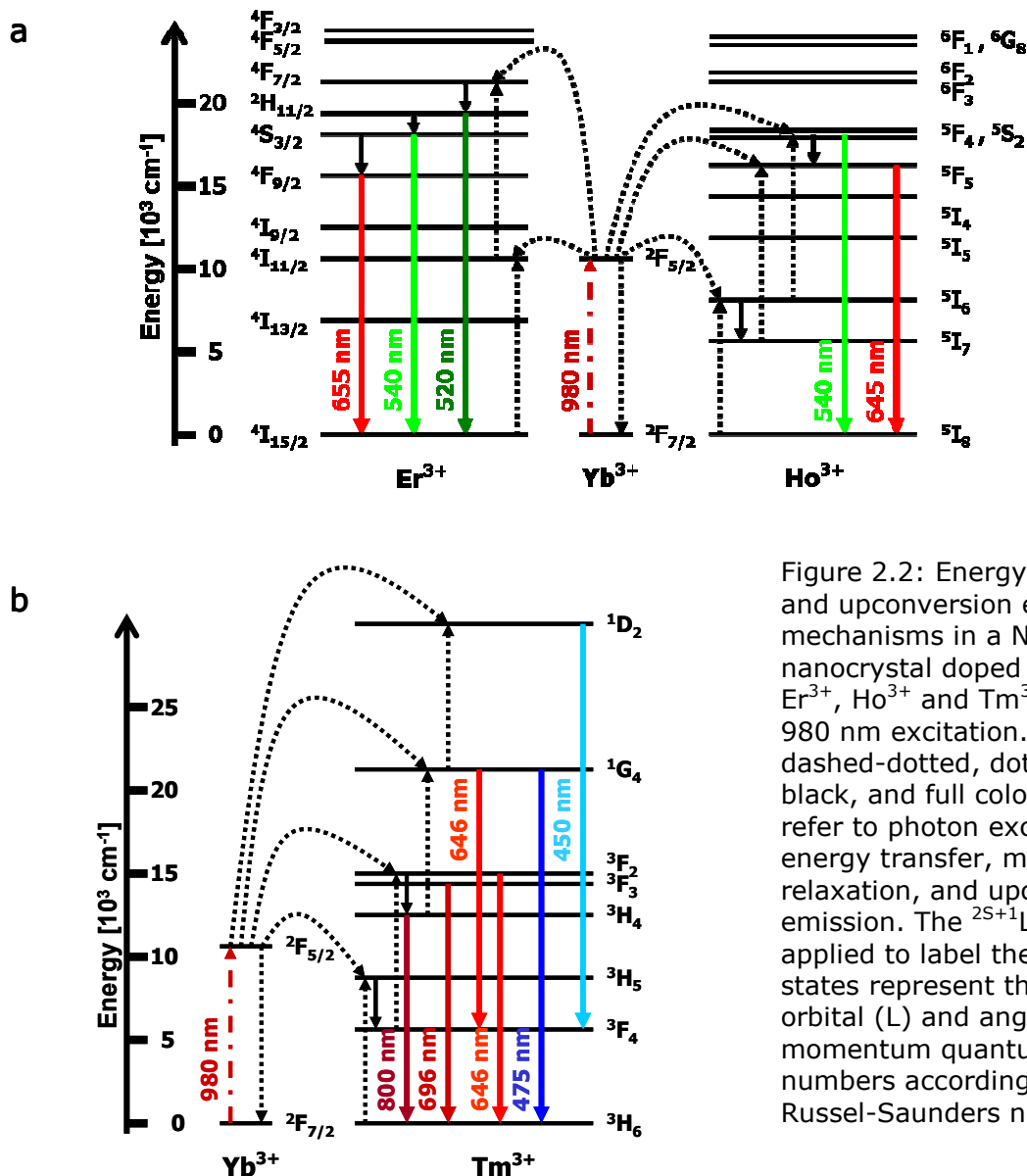
Figure 2.2: Energy transfer and upconversion emission mechanisms in a NaYF$_4$ nanocrystal doped with Yb^{3+}, Er^{3+}, Ho^{3+} and Tm^{3+} under 980 nm excitation. The dashed-dotted, dotted, full black, and full colored arrows refer to photon excitation, energy transfer, multi-photon relaxation, and upconversion emission. The $^{2S+1}L_J$ notation applied to label the f energy states represent the spin (S), orbital (L) and angular (J) momentum quantum numbers according to the Russel-Saunders notation.

Yb^{3+} is a common sensitizer ion since it has a high absorption cross-section and only one excited 4f state. This level is well resonant with the 4f-4f transitions of Er^{3+}, Tm^{3+} or Ho^{3+}. The sensitizer itself contributes no visible emission to the overall spectrum. Figure 2.2 displays the energy levels of Yb^{3+}, Er^{3+}, Ho^{3+} and Tm^{3+} according to the Russel-Saunders notation. The upconversion emissions resulting from the energy transfers of Yb^{3+} to Er^{3+}/ Ho^{3+} (Figure 2.2a) or Tm^{3+} (Figure 2.2b) are shown. The absorption band of the sensitizer around 980 nm is promoting the transition $^{2}F_{7/2} \rightarrow {}^{2}F_{5/2}$. After energy transfer to the activator ions, Er^{3+} and Ho^{3+} exhibit very similar emission spectra with peaks in the green and red region of the visible spectrum. The transitions $^{2}H_{11/2} \rightarrow {}^{4}I_{15/2}$, $^{4}S_{3/2} \rightarrow {}^{4}I_{15/2}$ and $^{4}F_{9/2} \rightarrow {}^{4}I_{15/2}$ in Er^{3+} promote photon emission with a wavelength of around 520, 540 and 655 nm. Ho^{3+} emits green light at 540 nm ($^{5}F_{4}/ {}^{5}S_{2} \rightarrow {}^{5}I_{8}$) and red light at 645 nm ($^{5}F_{5} \rightarrow {}^{5}I_{8}$). Tm^{3+} yields two peaks in the blue and two peaks in the red region of the VIS spectrum. This can be assigned to the transition $^{1}D_{2} \rightarrow {}^{3}F_{4}$ (450 nm) and relaxation from the energy levels $^{1}G_{4}$ (475 nm), $^{3}F_{2}$ (646 nm) and $^{3}F_{3}$ (696 nm) to the ground state level $^{3}H_{5}$. The energy of a further transition from $^{1}G_{4}$ to $^{3}F_{4}$ corresponds to $^{3}F_{2} \rightarrow {}^{3}H_{5}$ and results in no additional peak. Another relaxation from the energy level $^{3}H_{4}$ to the ground state results in emission of NIR light (800 nm) rendering Tm^{3+} an efficient NIR-to-NIR upconverter.[4,16,17,18]

2.2. Fluorescence Imaging

Imaging is used to visualize ions, molecules, organelle or whole cells (*in vitro* and *in vivo*), small animals or even human bodys. There are several imaging techniques (e.g. magnetic resonance imaging, x-ray computed imaging, nuclear tomography, optical imaging) that all rely on the interaction of different forms of energy with the object of interest resulting in a certain contrast on the macroscopic or molecular level. Historically, conventional or structural imaging enabled only a vague view of the

anatomy. New instrumentation and microscopic techniques in combination with novel imaging agents allowed for a higher resolution. This led to functional imaging and finally to molecular imaging for the visualization of even single molecules.[19] Molecular imaging allows for investigations on protein function, gene-expression, metabolism, protein-protein interactions and other cellular processes preferably *in vivo* with non-invasive methods. It has been used in genomics, proteomics, biological research, drug discovery and development. It offers the possibility to detect abnormalities caused by disease or treatment effects on an earlier molecular stage instead of a mere look at the eventual effects.[20,21] In particular optical techniques based on fluorescence and bioluminescence offer advantages like versatility, comparatively low-cost equipment, non-invasive measurements, high sensitivity, potential multiplexing and high spatial and temporal resolution.[22,23]

2.2.1. Two-Photon Excitation

TPE or multiphoton excitation in general can be compared to photon upconversion. Both processes are based on the absorption of two (or more) NIR photons followed by emission in the VIS spectral range. The fundamental difference is that in upconversion processes photons are absorbed sequentially via real intermediate levels having a certain lifetime. For TPE, in contrast, the absorptions have to proceed nearly simultaneous ($\sim 10^{-16}$ s).[24] Figure 2.3 displays schemes of conventional (one-photon) absorption (A), two-photon absorption (TPA) and upconversion (UC). The requirement of close, ladder like energy levels for upconversion is almost exclusively met by lanthanide ions. In contrast, TPE is possible for most molecules that can be excited by UV or VIS light at approximately twice of their one-photon absorption maximum. The transition probability for this process is extremely low at conventional light intensities. It will only occur when the excitation light is concentrated in space and time like it is realized with short-pulsed, focused laser

beams.[25,26] Nevertheless, TPA cross-sections of most fluorophores are very small.[26]
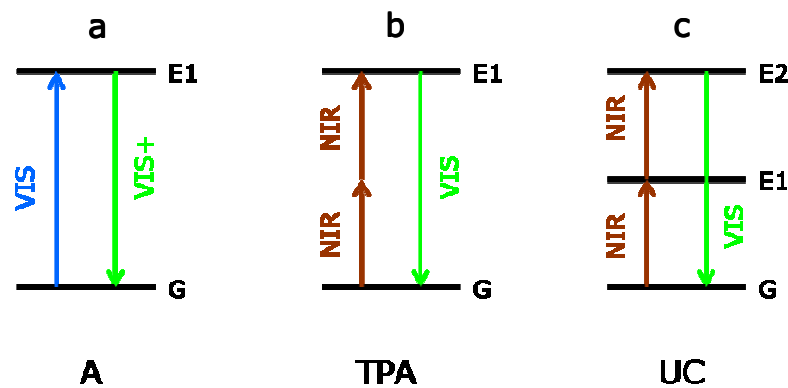
Figure 2.3: Schematic representation of conventional one-photon excitation by VIS light (a), TPA of NIR light (b), and a general UC process (c) all resulting in emission in the VIS spectral range. Upon one-photon excitation the emission is long-wave shifted (Stokes shift), whereas it is short-wave shifted for TPA and UC (anti-Stokes shift).

Especially in microscopy TPE has attracted enormous attention (TPLSM). Generally light microscopy offers high spatial resolution, yet it is limited by the wavelength of light (Abbe's limit). In addition, the resolution is degraded by scattering in tissue which worsens with deeper penetration. In LSCM high resolution is achieved first by illumination with a focussed CW laser beam (UV to VIS) that is raster scanned over the sample. Secondly, the emission is collected via a detector pinhole which rejects out-of-focus and scattered light. This is, at the same time, the major drawback since a large part of excitation light is wasted. The increase in excitation intensity required for compensation often leads to photobleaching and photodamage.[25] TPLSM in contrast is less sensitive to scattering since short-pulsed red or NIR light is used for illumination. Further, excitation is confined to the laser focus. There the photon density necessary for TPE is achieved resulting in three-dimensional contrast and resolution without further elements in the detection path like the pinhole in confocal microscopy. All luminescent photons contribute to the signal once they are collected by the objective. Additional advantages lie in the clear separation of emission and excitation light due to the anti-Stokes shift and reduced photodamage of the specimen. [25,27]

2.2.2. Labels and Agents for Conventional Optical Imaging

When choosing luminescent reporters, a thoughtful consideration of size, biocompatibility and interaction with the biological unit is required. Brightness, photostability and metabolic stability, excitation at wavelength where biological background fluorescence is low, solubility in relevant solvents (buffer, water) and functional groups for site-specific labeling constitute further requirements.[28,29] There are several different types of chromophores for optical imaging including organic dyes, metal-ligand complexes, lanthanide chelates, fluorescent proteins and luminescent NPss which will be discussed briefly regarding their assets and drawbacks in the following sections.

Organic Fluorophores

Classical labels and probes are organic fluorophores which feature the advantages of small size and well known chemistry for synthesis and conjugation to target molecules. Nevertheless, they suffer from numerous limitations. They exhibit broad emission bands and a small Stokes shift and usually require discrete excitation in the VIS spectral range. It is difficult to image different dyes simultaneously since multiple wavelengths for excitation limit the spectral range of emission collection. Additionally, the emission bands of different fluorophores overlap with each other and with the autofluorescence of the sample originating from the excitation light. Photobleaching of the fluorophore and potential phototoxicity constitute other drawbacks.[30,31]

Fluorescent Proteins

Fluorescent proteins have attracted great interest since the green fluorescent protein (GFP) was first isolated from the jellyfish *Aequorea victoria* in 1961.[32] Meanwhile related proteins have become available that emit various colors. They are very convinient for simultaneous indication of different genetic expression levels in living organism. They can be introduced in a wide variety of tissues in intact organism, they can be designed to respond to many biological events and exhibit good

biocompatibility with low phototoxicity.[33,34] Fluorescent proteins share most photophysical properties with organic dyes and hence are subject to the same limitations.[31]

Metal-Ligand Complexes and Lanthanide Chelates

Metal-ligand complexes[35,36] and lanthanide chelates[37,38,39,40] are advantageous due to narrow emission bands, larger Stokes shifts (compared to conventional organic dyes or fluorescent proteins) and long luminescent lifetimes. This allows for better signal separation and increased sensitivity in time-resolved measurements since the short-lived background fluorescence can be eliminated. Nevertheless, they are also prone to photobleaching like conventional fluorophores. In addition, desorption of metal or lanthanide ions needs to be taken into consideration due to high cytotoxicity.[35,39]

Luminescent Nanoparticles

NP reporters can offer some advantages compared to the chromophores described so far. Highly fluorescent labels can be generated by physical entrapment in or covalent linkage of classical labels to inert materials, typically by encapsulation of organic dyes or lanthanide chelates in silica[41,42] or polymer NPs.[43,44] Controlled loading of the particles with luminescent molecules (taking into account self quenching and energy transfer) enhances brightness as opposed to single chromophores, reduces quenching effects by the solvent, and increases their stability by shielding off the environment.[42] Fine tuning of the photophysical characteristics can be realized by encapsulating multiple different dye molecules[45,46] or by growing a metal shell on the particle surface.[42] Hybrid materials based on physical entrapment more often suffer from dye leakage and are less protective against quenching and photobleaching compared to those generated by covalent binding.[31]

Semiconductor QDs are a material for optical imaging that is not based on classical labels. They are often considered candidates for the replacement of classical chromophores in fluorescence labeling and

imaging. They do not suffer from photobleaching and can be excited in a very broad region spanning from UV to VIS light resulting in bright and narrowband emission. Further, the wavelengths of these peaks can be continuously tuned by varying the particle size leading to multicolor labels excitable at a single wavelength.[23,24,25] The main drawbacks of QDs are blinking and their potential toxicity.[25,26] Moreover, targeted imaging with QDs and NPs in general is more complicated compared to conventional fluorophores since there is still a lack of standardized protocols for surface modification, labeling and purification procedures.[28]

2.2.3. Labels and Agents for Near-Infrared Optical Imaging

All the labels and probes discussed above are conventionally excited via UV or VIS light. Especially for *in vivo* applications the penetration depth of short wave light in tissue is a limiting factor. TPE of these imaging agents[25,47,48,49] with short-pulsed NIR light can avert some limitations and the required penetration depth for the investigation of intact brain for example is met.[50] Photodamage of the specimen and the fluorophore is also reduced.[24] In the early years of two-photon microscopy the lack of knowledge about the optical two-photon characteristics of imaging agents was unfavorable but meanwhile TPA cross-sections, absorption and emission spectra from numerous "conventional" fluorophores have become available.[25,49,52] Further, there are continuous efforts to synthesize chromophores with large TPA cross-sections.[51,52,53] Aside from residual disadvantages like broad emission bands and metabolic degredation,[29] the main drawback of TPE is the need for expensive instrumentation.

UCLNPs constitute a promising alternative. Their advantageous optical properties like brightness, chemical and photochemical stability, narrow emission bands, and the possibility of excitation in the NIR with low-cost CW lasers renders them ideal candidates for optical molecular imaging *in vivo*.[31] First QDs have attracted interest as labels and optical imaging agents in medicine and biology.[24,25,54] But UCLNPs are about to

become the material of choice as they exhibit no blinking nor a high cytotoxicity and there is no need for expensive short-pulsed laser excitation.[48,62,55] However, common synthetic procedures provide UCLNPs without functionalities on the particle surface and often poor dispersibilty in aqueous solvents. Hence, it is a challenging objective to render them suitable reporters in optical imaging by surface modification for improved dispersibility and further bioconjugation.[45,62]

2.3. Optical Chemical Sensors

2.3.1. Definition and Classification

There exist several definitions for sensors. The formal definition by the IUPAC states:

"A chemical sensor is a device that transforms chemical information, ranging from the concentration of a single sample component to total composition analysis, into an analytical useful signal. The chemical information, mentioned above, may originate from a chemical reaction of the analyte or from a physical property of the system investigated."[56]

The so called Cambridge definition offers a somewhat more detailed description :

"Chemical sensors are miniaturized devices that can deliver real-time and on-line information on the presence of specific compounds or ions in complex samples."[57]

Chemical sensors are comprised of at least two functionalities connected in series: a *receptor* transforms the chemical information into a signal that can be measured by the *transducer* which in turn converts the signal into an electrical signal.[56] They further contain units for signal amplification, preprocessing and evaluation as well. Other definitions include more specific details like fast response, selectivity, operational and storage

stability and the very common criterion of continuous and reversible measurements. In fact, devices for single shot testing without continuous monitoring of the signal are more precisely called "probes" instead of sensors. Similar definitions do exist for biosensors in which a biological component acts as the receptor.[58] Especially for biosensors the requirement of reversibility is not always met as binding constants are very high.[59]

Sensors are classified with respect to the operating principle of the transducer into optical, electrochemical, electrical, mass sensitive, magnetic, thermometric or other devices.[56] In particular optical chemical sensors[60,61,62] and optical biosensors[58,60] for various analytes have become successful in recent decades. This is due to progress in optics, instrumentation and fluorescence spectroscopy.[62] Especially the coupling to novel optical fibers prompted their development. They are often referred to as optrodes (in analogy to electrodes) or optodes (Greek: optical path). Opt(r)odes generate a signal upon changes in reflectivity, refractive index, absorbance or luminescence (intensity and lifetime). They posses several advantages over traditional sensing systems like resistance to electrical and electromagnetic interference, potential miniaturization, high sensitivity, internal referencing or the opportunity of multiplexed sensing. Nevertheless, they are prone to interferences from ambient or scattered excitation light, they have a limited dynamic range and the operational stability may be restricted due to photobleaching or dye leakage.[61,63]

2.3.2. Sensors for Oxygen

An analyte that is of particular interest in sensor technology is oxygen. It is ubiquitous in nature and essential for almost all living systems. Hence, it is of enormous significance in areas such as biology,[64] medicine,[65] chemical process monitoring,[66] and food science,[67] to mention only a few. Methods for measuring oxygen in the gas phase are gas chromatography,

mass spectrometry, paramagnetic methods or solid state electrodes. The latter has become one of the most successful chemical sensors nowadays. It is better known as lambda sensor measuring the oxygen partial pressure (pO_2) in the exhaust gas of all modern vehicles.[68] Dissolved oxygen in water is mainly determined by the Winkler test[69] or its photometric modifications[70,71] in which on-line monitoring is not possible. A widely used amperometric method for continuous oxygen sensing is the Clark electrode[72] that is based on the reduction of oxygen on the cathode. It allows for measurements over several orders of magnitude down to the lower ppm range without extensive calibration. The main drawbacks of such membrane coated electrodes are demanding miniaturization, susceptibility to electrical interference, the consumption of oxygen at the interface and covering of the membrane by proteins resulting in misleading data.[73] Stirring of the sample is necessary and hence especially *in vivo* applications are complicated.

2.3.3. Optical Oxygen Sensing

In the 1930's Kautsky and Hirsch first recognized the reversible quenching effect of oxygen on the luminescence of certain dye molecules.[74,75] That provided the base for optical oxygen sensing. The quenching effect relies on collision quenching occurring between triplet oxygen ($^3O_2$) and probe molecules in their excited triplet state. The excitation energy is transferred to oxygen without radiation resulting in singlet oxygen ($^1O_2$), a loss in the signal intensity and a shorter lifetime of the luminescence.[73] Hence, unlike the amperometric methods described above optical methods for sensing oxygen do not consume the analyte. Oxygen sensing based on phosphorescence or lifetime quenching is versatile and applications include aerodynamic investigations in wind tunnels,[76] measurement of biological oxygen demand,[77] monitoring of oxygen during fermentation processes,[78,79] in blood,[80,81] tissues[82] or cells.[83,84]

A variety of molecules like organic dyes, transition metal complexes, metalloporphyrins or fullerenes are susceptible to quenching by oxygen. [73] These probes are usually incorporated in gas-permeable polymer matrices for further use as foils and paints,[85] fiber optics,[60] or in micro- and NPs.[86,87,88] Both the characteristics of the oxygen sensitive molecule and the polymer matrix determine the properties of the sensor. Powerful oxygen probes are required, to exhibit several characteristics like a sufficient quenching rate and efficiency, good photostability, brightness and long luminescence lifetimes. Additionally, excitation by simple and affordable light sources like diode lasers is desired.[89,90] Metal-ligand complexes of transition metals (e.g. Ru(II), Os(II), Ir(III)) with mainly polypyridines (2,2'-bipyridyl, 1,10-phenanthroline, 4,7-diphenyl-1,10-phe-nanthroline)[91,92,93] or coumarin derivatives[94,95] and metalloporphyrins of Pt(II) and Pd(II)[91,96] are the classes of oxygen probes that were found to be particularly useful since they meet most of the criteria mentioned above.

The transition-metal complexes exhibit high quantum yields, quite long luminescence lifetimes up to several microseconds, good photostability and the indicators are excitable by UV or blue VIS light.[97] They posses a high Stokes shift allowing for good signal separation of excitation and emission but unfortunately the emission bands are very broad. This is a limiting factor for multiple sensing applications.[89,91,98,99] Further, the high cross-sensitivity of these probes to temperature has to be taken into account.

The Pt(II) and Pd(II) metalloporphyrins display oxygen sensitive phosphorescence at room temperature after excitation in the near UV and VIS region.[89] They offer moderate quantum yields and lifetimes up to 1 millisecond resulting in a very good quenching efficiency.[96] Relatively narrow emission bands allow for a good signal separation[99] and the fluorinated derivatives exhibit excellent photostability.[89]

2.3.4. State of the Art in Near-Infrared Based Optical Sensing

Optical sensing approaches for various analytes make use of absorption in the UV or VIS spectral range, whereas only a few are based on NIR excitation. Sensor probes and sensing applications based on TPE are described for fluoride,[100] cysteine/ homocysteine,[101,102] and metal ions,[103,104,105,106] especially calcium.[107,108] Two-photon induced oxygen sensing is limited to few experiments that are all based on an energy transfer from a sensitizer to oxygen sensitive metal-ligand complexes. The workgroup of Vinogradov created a nanosensor for oxygen by combining two-photon absorbing antennae and platinum(II) porphyrins[109,110,111] which they used for two-photon imaging of oxygen in cells.[112] Wu et al. described a similar combination of platinum(II) porphyrins with a conjugated polymer and proposed the use of these NPs as oxygen sensors in biological two-photon-based imaging.[113] Further, an energy transfer from two-photon absorbing nanocrystals to a osmium(II) polypyridyl complex in a nanoconjugate was recommended as internally referenced sensor by McLaurin et al.[114]

Sensors based on UCLNPs are rare. On the one hand this might be due to their novelty but there is also a lack of standardized protocols for reproducible preparation, coating and functionalization. The NIR excited upconversion is intrinsically dependent on temperature rendering them useful tools in thermometry.[115] Vetrone et al. demonstrated their applicability as temperature nanosensors inside living cells.[116] Further, the dependency of ligand-free UCLNPs on pH due to surface quenching effects[117] and dynamic quenching by heavy metal ions was observed.[118] Few UCLNP-based biosensors for oligonucleotides,[119,120,121,122] proteins,[123] ligand-receptor interactions[124,125] and enzyme activity[126] have been presented. Kumar et al. used a single strand DNA mediated energy transfer between UCLNPs and a fluorophore for the detection of mercuric ions.[127] Chemical sensing based on NIR excitation of upconverting nanomaterials in combination with conventional probes was demonstrated

for pH,[128] ammonia[129] and carbon dioxide[130] at the Institute of Analytical Chemistry, Chemo- and Biosensors at the University of Regensburg.

2.4. References

1   Escribano P, Julián-López B, Planelles-Aragó J, Cordoncillo E, Viana B, Sanchez C (2008) *Photonic and nanobiophotonic properties of luminescent lanthanide-doped hybrid organic-inorganic materials.* J Mater Chem 18:23-40

2   Auzel F (2004) *Upconversion and Anti-Stokes Processes with f and d Ions in Solids.* Chem Rev 104:139-173

3   Suyver JF, Aebischer A, Biner D, Gerner P, Grimm J, Heer S, Krämer KW, Reinhard C, Güdel HU (2005) *Novel materials doped with trivalent lanthanides and transition metal ions showing near-infrared to visible photon upconversion.* Opt Mater 27:1111-1130

4   Wang F, Liu X (2009) *Recent advances in the chemistry of lanthanide-doped Upconversion nanocrystals.* Chem Soc Rev 38:976-989

5   Zou X, Izumitani T (1993) *Spectroscopic properties and mechanisms of excited state absorption and energy transfer upcpnversion in Er^{3+}-doped glasses.* J Non-Cryst Solids 162:68-80

6   Downing E, Hesselink L, Ralston J, Macfarlane R (1996) *A Three-Color, Solid-State, Three-Dimensional Display.* Science 30:1185-1189

7   Hirao K, Todoroki S, Soga N (1992) *CW room temperature upconversion lasing in Er^{3+}-doped fluoride glass fibre.* J Non-Cryst Solids 143:40-45

8   Wang H-Q, Nann T (2011) *Upconverting Nanoparticles.* Springer Ser Fluoresc 7:115-132

9   Menyuk N, Dwight K, Pierce JW (1972) *$NaYF_4$:Yb,Er – an efficient upconversion phosphor.* Appl Phys Lett 21:159-161

10   Haase M, Schäfer H (2011) *Upconverting Nanoparticles.* Angew Chem Int Ed 50:5808-5829

11   Liu C, Wang H, Chen D (2009) *Monodisperse, size-tunable and highly efficient β-$NaYF_4$:Yb,Er(Tm) up-conversion luminescent nanospheres: controllable synthesis and their surface modifications.* J Mater Chem 19:3546-3553

12   Wang F, Han Y, Lim CS, Lu Y, Wang J, Xu J, Chen H, Zhang C, Hong M, Liu X (2010) *Simultaneous phase and size control of upconversion nanocrystals through lanthanide doping.* Nature 463:1061-1065

13   Zhou J, Sun Y, Xiong L, Hu H, Li F (2010) *Dual-modality in vivo imaging using rare-earth nanocrystals with near-infrared to near-infrared (NIR-to-NIR) upconversion luminescence and magnetic resonance properties.* Biomaterials 31:3287-3295

14   Park YI, Kim JH, Lee KT, Jeon K-S, Na HB, Yu JH, Kim HM, Lee N, Choi SH, Baik S-I, Kim H, Park SP, Park B-J, Kim YW, Lee SH, Yoon S-Y, Song IC, Moon WK Suh YD, Hyeon T (2009) *Nonblinking and Nonbleaching Upconverting Nanoparticles as an Optical Imaging Nanoprobe and T1 Magnetic Resonance Imaging Contrast Agent.* Adv Mater 21:4467-4471

15   Dieke GH (1968) *Spectra and Energy Levels of Rare Earth Ions in Crystals.* Wiley Interscience, New York

16   Mahalingam V, Vetrone F, Naccache R, Speghini A, Capobianco JA (2009) *Colloidal Tm^{3+}/Yb^{3+}-Doped $LiYF_4$ Nanocrystals: Multiple Luminescence Spanning the UV to NIR Regions via Low-Energy Excitation.* Adv Mater 21:1-4

17   Qu Y, Kong X, Sun Y, Zeng Q, Zhang H (2009) *Effect of Excitation Power Density on the Upconversion Luminescence of LaF_3:Yb^{3+},Er^{3+} nanocrystals.* J Alloy Compd 485:493-496

18   Yang LW, Han HL, Zhang YY, Zhong JX (2009) *White Emission by Frequency Up-Conversion in Yb^{3+}-Ho^{3+}-Tm^{3+} Triply Doped Hexagonal $NaYF_4$ Nanorods.* J Chem Phys C 113:18995-18999

19   Rudin M, Weissleder R (2003) *Molecular Imaging in Drug Discovery and Development.* Nat Rev Drug Discovery 2:123-131

20   Weissleder R, Mahmood U (2001) *Molecular Imaging.* Radiology 219:316-333

21   Massoud TF, Gambhir SS (2003) *Molecular imaging in living subjects: seeing fundamental biological processes in a new light.* Genes Dev 17:545-580

22   Weissleder R, Mahmood U (2001) *Molecular Imaging.* Radiology 219:316-333
23   Ntziachristos V (2006) *Fluorescence Molecular Imaging.* Annu Rev Biomed Eng 8:1-33
24   Helmchen F, Denk W (2005) *Deep tissue two-photon microscopy.* Nat Methods 2:932-941
25   Denk W, Svoboda K (1997) *Photon Upmanship: Why Multiphoton Imaging is More than a Gimmick.* Neuron 18:351-357
26   Svoboda K, Yasuda R (2006) *Principles of Two-Photon Excitation and Its Applications to Neuroscience.* Neuron 50:823-839
27   Rubart Michael (2004) *Two-Photon Microscopy of Cells and Tissue.* Circ Res 95:1154-1166
28   Resch-Genger U, Grabolle M, Cavaliere-Jaricot S, Nitschke R, Nann T (2008) *Quantum Dots versus organic dyes as fluorescent labels.* Nat Methods 5:763-775
29   Nyk M, Kumar R, Ohulchanskyy TY, Bergey EJ, Prasad PN (2008) *High Contrast in Vitro and in Vivo Photoluminescence Bioimaging using Near Infrared to Near Infrared Up-Conversion in Tm^{3+} and Yb^{3+} Doped Fluoride Nanophosphors.* Nano Lett 8:3834-3838
30   Waggoner A (2006) *Fluorescent labels for proteomics and genomics.* Curr Opin Chem Biol 10:62-66
31   Wang F, Tan WB, Zhang Y, Fan X, Wang M (2006) *Luminescent nanomaterials for biological labelling.* Nanotechnology 17:R1-R13
32   Shimomura O, Johnson FH, Saiga Y (1962) *Extraction, Purification and Properties of Aequorin, a Bioluminescent Protein from the Luminous Hydromedusan,* Aequorea. J Cell Physiol 59: 223–239
33   Zhang J, Campbell RE, Ting AY, Tsien RY (2002) *Creating New Fluorescent Probes for Cell Biology.* Nat Rev Mol Cell Biol 3_906-918
34   Hoffman RM (2005) *Advantages of multi-color fluorescent proteins for whole-body and in vivo cellular imaging.* J Biomed Opt 10:041202
35   Fernández-Moreira V, Thorp-Greenwood FL, Coogan MP (2010) *Application of d^6 transition metal complexes in fluorescence cell imaging.* Chem Commun 46:186-202
36   Terpetschnig E, Szmacinski H, Lakowicz JR (1997) *Long-lifetime metal-ligand complexes as probes in biophysics and clinical chemistry.* Method Enzymol 278:295-321
37   Licha K (2002) *Contrast Agents for Optical Imaging.* Top Curr Chem 222:1-29
38   Vereb G, Jares-Erijman E, Selvin PR, Jovin TM (1998) *Temporally and Spectrally Resolved Imaging Microscopy of Lanthanide Chelates.* Biophys J 74:2210-2222
39   Montgomery CP, Murray BS, New EJ, Pal R, Parker D (2008) *Cell-Penetrating Metal Complex Optical Probes: Targeted and Responsive Systems Based on Lanthanide Luminescence.* Accounts Chem Res 42:925-937
40   Hemmilä I, Laitala V (2005) *Progress in Lanthanides as Luminescent Probes.* J Fluoresc 15: 530-542
41   Burns A, Ow H, Wiesner U (2006*) Fluorescent core-shell silica nanoparticles: towards "Lab on a Particle" architectures for nanobiotechnology.* Chem Soc Rev 35:1028-1042
42   Yao G, Wang L, Wu Y, Smith J, Xu J, Zhao W, Lee E, Tan W (2006) *Flodots: luminescent nanoparticles.* Anal Bioanal Chem 385:518-524
43   Baier MC, Huber J, Mecking S (2009) *Fluorescent Conjugated Polymer Nanoparticles by Polymerization in Miniemulsion.* J Am Chem Soc 131:14267-14273
44   Huhtinen P, Kivelä M, Kuronen O, Hagren V, Takalo H, Tenhu H, Lövgren T, Härmä H (2005) *Synthesis, Characterization, and Application of Eu(III), Tb(III), Sm(III), and Dy(III) Lanthanide Chelate Nanoparticle Labels.* Anal Chem 77:2643-2648
45   Wang L, Tan W (2006) *Multicolor FRET Silica Nanoparticles by Single Wavelength Excitation.* Nano Lett 6:84-88
46   Wang L, Yang C, Tan W (2005) *Dual-Luminophore-Doped Silica Nanoparticles for Multiplexed Signaling.* Nano Lett 5:37-43
47   Bestvater F, Spiess E, Stobrawa G, Hacker M, Feurer T, Porlow T, Berchner-Pfannschmidt U, Wotzlaw C, Acker H (2002) *Two-photon fluorescence absorption and emission spectra of dyes relevant for cell imaging.* J Microsc 208:108-115
48   Lansford R, Bearman G, Fraser SE (2001) *Resolution of multiple green fluorescent protein color variants and dyes using two-photon microscopy and imaging spectroscopy.* J Biomed Opt 6:311-318
49   Xu C, Webb WW (1996*) Measurement of two-photon excitation cross sections of molecular fluorophores with data from 690 to 1050 nm.* J Opt Soc Am B 13:481-491

50   Svoboda K, Denk W, Kleinfeld D, Tank DW (1997) *In vivo dendritic calcium dynamics in neocortical pyramidal neurons.* Nature 385:161-165

51   Albota M, Beljonne D, Brédas J-L Ehrlich JE, Fu J-Y, Heikal AA, Hess SE, Kogej T, Levin MD, Marder SR, McCord-Maughon D, Perry JW, Röckel H, Rumi M, Subramaniam G, Wenn WW, Wu X-L, Xu C (1998) *Design of Molecules with Large Two-Photon Absorption Cross Sections.* Science 281:1653-1656

52   Yoo J, Yang K, Jeong M-Y, Ahn HC, Jeon S-J, Cho BR (2003) *Bis-1,4-(p-diarylaminostryl)-2,5-dicyanobenzene Derivatives with Large Two-Photon Absorption Cross-Sections.* Org Lett 5:645-648

53   Wan Y, Yan L, Zhao Z, Ma X, Guo Q, Jia M, Lu P, Ramos-Ortiz G, Maldonado JL, Rodríguez M, Xia A (2010) *Gigantic Two-Photon Absorption Cross Sections and Strong Two-Photon Excited Fluorescence in Pyrene Core Dendrimers with Fluorene/Carbazole as Dendrons and Acetylene as Linkages.* J Phys Chem B 114:11737-11745

54   Gao X, Cui Y, Levenson RM, Chung LWK, Nie S (2004) *In vivo cancer targeting and imaging with semiconductor quantum dots.* Nat Biotechnol 22:969-976

55   Chatterjee DK, Rufaihah AJ, Zhang Y (2008) *Upconversion fluorescence imaging of cells and small animals using lanthanide doped nanocrystals.* Biomaterials 29:937-943

56   Hulanicki A, Glab S, Ingman F (1991) *Chemical Sensors: Definitions and Classifications.* Pure & Appl Chem 63:1247-1250

57   Cammann K, Guilbault GG, Hall EAH, Kellner R, Wolfbeis OS (1996) *The Cambridge Definition of Chemical Sensors.* Proceedings of the Cambridge Workshop on Chemical Sensors and Biosensors, Cambridge University Press, New York

58   Borisov SM, Wolfbeis OS (2008) *Optical Biosensors.* Chem Rev 108:423-461

59   Thévenot DR, Toth K, Durst RA, Wilson GS (1999) *Electrochemical Biosensors: Recommended Definitions and Classification.* Pure Appl Chem 71:2333-2348

60   Wolfbeis OS (2008) *Fiber-Optic Chemical Sensors and Biosensors.* Anal Chem 80: 4269-4283

61   McDonagh C, Burke CS, MacCraith BD (2008) *Optical Chemical Sensors.* Chem Rev 108: 400-422

62   Wolfbeis OS (2004) *Optical Sensors: Industrial, Environmental and Diagnostic Applications.* Springer Series on Chemical Sensors and Biosensors, Springer-Verlag, Berlin

63   Narayanaswamy R (1993) *Optical Chemical Sensors: Transduction and Signal Processing.* Analyst 118:317-322

64   Preininger C, Klimant I, Wolfbeis OS (1994) *Optical Fiber Sensor for Biological Oxygen Demand.* Anal Chem 66:1841-1846

65   Pérez-Ortíz N, Navarro-Villoslada F, Orellana G, Moreno-Jiménez F (2007) *Determination of the oxygen permeability (Dk) of contact lenses with a fiber-optic luminescent sensor system.* Sens Actuators B 126:394-399

66   Ge X, Hanson M, Shen H, Kostov Y, Brorson KA, Frey DD, Moreira AR, Rao G (2006) *Validation of an optical sensor-based high-throughput bioreactor system for mammalian cell culture.* J Biotechnol 122: 293-306

67   Mills A (2005) *Oxygen indicators and intelligent inks for packaging food.* Chem Soc Rev 34:1003-1011

68   Gründler P (2004) *Chemische Sensoren: Eine Einführung für Naturwissenschaftler und Ingenieure.* Springer-Verlag, Berlin, p.148

69   Winkler LW (1888) *Die Bestimmung des im Wasser gelösten Sauerstoffes.* Berichte der deutschen chemischen Gesellschaft 21:2843-2854

70   Broenkow WW, Cline JD (1969) *Colorimetric Determination of Dissolved Oxygen at Low Concentrations.* Limnol Oceanogr 14:450-454

71   Sastry GS, Hamm RE, Pool KH (1969) *Spectrophotometric Determination of Dissolved Oxygen in Water.* Anal Chem 41:857-858

72   Clark L C, Lyons C (1962) *Electrode systems for continuous monitoring in cardiovascular surgery.* Ann N Y Acad Sci 31:29-45

73   Amao Y (2003) *Probes and Polymers for Optical Sensing of Oxygen.* Microchim Acta 143:1-12

74   Kautsky H, Hirsch A (1931) *Wechselwirkung zwischen angeregten Farbstoff-Molekülen und Sauerstoff.* Chem Ber 64:2677-2683

75   Kautsky H (1938) *Quenching of luminescence by oxygen.* Trans Faraday Soc 35:216-219

76   Wolfbeis OS (2005) *Materials for fluorescence-based optical chemical sensors.* J Mater Chem 15:2657-2669

77   Preininger C, Klimant I, Wolfbeis OS (1994) *Optical Fiber Sensor for Biological Oxygen Demand.* Anal Chem 66:1841-1846

78   Gupta A, Rao G (2003) *A study of oxygen transfer in shake flasks using a non-invasive oxygen sensor.* Biotechnol Bioeng 84: 351-358

79   Anderlei T, Büchs J (2000) *Device for sterile online measurement of the oxygen transfer rate in shaking flasks.* Biochem Eng J 3478:1-6

80   Leiner MJP (1995) *Optical sensors for in vitro blood gas analysis.* Sensor Actuat B-Chem 29:169-173

81   Wolfbeis OS, Klimant I, Werner T, Huber C, Kosch U, Krause C, Neurauter G, Dürkop A (1998) *Set of luminescence decay time based chemical sensors for clinical applications.* Sensor Actuat B-Chem 51:17-24

82   Kellner K, Liebsch G, Klimant I, Wolfbeis OS, Blunk T, Schultz MB, Göpferich A (2002) *Determination of oxygen gradients in engineered tissue using a fluorescent sensor.* Biotechnol Bioeng 80:73-83

83   Xu H, Aylott JW, Kopelman R, Miller TJ, Philbert MA (2001) *A Real-Time Ratiometric Method for the Determination of Molecular Oxygen Inside Living Cells Using Sol-Gel-Based Spherical Optical Nanosensors with Applications to Rat C6 Glioma.* Anal Chem 73:4124-4133

84   Wang X, Gorris HH, Stolwijk JA, Meier RJ, Groegel DBM, Wegener J, Wolfbeis OS (2011) *Self-referenced RGB colour imaging of intracellular oxygen.* Chem Sci 2:901-906

85   Stich MIJ, Wolfbeis OS (2008) *Fluorescence Sensing and Imaging Using Pressure-Sensitive Paints and Temperature-Sensitive Paints.* Springer Ser Fluoresc 5:429-461

86   O'Donovan C, Hynes J, Yashunski D, Papkovsky DB (2005) *Phosphorescent oxygen-sensitive materials for biological applications.* J Mater Chem 15:2946-2951

87   Wu C, Bull B, Christensen K, McNeill J (2009) *Ratiometric Single-Nanoparticle Oxygen Sensors for Biological Imaging.* Angew Chem Int Ed 48:2741-2745; Angew Chem 121: 2779-2783

88   Borisov SM, Klimant I (2008) *Optical nanosensors - smart tools in bioanalytics.* Analyst 133:1302-1307

89   Meier RJ (2011) *Luminescent Single and Dual Sensors for In Vivo Imaging of pH and pO$_2$.* Ph.D. Thesis, University of Regensburg

90   DeRosa MC, Hodgson DJ, Enright GD, Dawson B, Evans CEB, Crutchley RJ (2004) *Iridium Luminophore Complexes for Unimolecular Oxygen Sensors.* J Am Chem Soc 126:7619-7626

91   Mills A (1997) *Optical Oxygen Sensors.* Platinum Metals Rev 41:115-127

92   Xu W, Kneas KA, Demas JN, DeGraff BA (1996) *Oxygen Sensors Based on Luminescence Quenching of Metal Complexes: Osmium Complexes Suitable for Laser Diode Excitation.* Anal Chem 68:2605-2609

93   Amao Y, Ishikawa Y, Okura I (2001) *Green luminescent iridium(III) complex immobilized in fluoropolymer film as optical oxygen-sensing material.* Anal Chim Acta 445:177-182

94   Borisov SM, Klimant I (2007) *Ultrabright Oxygen Optodes Based on Cyclometalated Iridium (III) Coumarin Complexes.* Anal Chem 79:7501-7509

95   DeRosa MC, Hodgson DJ, Enright GD, Dawson B, Evans CEB, Crutchley RJ (2004) *Iridium Luminophore Complexes for Unimolecular Oxygen Sensors.* J Am Chem Soc 126:7619-7626

96   Papkovsky DB (1993) *Luminescent porphyrins as probes for optical (bio)sensors.* Sensor Actuat B-Chem 11:293-300

97   Wang X, Chen H, Zhao Y, Chen X, Wang X, Chen X (2010) *Optical oxygen sensors move towards colorimetric determination.* TrAC 29:319-338

98   Demas JN, DeGraff BA Coleman PB (1999) *Oxygen Sensors Based on Luminescence Quenching.* Anal Chem 71:793A-800A

99   Papkovsky DB (1995) *Phosphorescent Complexes of Porphyrin Ketones: Optical Properties and Application to Oxygen Sensing.* Anal Chem 67:4112-4117

100   Liu Z-Q, Mei S, Li F-Y, Fang Q, Chen Z-H, Yi T, Huang C-H (2005) *Highly Selective Two-Photon Chemosensors for Fluoride Derived from Organic Boranes.* Org Lett 7:5481-5484

101   Zhang X, Ren X, Xu Q-H, Loh KP, Chen Z-K (2009) *One- and Two-Photon Turn-on Fluorescent Probe for Cysteine and Homocysteine with Large Emission Shift.* Org Lett 11:1257-1260

102 Zhang M, Li M, Zhao Q, Li F, Zhang D, Zhang J, Yi T, Huang C (2007) *Novel Y-type two-photon active fluorophore: synthesis and application in fluorescent sensor for cysteine and homocysteine.* Tetrahedron Lett 48:2329-2333

103 Taki M, Wolford JL, O'Halloran TV (2004) *Emission Ratiometric Imaging of Intracellular Zinc: Design of a Benzoxazole Fluorescent Sensor and Its Application in Two-Photon Microscopy.* J Am Chem Soc 126:712-713

104 Chang CJ, Nolan EM, Jaworski J, Okamoto K-I, Hayashi Y, Sheng M, Lippard SJ (2004) *ZP8, a Neuronal Zinc Sensor with Improved Dynamic Range; Imaging Zinc in Hippocampal Slices with Two-Photon Microscopy.* Inorg Chem 43:6774-6779

105 Kim HM, Jeong M-Y, Ahn HC, Jeon S-J, Cho BR (2004) *Two-Photon Sensor for Metal Ions Derived from Azacrown Ether.* J Org Chem 69:5749-5751

106 Pond SJK, Tsutsumi O, Rumi M, Kwon O, Zojer E, Brédas J-L, Marder SR, Perry JW (2004) *Metal-Ion Sensing Fluorophores with Large Two-Photon Absorption Cross Sections: Aza-Crown Ether Substituted Donor-Acceptor-Donor Distyrylbenzenes.* J Am Chem Soc 126:9291-9306

107 Stosiek C, Garaschuk O, Holthoff K, Konnerth A (2003) *In vivo two-photon calcium imaging of neuronal networks.* P Natl Acad Sci USA 100:7319-7324

108 Piston DW, Kirby MS, Cheng H, Lederer WJ, Webb WW (1994) *Two-photon-excitation fluorescence imaging of three-dimensional calcium-ion activity.* Appl Optics 33:662-669

109 Briñas RP, Troxler T, Hochstrasser RM, Vinogradov SA (2005) *Phosphorescent Oxygen Sensor with Dentritic Protection and Two-Photon Absorbing Antenna.* J Am Chem Soc 127:11851-11862

110 Lebedev AY, Troxler T, Vinogradov SA (2008) *Design of Metalloporphyrin-Based Dentritic Nanoprobes for Two-Photon Microscopy of Oxygen.* J Porphyr Phtalocya 12:1261-1269

111 Finikova OS, Chen P, Ou Z, Kadish KM, Vinogradov SA (2008) *Dynamic Quenching of Porphyrin Triplet States by Two-Photon Absorbing Dyes: Towards a Two-Photon-Enhanced Oxygen Nanosensor.* J Photochem Photobiol A Chem 198:75-84

112 Finikova OS, Lebedev AY, Aprelev A, Troxler T, Gao F, Garnacho C, Muro S, Hochstrasser RM, Vinogradov SA (2008) *Oxygen Microscopy by Two-Photon-Excited Phosphorescnce.* Chemphyschem 9:1673-1679

113 Wu C, Bull B, Christensen K, McNeill J (2009) *Ratiometric Single-Nanoparticle Oxygen Sensors for Biological Imaging.* Angew Chem Int Ed 48:2741-2745

114 McLaurin EJ, Greytak AB, Bawendi MG, Nocera DG (2009) *Two-Photon Absorbing Nanocrystal Sensors for Ratiometric Detection of Oxygen.* J Am Chem Soc 131:12994-13001

115 Fischer LH, Harms GS, Wolfbeis OS (2011) *Upconverting Nanoparticles for Nanoscale Thermometry.* Angew Chem Int Ed 50:4546-4551

116 Vetrone F, Nacchache R, Zamarrón A, de la Fuente AJ, Sanz-Rodríguez F, Maestro LM, Rodriguez EM, Jaque D, Solé JG, Capobianco JA (2010) *Temperature Sensing Using Fluorescent Nanothermometers.* ACS Nano 4:3254-3258

117 Bogdan N, Vetrone F, Ozin GA, Capobianco JA (2011) *Synthesis of Ligand-Free Colloidally Stable Water Dispersible Brightly Luminescent Lanthanide-Doped Upconverting Nanoparticles.* Nano Lett 11:835-840

118 Saleh SM, Ali R, Wolfbeis OS (2011) *Quenching of the Luminescence of Upconverting Luminescent Nanoparticles by Heavy Metal Ions.* Chem-Eur J 17:14611-14617

119 Zhang P, Rogelj S, Nguyen K, Wheeler D (2006) *Design of a highly sensitive and specific nucleotide sensor based on photon upconverting particles.* J Am Chem Soc 128:12410–12411

120 Kumar M, Guo Y, Zhang P (2009) *Highly sensitive and selective oligonucleotide sensor for sickle cell disease gene using photon upconverting nanoparticles.* Biosens Bioelectron 24:1522–1526

121 Kumar M, Zhang P (2009) *Highly sensitive and selective label-free optical detection of DNA hybridization based on photon upconverting nanoparticles.* Langmuir 25:6024–6027

122 Rantanen T, Järvenpää ML, Vuojola J, Arppe R, Kuningas K, Soukka T (2009) *Upconverting phosphors in a dual-parameter LRET-based hybridization assay.* Analyst 134:1713–1716

123 Wang M, Hou W, Mi CC, Wang WX, Xu ZR, Teng HH, Mao CB, Xu SK (2009) *Immunoassay of goat antihuman immunoglobulin G antibody based on luminescence resonance energy transfer between near-infrared responsive NaYF$_4$:Yb, Er upconversion fluorescent nanoparticles and gold nanoparticles.* Anal Chem 81:8783–8789

124 Wang L, Yan R, Huo Z, Wang L, Zeng J, Bao J, Wang X, Peng Q, Li Y (2005) *Fluorescence resonance energy transfer biosensor based on upconversion-luminescent nanoparticles.* Angew Chem Int Ed Engl 117:6208–6211

125 Saleh SM, Ali R, Hirsch T, Wolfbeis OS (2011) *Detection of biotin-avidin affinity binding by exploiting a self-referenced system composed of upconverting luminescent nanoparticles and gold nanoparticles.* J Nanopart Res 13:4603-4611

126 Rantanen T, Ja¨rvenpa¨a¨ ML, Vuojola J, Kuningas K, Soukka T (2008) *Fluorescence quenching based enzyme-activity assay by using photon upconversion.* Angew Chem Int Ed 47:3811–3813

127 Kumar M, Zhang P (2010) *Highly Sensitive and Selective Label-Free Optical Detection of Mercuric Ions Using Photon Upconverting Nanoparticles.* Biosens Bioelectron 25:2431-2435

128 Sun L-N, Peng H, Stich MIJ, Achatz DE, Wolfbeis OS (2009) *pH sensor based on upconverting luminescent lanthanide nanorods.* Chem Commun:5000-5002

129 Mader HS, Wolfbeis OS (2010) *Optical Ammonia Sensor Based on Upconverting Luminescent Nanoparticles.* Anal Chem 82:5002-5004

130 Ali R, Saleh SM, Meier RJ, Azab HA, Abdelgawad II, Wolfbeis OS (2010) *Upconverting nanoparticles based optical sensor for carbon dioxide.* Sensor Actuat B-Chem:150:126-131

3. Synthesis and Characterization of NaYF$_4$:Yb,X (X = Er^{3+}, Tm^{3+})

For 10 years substantial efforts have been made to synthesize small, bright and uniform UCLNPs. Meanwhile, numerous protocols have become available for producing upconverting nanocrystals in the form of spheres, rods, plates, or tubes. For the most part, the method depends on the desired host lattice. Common procedures include thermal decomposition, co-precipitation (also called arrested precipitation), solvothermal synthesis, combustion and sol-gel processes,[1] synthesis in liquid-solid solutions,[2,3] and ionothermal synthesis.[4] This chapter deals with the preparation and characterization of UCLNPs. As mentioned above, lanthanide doped NaYF$_4$ was found to be the most efficient host for luminescence upconversion. Therefore, it was also the material of choice in this work. The two main procedures for the synthesis of NaYF$_4$-based UCLNPs are co-precipitation and the thermal decomposition method.[1] In the work for this thesis, both methods were performed to fabricate NaYF$_4$:Yb,X (X = Er^{3+}, Tm^{3+}). Optimized doping ratios of Y^{3+}/Yb^{3+}/X^{3+} for most efficient upconversion were used (78/20/2 for Er^{3+} and 79.5/20/0.5 for Tm^{3+}).[5] Generally, nucleation and growth of NPs in solution can be described by the LaMer mechanism[6] which divides particle formation into three phases. First, reactant or monomer concentration increases until a critical limit is reached that exceeds solubility. At this point of supersaturation rapid nucleation occurs and the concentration of reactants in sudden bursts decreases. Thereon particle growth follows until the monomer concentration falls below solubility or the reaction is interrupted.[7,8] Most probably an Ostwald ripening process is further involved, i.e. smaller particles dissolve in benefit of the growth of bigger particles in saturated solution.[8]

The particles were characterized and compared regarding size, phase and morphology by X-ray diffraction (XRD) and transmission electron microscopy (TEM). Upconverting luminescence spectra were collected using an adjustable (maximum 5 W) 980 nm CW diode laser as the

excitation light source at an otput power of 1 W unless otherwise state. Thermal gravimetric analysis (TGA), Fourier transform infrared (FTIR) spectroscopy and/ or diffuse reflectance infrared Fourier transform (DRIFT) spectroscopy were applied for surface characterization. Results from XRD, TGA and IR spectroscopy were found to be identical for Er^{3+} and Tm^{3+} doped UCLNPs which is why general findings are shown.

3.1. Co-precipitation followed by Thermal Treatment

In co-precipitation technique, nanosized lanthanide doped NaYF$_4$ particles are precipitated as an insoluble product by mixing sodium fluoride (NaF) with a mixture of the RE ions in aqueous solution at room temperature. Usually EDTA (ethylendiamine tetraacetic acid) serves as a capping agent that is essential to control the particle size. EDTA efficiently forms complexes with RE ions in which one trivalent ion is coordinated by one ligand molecule.[9,10] The slow release of ions from the chelate controls the particle growth and is dependent on the ratio of EDTA to RE ions.[7,11] Adsorption of ligand molecules to the surface of thus formed particles further prevents aggregation. Several protocols for this synthetic route have been published which make use of different capping agents[12] or different RE precursors. Possible candidates are nitrates,[13] chlorides,[9,10] or oxides[14] of Y^{3+}, Yb^{3+}, and of the activators Er^{3+} and Tm^{3+}. In general, co-precipitation results in the formation of lanthanide doped α-NaYF$_4$. A postsynthetic thermal treatment of the isolated particles induces a cubic to hexagonal phase transfer and enhances upconversion efficiency.[9,13,14] The particles obtained are well dispersible in ethanol or water.

Within this work, co-precipitation was carried out according to the protocol of Yi et al.[9] using RE chlorides as precursors and EDTA as the capping agent. Acidic aqueous stock solutions of the chlorides were combined with an aqueous stock solution of EDTA in a molar ratio of EDTA/ RE chlorides = 1/1 to form RE-EDTA complex compounds. In parallel, NaF was dissolved in water and the complexes were injected

quickly into this solution. Within a few minutes the mixture turned turbid due to particle growth. After 1 h stirring at room temperature, the precipitated UCLNPs were collected by centrifugation, washed with water and ethanol, dried, and ground in a mortar. The doping ratio can be controlled by keeping the total amount of chlorides constant while varying the ratio YCl$_3$/YbCl$_3$/XCl$_3$. The colorless solid was annealed at 400 °C for 5 h in a muffle furnace to achieve cubic to hexagonal phase transition.

The transformation from α- to β-NaYF$_4$ can be followed by looking at the XRD pattern of the as prepared particles before and after thermal treatment (Figure 3.1).
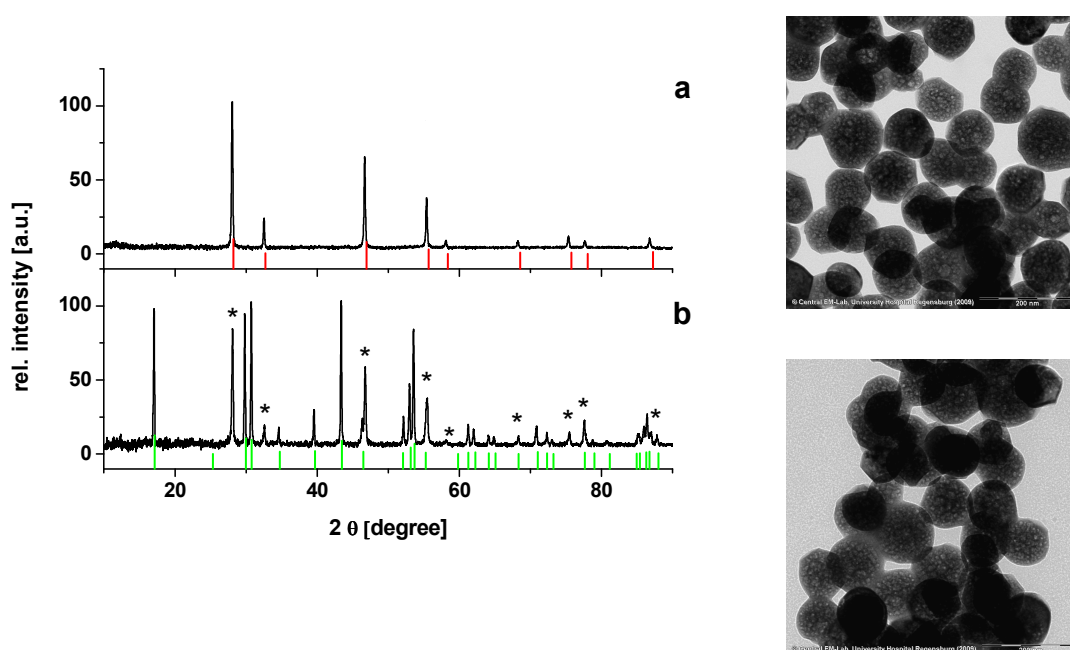
Figure 3.1: XRD pattern of UCLNPs prepared by co-precipitation before (a) and after annealing at 400 °C for 5h (b). Before the temperature treatment, the signals can be assigned to α-NaYF$_4$:Yb,X (cubic phase; ICDD, No. 77-2042, red lines). After annealing, additional peaks emerge that accord with β-NaYF$_4$:Yb,X (hexagonal phase; ICDD, No. 28-1192, green lines). The peaks asterisked in (b) mark the remaining fraction of the cubic phase. The TEM pictures on the right display the corresponding NPs in 80,000x magnification. The length of the scale bars is 200 nm.

The peaks of the UCLNPs before annealing (Figure 3.1a) are consistent with the pattern of α-NaYF$_4$ (cubic phase; International Centre for Diffraction Data (ICDD) No. 77-2042, red lines). In the XRD pattern after heating (Figure 3.1b) additional peaks emerge that indicate a partial phase transition to β-NaYF$_4$ (hexagonal phase; ICDD No. 28-1192, green

lines). The TEM pictures next to the XRD spectra display the corresponding UCLNPs, whereas NaYF$_4$:Yb,Er and NaYF$_4$:Yb,Tm did not differ in size and morphology. The particle size is moderately uniform and ranges between 80 and 120 nm. Their shape is roughly spherical, whereas the particles are more agglomerated after the annealing process. Cubic to hexagonal phase transition is promoted by higher temperatures over a extended period of time. But the particles are irreversibly transformed into large amorphous aggregates simultaneously.[9,10] Hence, a compromise must be reached between the scale and time of heating regarding brightness and size of the particles. The progressive agglomeration might be a consequence of the decomposition of the stabilizing surface ligands. It was proved by TGA of UCLNPs prepared by co-precipitation before and after thermal treatment that combustion of EDTA takes place during the annealing process (Figure 3.2).
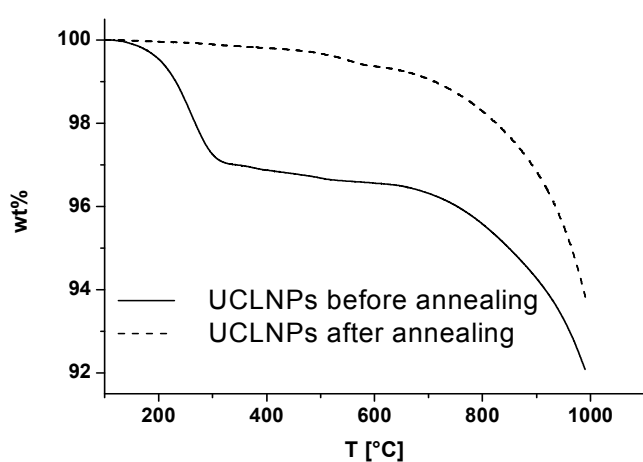
Figure 3.2: Thermogram of UCLNPs prepared via co-precipitation before (solid line) and after (dashed line) annealing at 400 °C for 5 h. After synthesis and washing procedures about 3wt% EDTA is left on the particle surface, which is completely removed by thermal treatment.

A major weight loss of 3.5% with a maximum gradient around 250 °C is observed for the particles before the annealing process (Figure 3.2, solid line). This is in line with the decomposition temperature of EDTA.[15] The UCLNP material itself starts to decompose above 600 °C. It is obvious that after thermal treatment at 400 °C for 5 h no more EDTA is left on the particle surface (Figure 3.2, dashed line).

Comparing luminescence spectra of the UCLNPs before and after annealing (Figure 3.3) yields that α-NaYF$_4$:Yb,X hardly exhibits any

upconversion emission, whereas very distinct peaks at the expected wavelengths appear in the spectra of partly β-NaYF$_4$:Yb,X.
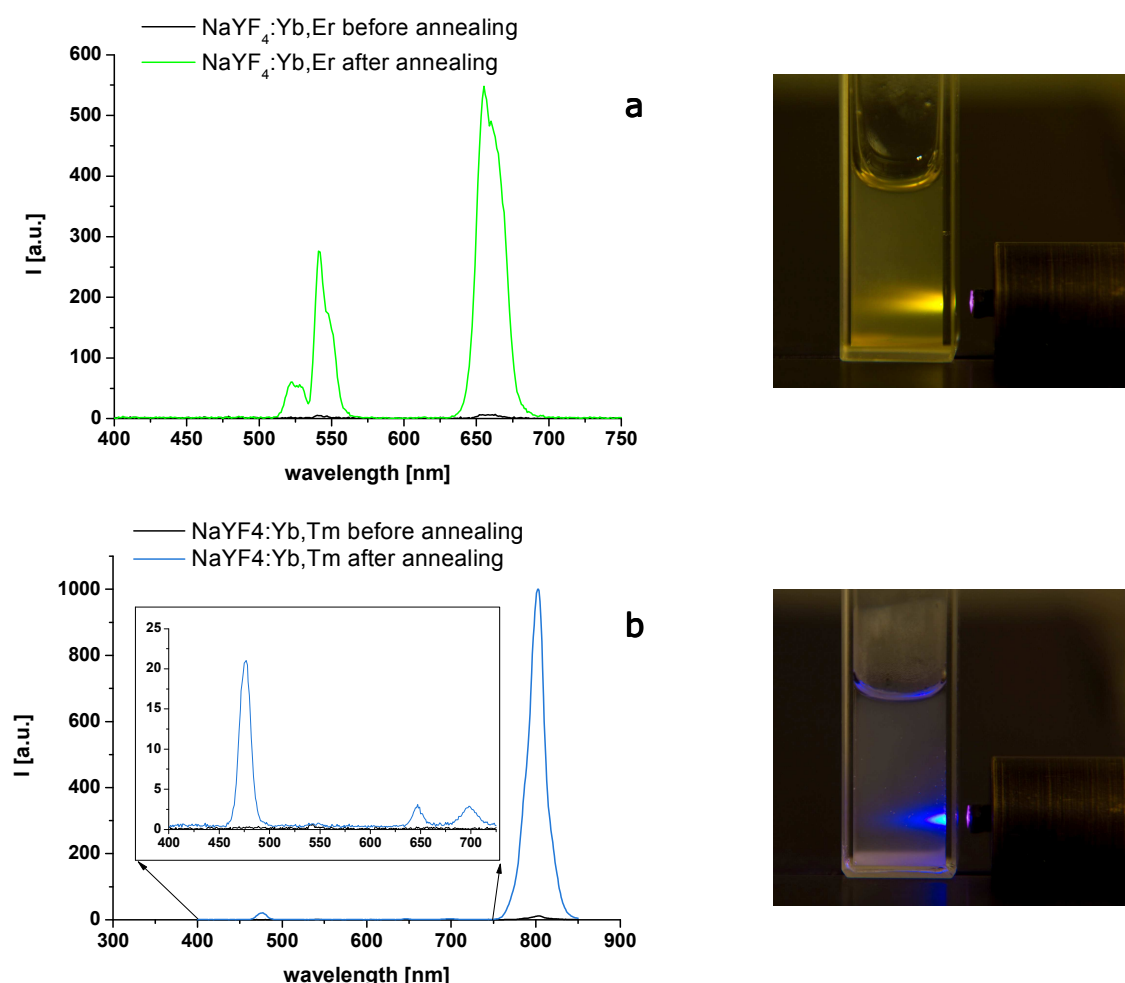
Figure 3.3: Upconversion luminescence spectra of 0.1wt% solutions of NaYF$_4$:Yb,Er (a) and NaYF$_4$:Yb,Tm (b) before (black lines) and after the annealing process (colored lines) in ethanol. The framed magnification of the VIS range in (b) illustrates the much higher intensity of the NIR peak at 800 nm. The pictures beside the graphs were taken by a conventional consumer camera and show the emission of the corresponding solutions as they appear to the human eye upon excitation with a 980 nm CW diode laser.

Figure 3.3a displays the spectra of 0.1wt% solutions of NaYF$_4$:Yb,Er in ethanol after excitation in the NIR, Figure 3.3b the graphs of analogous dispersions of NaYF$_4$:Yb,Tm. Er^{3+} doped UCLNPs emit in the green (520, 540 nm) and the red region (655 nm) of the VIS spectral range. The luminescence appears to be green to the eye (see inserted picture in Figure 3.3a) even though the red peak exhibits a higher intensity in the spectrum. This effect is due to the response of the eye to light with a maximum at around 550 nm i.e. it is most sensitive for green-yellowish

light and less sensitive to the red emission.[16] Figure 3.3b displays the upconversion spectra of Tm^{3+} doped nanocrystals. The complete emission including the peak in the NIR at 800 nm is shown in the main layer. This signal is much more intense than the blue and red emissions. The insetted spectrum is a magnification of the VIS spectral range with signals at 475, 646, and 696 nm. Noteworthy, the expected peak at 450 nm (compare Figure 2.2) does not appear. The picture beside the spectrum depicts the blue luminescence of NaYF$_4$:Yb,Tm since NIR light is invisible to the eye. The emissions of Er^{3+} and Tm^{3+} doped NaYF$_4$ were collected at identical laser and instrument parameters i.e. the VIS luminescence of green emitting UCLNPs is more intense than that of blue emitting particles.

3.2. Thermal Decomposition Method

The thermal decomposition method requires no subsequent heat treatment of the UCLNPs since the synthesis is carried out at high temperatures in an appropriate solvent resulting in the formation of RE-doped hexagonal phase NaYF$_4$ from the outset. RE precursors together with fluoride and sodium ions are typically reacted in octadecene (OD) whose boiling point is above 300 °C. Suitable precursors are RE oxides,[17] nitrates,[2] chlorides[18] or trifluoroacetates,[19, 20] whereas the latter are less favorable due to emerging toxic fluorinated gases and byproducts.[21] As in the co-precipitation technique, a capping agent is used to control the particle size and to prevent aggregation. Typical ligands are long-chained acids or amines like oleic acid (OA) or oleylamine (OAm) since these molecules are stable at the temperatures of this synthesis. These surfactants might serve as the intrinsic solvent as well.[20]

In this work the thermal decomposition of RE precursors, sodium hydroxide (NaOH) and ammonium fluoride (NH$_4$F) in the presence of OA and OD was carried out according to the protocol of Li et al.[18] Hexahydrates of the RE chlorides were heated in an OD-OA mixture at 150 °C to dissolve the salts. NaOH and NH$_4$F were dissolved in methanol

and added dropwise to the cooled precursor solution. A colorless precipitate was formed immediately. After 2 h of stirring and removal of methanol, the particle suspension was heated to 300 °C in a three-neck round bottom flask equipped with an internal thermometer and an air cooler under a gentle flow of argon and kept at this temperature for 1.5 h. Argon was turned off until the desired temperature was reached. After cooling to room temperature, the off-white particles were isolated by precipitation followed by washing with ethanol and acetone via centrifugation-redispersion cycles.

Figure 3.4 displays the XRD spectrum of NaYF$_4$:Yb,X prepared by thermal decomposition and the ICDD pattern 28-1192 (red lines). It reveals that the particles thus obtained are of hexagonal phase.
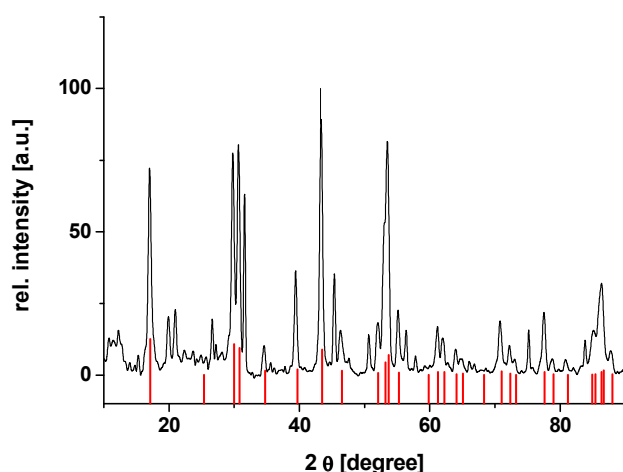
Figure 3.4: XRD pattern of UCLNPs of the type NaYF$_4$:Yb,X prepared by thermal decomposition. The peaks can be assigned to hexagonal NaYF$_4$ (ICDD, No. 28-1192, red lines).

Compared to the XRD spectra of NaYF$_4$:Yb,X prepared by co-precipitation (Figure 3.1), peak broadening can be observed which is due to the smaller size of the particles[22] that were synthesized via the thermal decomposition method.

The TEM pictures in Figure 3.5 illustrate NaYF$_4$:Yb,Er (a) and NaYF$_4$:Yb,Tm (b), respectively. Unlike for particles prepared via co-precipitation, the different activator ions cause a certain deviation in size. In repeated syntheses UCLNPs of the type NaYF$_4$:Yb,Tm were found to be about 34 to 40 nm in diameter and hence slightly larger than NaYF$_4$:Yb,Er

with 25 to 30 nm. The regular space between NPs lying next to each other is due to oleic acid molecules that remain on the surface of the particles. These surface ligands prevent aggregation during and after the synthesis by steric repulsion and are responsible for good dispersibility of the particles in non-polar solvents.
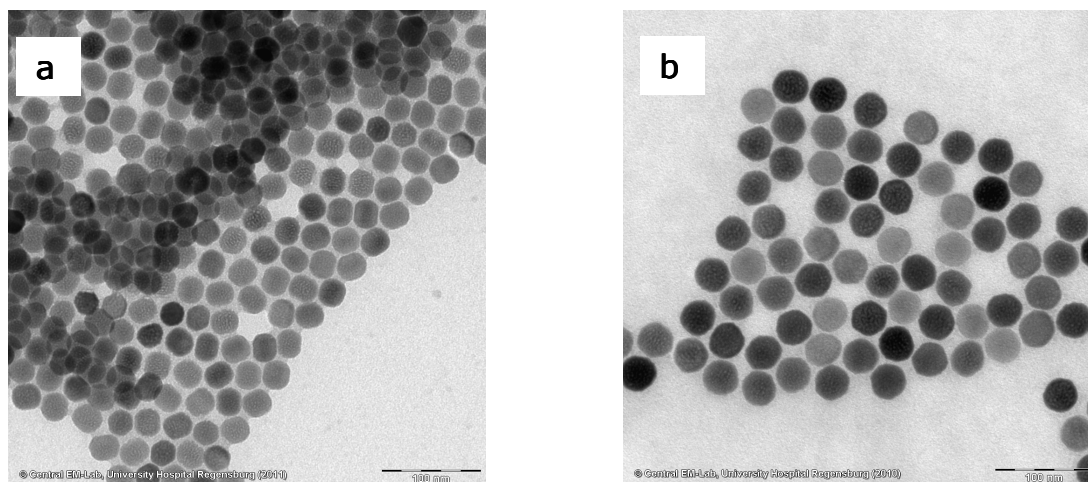
Figure 3.5: TEM pictures of NaYF$_4$:Yb,Er (a) and NaYF$_4$:Yb,Tm (b) prepared via thermal decomposition. Different activator ions cause a variation in size. Er^{3+}-doped UCLNPs were found to have an average size of about 27 nm, whereas Tm^{3+}-doped UCLNPs are bigger with a diameter of about 37 nm. The particles are shown in 100,000x magnification. The length of the scale bars is 100 nm.

Luminescence spectra of the green (X = Er^{3+}) and the blue (X = Tm^{3+}) emitting NaYF$_4$:Yb,X are presented below. Figure 3.6a shows the emission of a 0.1wt% solution of NaYF$_4$:Yb,Er in cyclohexane after excitation in the NIR, Figure 3.6b the spectra of an analogous dispersion of NaYF$_4$:Yb,Tm. Noteworthy, the emission wavelengths of NaYF$_4$:Yb,X (X = Er^{3+}, Tm^{3+}) prepared by either method are identical. The intensity ratios of the peaks of NaYF$_4$:Yb,Tm are nearly unchanged (compare Figure 3.3b and Figure 3.6b), whereas the intensity ratio of the green and red emission in NaYF$_4$:Yb,Er is inverted (compare Figure 3.3a and Figure 3.6a). This is most likely due to the pure hexagonal crystal phase in NaYF$_4$:Yb,Er in contrast to a mixture of cubic and hexagonal phase in NaYF$_4$:Yb,Er. The spectra given in Figure 3.6 were also collected at identical laser and instrument parameters i.e. the VIS luminescence of the green emitting UCLNPs is brighter than that of blue emitting particles again.
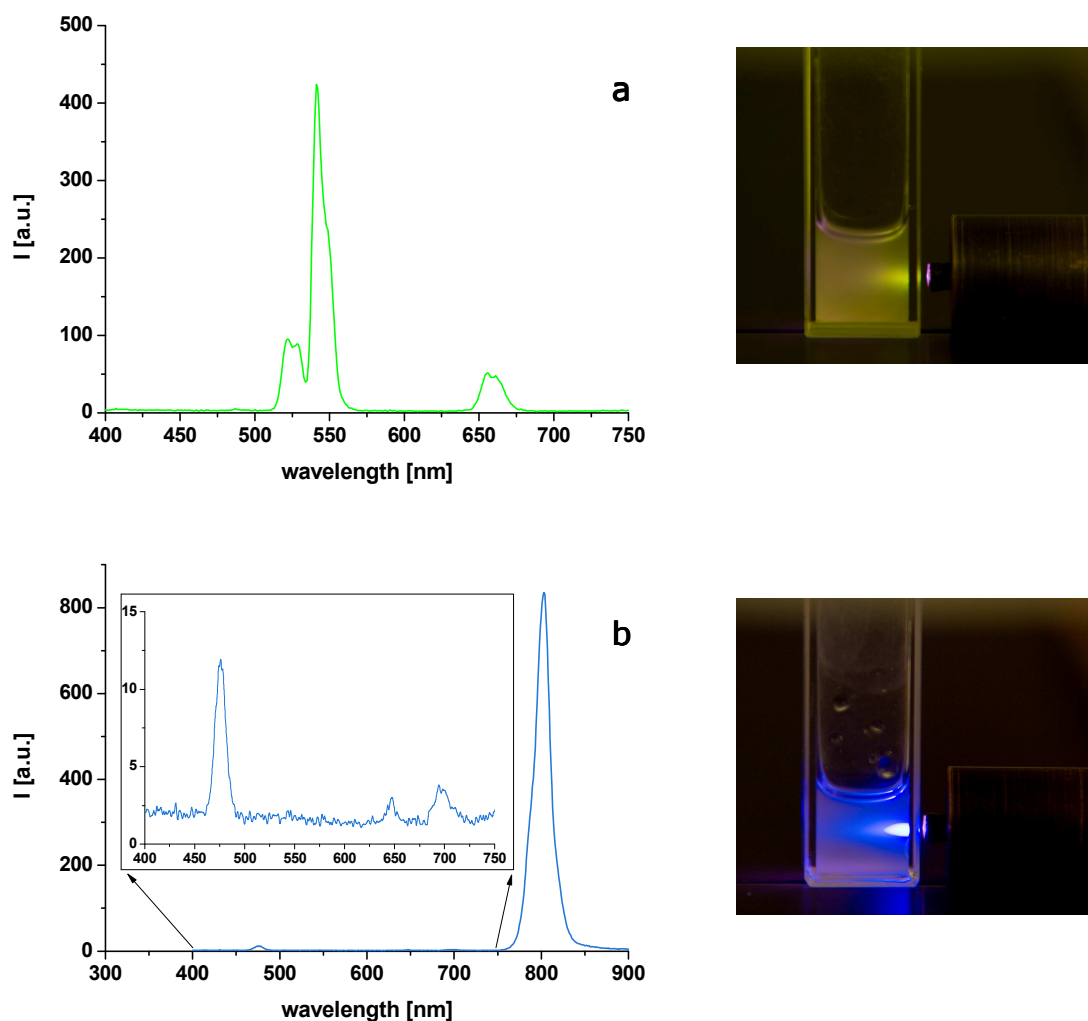
Figure 3.6: Upconversion luminescence spectra of 0.1wt% solutions of NaYF$_4$:Yb,Er (a) and NaYF$_4$:Yb,Tm (b) in cyclohexane. The magnification of the VIS spectral range in (b) illustrates the much higher intensity of the NIR peak at 800 nm. The pictures beside the spectra were taken by a conventional camera and display the emission of the particle solutions upon excitation with a 980 nm CW diode laser.

The existence of OA molecules on the surface of NaYF$_4$:Yb,X (X = Er^{3+}, Tm^{3+}) was complementary proven by DRIFT (Figure 3.7a) and FTIR spectroscopy (Figure 3.7b). The peaks around 2930 and 2860 cm^{-1} can be assigned to asymmetric and symmetric stretching of the saturated hydrocarbon chains. Apparently, there are weak signals from the alkene group around 3005 and 1705 cm^{-1} in the DRIFT spectrum (Figure 3.7a). Carboxylate stretching vibrations around 1560 and 1475 cm^{-1} confirm the adsorption of OA on the surface of the UCLNPs via its carboxylate group.[23] The broad hydroxyl stretching band (3100 to 3700 cm^{-1}) and very weak signals at 1755 and 1305 cm^{-1} are only evident in the results of DRIFT

spectroscopy and might be an indication of remaining carboxyl groups.
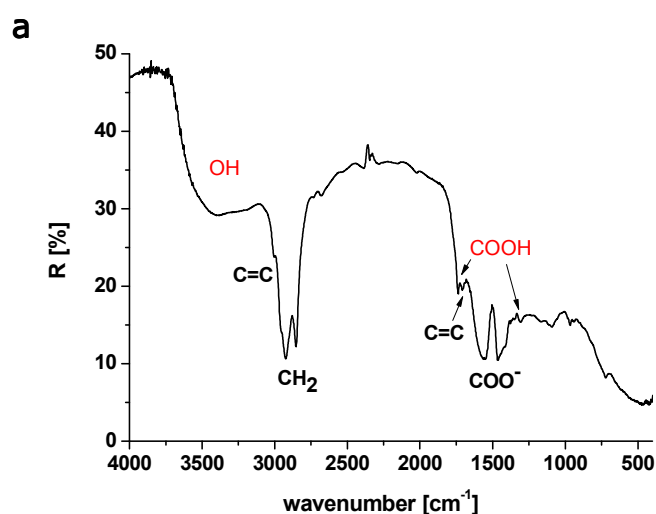
Figure 3.7: DRIFT (a) and FTIR (b) spectra of NaYF$_4$:Yb,X displaying characteristical bands of OA in its carboxylate form: 2930 and 2860 cm^{-1} (CH$_2$), 3005 and 1705 cm^{-1} (C=C), 1560 and 1475 cm^{-1} (COO$^-$). The hydroxyl stretching band above 3100 cm^{-1} and the weak signals at 1755 and 1305 cm^{-1} in the DRIFT spectrum indicate remaining carboxyl groups. The molecular structure of OA is given next to spectra (b).
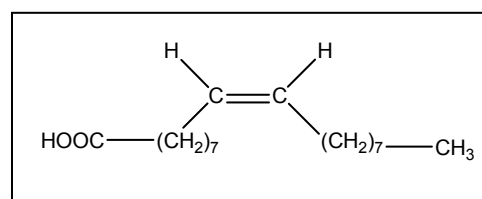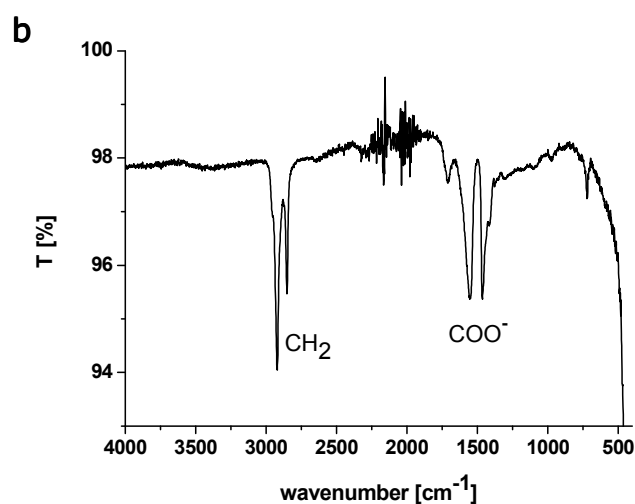
The ligand molecules on the surface of the UCLNPs were quantified by TGA. A thermogram of NaYF$_4$:Yb,X prepared via thermal decomposition is displayed in Figure 3.8. The major weight loss (8wt%) with a maximum gradient around 360 °C matches the boiling point of OA. The material itself starts to decompose above 600 °C like it was already observed in the thermogram of UCLNPs prepared by co-precipitation (Figure 3.2).
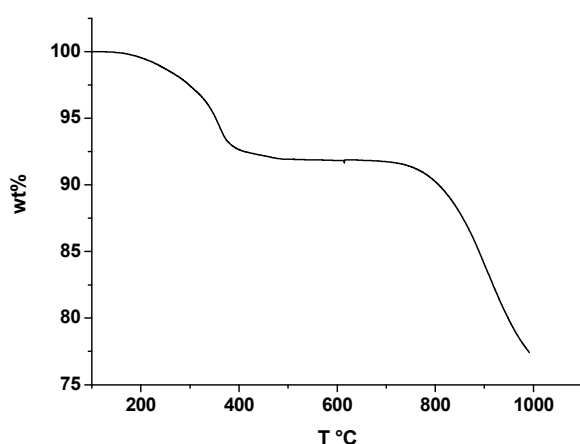
Figure 3.8: Thermogram of NaYF$_4$:Yb,X prepared by thermal decomposition. The graph reveals a major weight loss of 8wt% between 200 and 500 °C that can be assigned to OA ligands on the particle surface.

The amount of OA on the particle surface was found to be rather inconsistent (variations between 6 and 16wt%) for different batches of UCLNPs despite an identical washing procedure. The respective thermograms are given on the enclosed CD.

3.3. Co-Precipitation vs. Thermal Decomposition

There are assets and drawbacks involved in both syntheses for lanthanide doped NaYF$_4$ carried out in this work. Particles of a size from 80 to 120 nm (Figure 3.1) are obtained via the co-precipitation technique. That barely fulfils the size criterium for NPs.[24] The main advantages of this technique are the straightforward and robust procedure that allows the synthesis of about 2 g α-NaYF$_4$:Yb,X within a few hours. Another bonus is the hydrophilic nature of the particles that eliminates further surface modifications for dispersion in aqueous solutions. Nevertheless, the thermal treatment for cubic to hexagonal phase transfer is crucial regarding completeness, particle aggregation and reproducibility. As revealed from the XRD spectra in Figure 3.1, the transition from α- to β- NaYF$_4$:Yb,X is incomplete. Using higher temperatures and prolonged annealing times can drive the phase transfer further towards the hexagonal crystal structure but also leads to irreversible particle aggregation.[9,10] It is essential to heat the UCLNPs in small portions to achieve sufficient phase transfer within the solid and hence satisfying

upconversion efficiency. But the upconversion emission from different portions of β-NaYF$_4$:Yb,X derived from the same batch of α-NaYF$_4$:Yb,X usually varies in terms of brightness and the ratio of the respective emission peaks, whereas the green peak is usually less, equal or little more intense than the red peak. This is exemplarily displayed by the luminescence spectra of two portions of NaYF$_4$:Yb,Er taken from one batch after annealing at identical conditions (Figure 3.9).[25]
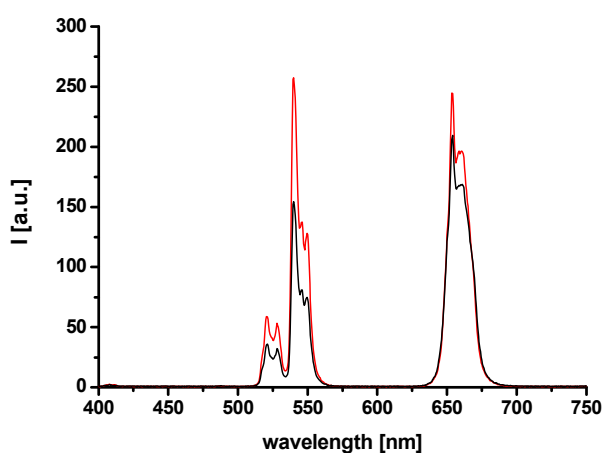
Figure 3.9: Upconversion luminescence spectra of two portions of NaYF$_4$:Yb,Er from one batch after annealing at identical conditions. The particles are inconsistent regarding brightness and ratio of the emission peaks.

NaYF$_4$:Yb,X prepared via thermal decomposition are much smaller with a well uniform size 25 to 30 nm for NaYF$_4$:Yb,Er and 34 to 40 nm for NaYF$_4$:Yb,Tm (Figure 3.5). The nanocrystals have an entirely hexagonal crystal structure (Figure 3.6) what is essential for most efficient upconversion. The reproducibility of the synthesis is highly dependent on time, temperature and especially on the intensity and time duration of the argon flow in the last step of the synthesis. A violent argon flow during the phase of heating to 300 °C reduces the volume of the reaction mixture. This results in bigger and non-uniform particles (Figure 3.10a), accelerating agglomeration (Figure 3.10b) and may culminate in complete failure of the synthesis when the argon flow is continued throughout the heating period of 1.5 h. The latter is indicated by a brownish oily residue after precipitation and washing instead of off-white, solid UCLNPs. Apart from that, uniform nanocrystals with reproducible size, peak ratios and brightness are obtained from syntheses according to the protocol given in

the Experimental PArt. Usually, 150 to 200 mg of NPs are obtained from one reaction batch. Because of the remaining OA ligands on the particle surface these are highly hydrophobic and further surface modifications are necessary to use them in aqueous solutions.
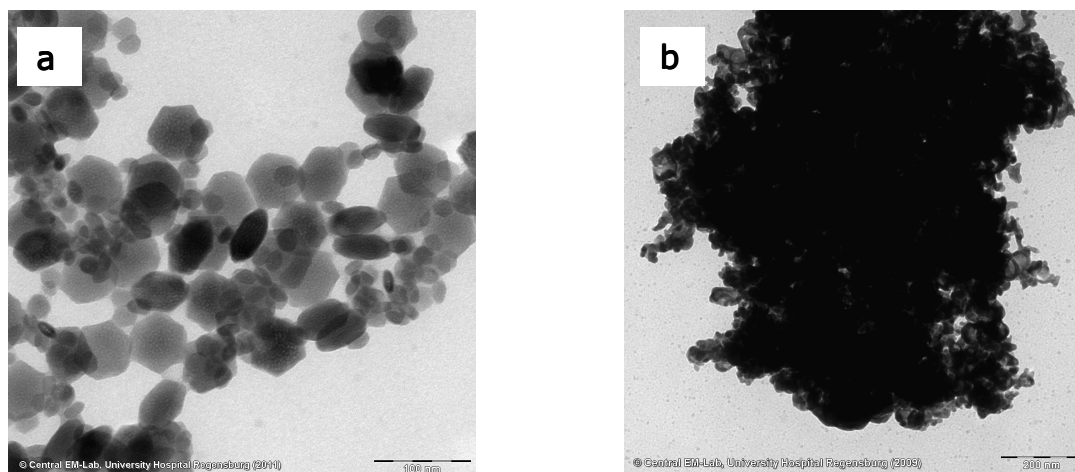
Figure 3.10: TEM pictures of UCLNPs prepared via the thermal decomposition method demonstrating the dependency of the particle size and morphology on the intensity of the argon flow in the last step of the synthesis. An enhanced argon flow continuously reduces the volume of the reaction solution resulting in bigger, non-uniform particles (a) and accelerating agglomeration (b).

It is complicated to compare the UCLNPs obtained from both methods regarding their brightness since they differ in size, phase and dispersibilty. For a rough estimation, equal amounts of NaYF$_4$:Yb,Er and NaYF$_4$:Yb,Tm prepared by the respective method were dispersed in 0.1 M hydrochloric acid (HCl). The acidic conditions allow for the dispersion of the hydrophobic UCLNPs prepared by thermal decomposition.[26] Hence, quenching effects by the solvent, what will be discussed in more detail in the next chapter, were quite the same for both particle types. The upconversion luminescent spectra are displayed in Figure 3.11. Brightness is approximately in the same range for NaYF$_4$:Yb,Er (Figure 3.11a) prepared via co-precipitation followed by thermal treatment (dashed line) and thermal decomposition (solid line). The intensity ratios of the green to the red peak are different as it was already stated above. A comparison of the spectra of NaYF$_4$:Yb,Er (Figure 3.11b) reveals that the emission of the UCLNPs prepared via thermal decomposition (solid line) is much smaller than the one from particles prepared via co-precipitation (dashed line).
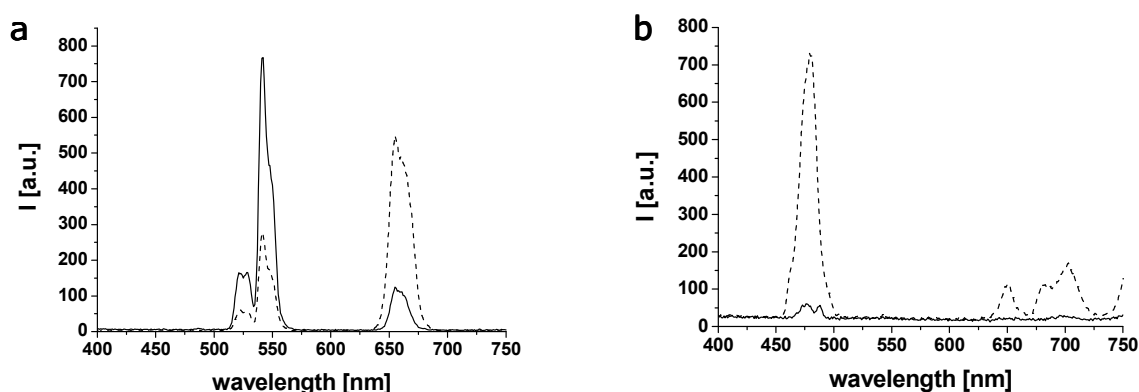
Figure 3.11: Upconversion luminescent spectra of NaYF$_4$:Yb,Er (a) and NaYF$_4$:Yb,Tm (b) prepared either by co-precipitation followed by thermal treatment (dashed lines) or thermal decomposition (solid lines) in 0.1 M HCl.

These findings can hardly be interpreted. Generally, the upconversion process is more efficient in hexagonal phase NaYF$_4$.[21,27] Hence, UCLNPs prepared in the OA-OD mixture should yield a higher emission (see Figure 3.1 and Figure 3.4). At the same time, a greater size and a smaller surface-to-volume ratio is realized for nanophosphors obtained by co-precipitation rendering them less prone to surface quenching effects. A possible explanation is that the crystal phase of the host lattice seems to exercise a greater influence on the emission of Er^{3+} than on Tm^{3+}. This hypothesis is corroborated by the fact that the peak ratios are inverted in α/β- and pure β-NaYF$_4$:Yb,Er, whereas they are consistent for NaYF$_4$:Yb,Tm (see Figure 3.3 and Figure 3.6). It is assumed that the brightness is tremendously enhanced in β-NaYF$_4$:Yb,Er compensating the stronger surface quenching effects. In contrast, the increased upconversion efficiency in β-NaYF$_4$:Yb,Tm can not counterbalance the smaller particle size.

3.4. References

1   Wang F, Liu X (2009) *Recent advances in the chemistry of lanthanide-doped upconversion nanocrystals.* Chem Soc Rev 38:976-989

2   Wang L, Li Y (2007) *Controlled Synthesis and Luminescence of Lanthanide Doped NaYF$_4$ Nanocrystals.* Chem Mater 19:727–734

3   Wang X, Zhuang J, Peng Q, Li Y (2005) *A general strategy for nanocrystal synthesis.* Nature 437:121–124

4   Liu X, Zhao J, Sun Y, Song K, Yu Y, Du C, Kong X, Zhang H (2009) *Ionothermal synthesis of hexagonal phase NaYF$_4$:Yb^{3+},Er^{3+}/Tm^{3+} upconversion nanophosphors.* Chem Commun 6628–6630

5   Haase M, Schäfer H (2011) *Upconverting Nanoparticles.* Angew Chem Int Ed 50:5808-5829

6   LaMer VK, Dinegar RH (1950) *Theorie, Production and Mechanism of Formation of Monodispersed Hydrosols.* J Am Chem Soc 72:4847-4854

7   Wang H-Q, Nann T (2011) *Upconverting Nanoparticles.* Springer Ser Fluoresc 7:115-132

8   Feng W, Sun L-D, Zhang Y-W, Yan C-H (2010) *Synthesis and assembly of rare earth nanostructures directed by the principle of coordination chemistry in solution-based process.* Coordin Chem Rev 254:1038-1053

9   Yi G, Lu H, Zhao S, Ge Y, Yang W, Chen D, Guo L-H (2004) *Synthesis, Characterization, and Biological Application of Size-Controlled Nanocrystalline NaYF$_4$:Yb,Er Infrared-to-Visible Up-Conversion Phosphors.* Nano Lett 4:2191-2196

10   Wei Y, Lu F, Zhang X, Chen D (2007) *Synthesis and characterization of efficient near-infrared upconversion Yb and Tm codoped NaYF$_4$ nanocrystal reporter.* J Alloy Compd 427:333-340

11   Sugimoto T (2007) *Underlying mechanisms in size control of uniform nanoparticles.* J Colloid Interf Sci 309:106-118

12   Xingping Z, Zhiquiang W, Shanshan L, Shunan S, Xiaqin W (2010) *Formation and Luminescence of Sodium Rare Earth Fluoride Nanocrystals in the Presence of Chelators.* J Nanosci Nanotechnol 10:2193-2202

13   Sun Y, Chen Y, Tian L, Yu Y, Kong X, Zhao J, Zhang H (2007) *Controlled synthesis and morphology dependent upconversion luminescence of NaYF$_4$:Yb, Er nanocrystals.* Nanotechnology 18:275609

14   Zeng J-H, Su J, Li Z-H, Yan R-X, Li Y-D (2005) *Synthesis and Upconversion Luminescence of Hexagonal-Phase NaYF$_4$:Yb, Er^{3+} Phosphors of Controlled Size and Morphology.* Adv Mater 17:2119-2123

15   Wendlandt W (1960) *Thermogravimetric and Differential Thermal Analysis of (Ethylenedinitrilo)tetraacetic Acid and Its Derivatives.* Anal Chem 32:848-849

16   Campbell FW, Gubisch RW (1966) *Optical quality of the human eye.* J Physiol 186:558-578

17   Chen Z, Chen H, Yu M, Li F, Zhang Q, Zhou Z, Yi T, Huang C (2008) *Versatile Synthesis Strategy for Carboxylic Acid-functionalized Upconverting Nanophosphors as Biological Labels.* J Am Chem Soc 130:3023-3029

18   Li Z, Zhang Y (2008) *An efficient and user-friendly method for the synthesis of hexagonal-phase NaYF$_4$:Yb, Er/Tm nanocrystals with controllable shape and upconversion fluorescence.* Nanotechnology 19: 345606

19   Boyer J-C, Vetrone F, Cuccia LA, Capobianco JA (2006) *Synthesis of Colloidal Upconverting NaYF$_4$ Nanocrystals Doped with Er^{3+}, Yb^{3+} and Tm^{3+} via Thermal Decomposition of Lanthanide Trifluoroacetate Precursors.* J Am Chem Soc 128:7444-7445

20   Yi GS, Chow GM (2006) *Synthesis of Hexagonal-Phase NaYF$_4$:Yb,Er and NaYF$_4$:Yb,Tm Nanocrystals with Efficient Up-Conversion Fluorescence.* Adv. Funct Mater 16:2321-2329

21   Liu C, Wang H, Li X, Chen D (2009) *Monodisperse, size-tunable and highly efficient β-NaYF$_4$:Yb,Er(Tm) up-conversion luminescent nanospheres: controllable synthesis and their surface modifications.* J Mater Chem 19:3546-3553

22   Birks LS, Friedman H (1946) *Particle Size Determination from X-Ray Line Broadening.* J Appl Phys 17:687-692

23   De Palma R, Peeters S, Van Bael MJ, Van den Rul H, Bonroy K, Laureyn W, Mullens J, Borghs G, Maes G (2007) *Surface Ligand Exchange to Make Hydrophobic Superparamegnetic Nanoparticles Water-Dispersible.* Chem Mater 19:1821-1831

24   Cademartiri L, Ozin GA (2009) *Concepts of Nanochemistry.* Wiley-VCH Verlag GmbH & Co. KGaA, Weinheim

25   Mader HS (2010) *Surface Modification of Silica Particles and Upconverting Particles Using Click Chemistry.* Dissertation, University of Regensburg

26   Bogdan N, Vetrone F, Ozin GA, Capobianco JA (2011) *Synthesis of Ligand-Free Colloidally Stable Water Dispersible Brightly Luminescent Lanthanide-Doped Upconverting Nanoparticles.* Nano Lett 11:835-840

27   Wang F, Han Y, Lim CS, Lu Y, Wang J, Xu J, Chen H, Zhang C, Hong M, Liu X (2010) *Simultaneous phase and size control of upconversion nanocrystals through lanthanide doping.* Nature 463:1061-1065

4. Surface Engineering of Upconverting Luminescent Nanoparticles

Surface engineering of UCLNPs pursues the major objectives of enhancing upconversion efficiency, tuning dispersibility and introducing functionalities on the particles for further conjugation. Within this work nanocrystals were coated with $NaYF_4$ to reduce surface quenching effects and thus to enhance their brightness. Coating with silica (SiO_2) was applied to achieve dispersibilty in aqueous solutions and to generate a platform for various functionalizations via silanization. Additionally, simple ligand exchange reactions were used to change particle dispersibility and to introduce surface functionalities.

4.1. Core-Shell Upconverting Luminescent Nanoparticles: Synthesis of $NaYF_4$:Yb,X@$NaYF_4$ (X = Er^{3+}, Tm^{3+})

Compared to their bulk counterpart materials, UCLNPs exhibit significantly lower upconversion efficiency. Activator ions located at the particle surface are in close contact with surface ligands and solvent molecules that can act as quenchers. This becomes more and more evident at smaller particle sizes since the surface-to-volume ratio increases. Hence, statistically more activators are close to the particle surface and prone to quenching effects. The quenching is even increased in aqueous solutions due to the high energy stretching vibrations of water.[1,2] This is a predicament since especially for biological applications a smaller particle size is favored yet an aqueous environment is essential. The strategy to reduce surface quenching is shielding off the emitting lanthanide ions on the interface by growing an inactive, i.e. not activator doped, shell of host material around an active lanthanide doped core.[3,4,5]

A shell of $NaYF_4$ was grown around a core of $NaYF_4$:Yb,X (X = Er^{3+}, Tm^{3+}) in a modification of the protocol for seed-mediated synthesis of $NaYF_4$:Yb,Er@$NaGdF_4$ by Guo et al.[6] Lanthanide doped core particles were synthesized via thermal decomposition (see chapter 3.2) and used as

seeds in a thermal decomposition synthesis of $NaYF_4$. TEM pictures of the UCLNPs before and after coating are displayed in Figure 4.1.
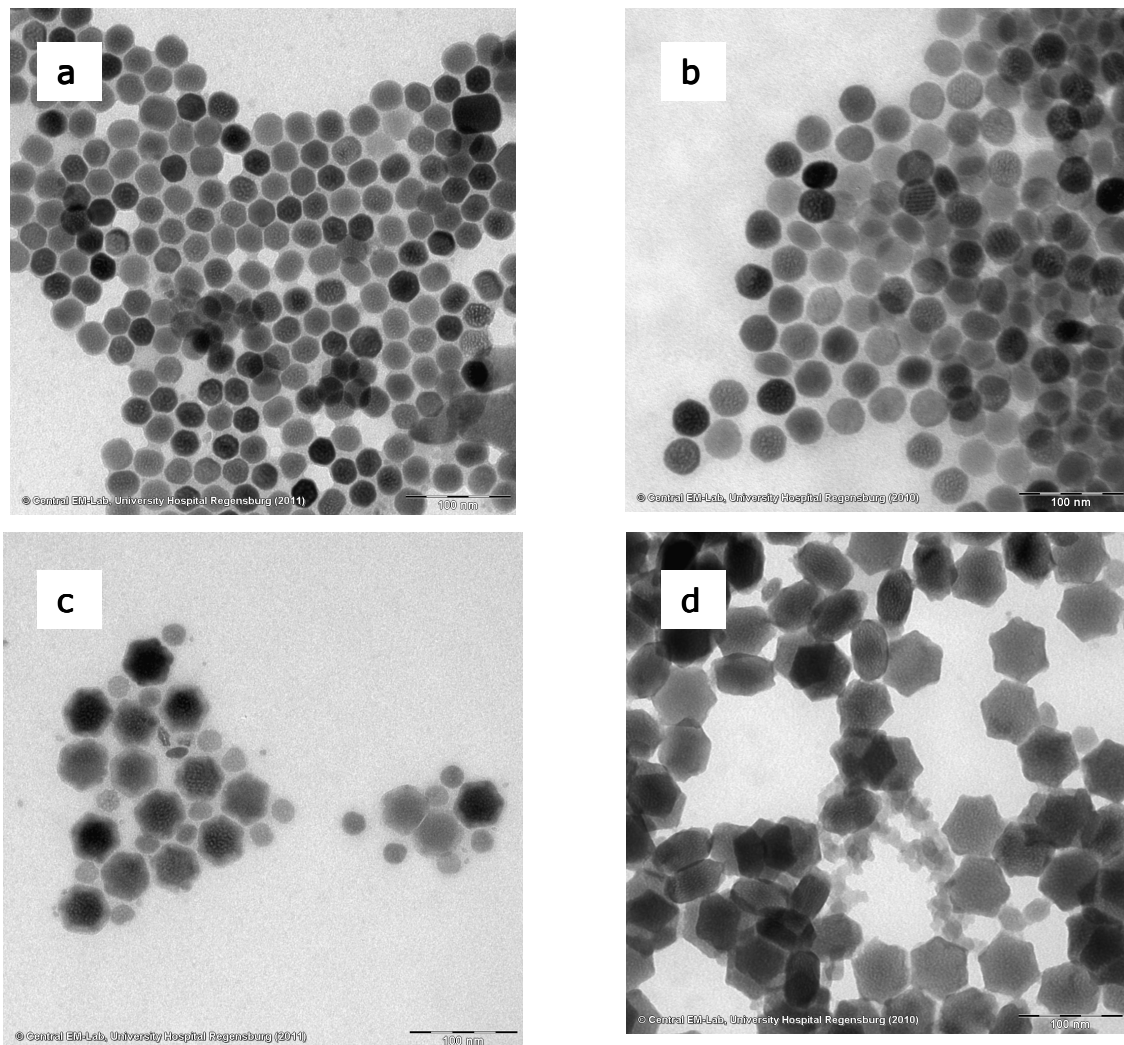
Figure 4.1: TEM pictures of $NaYF_4$:Yb,Er(a) and $NaYF_4$:Yb,Tm(b) synthesized via thermal decomposition. The particles were coated with a shell of $NaYF_4$ by seed-mediated thermal decomposition. The average particle size increased from about 27 (a) to 47 nm for Er^{3+}-doped seeds and second nucleation of $NaYF_4$ can be observed (c). New particle formation occurred to a lesser degree in the synthesis of $NaYF_4$:Yb,Tm@ $NaYF_4$ resulting in a thicker shell of 10 to 15nm (d). NPs are shown in100,000x magnification, the length of the scale bars is 100 nm.

It was stated before that $NaYF_4$:Yb,Tm core particles (Figure 4.1b) were found to be bigger than Er^{3+}-doped seeds (Figure 4.1a). Also the shell growth is not consistent for both particle types. The same procedure results in deposition of 10 nm $NaYF_4$ on $NaYF_4$:Yb,Er (Figure 4.1c) increasing the average particle size from 27 to 47 nm. A slightly thicker shell of 10 to 15 nm was grown around $NaYF_4$:Yb,Tm resulting in core-

shell UCLNPs of about 65 nm. Second nucleation takes place alongside shell growth. It is indicated by the occurrence of small NPs between the core-shell particles. Only a few small amorphic particles are formed during coating of $NaYF_4$:Yb,Tm (Figure 4.1d), whereas many $NaYF_4$-nuclei were found after coating of $NaYF_4$:Yb,Er (Figure 4.1c). These particles are uniform and smaller (23 nm) than the original seed particles. Hence, they cannot be comprised of the doped material.

The XRD spectra of core and core-shell UCLNPs are shown below. At the top, the spectrum reveals the hexagonal phase of the particles (compare ICDD pattern 28-1192 in Figure 3.4). The peaks in the spectrum of $NaYF_4$:Yb,X@$NaYF_4$ at the bottom appear at the same angles but are even more distinct. Hence, $NaYF_4$ in its hexagonal phase is grown on the UCLNP seeds.
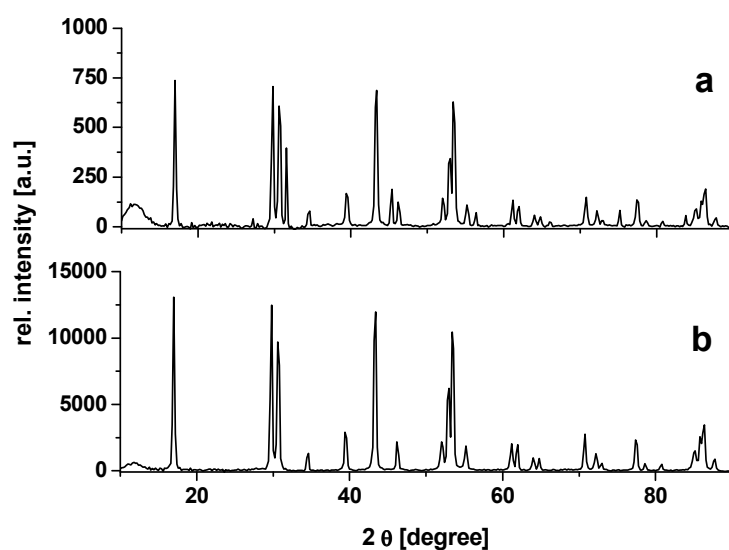
Figure 4.2: XRD spectra of $NaYF_4$:Yb,X (a) and $NaYF_4$:Yb,X@$NaYF_4$ (b) UCLNPs. A shell of hexagonal phase $NaYF_4$ is grown around the particle seeds.

Luminescence is efficiently enhanced as can be seen in the emission spectra of green or blue emitting core and core-shell UCLNPs. A consistent 6-fold increase was recorded for the green and red emissions according to the spectra of $NaYF_4$:Yb,Er compared to $NaYF_4$:Yb,Er@$NaYF_4$ in cyclohexane (Figure 4.3a). The blue luminescence of $NaYF_4$:Yb,Tm@$NaYF_4$ at 475 nm was found to be even 10 times higher in contrast to $NaYF_4$:Yb,Tm. There was a 5-fold and 3-fold enhancement for the red emissions at 646 and 696 nm, respectively.
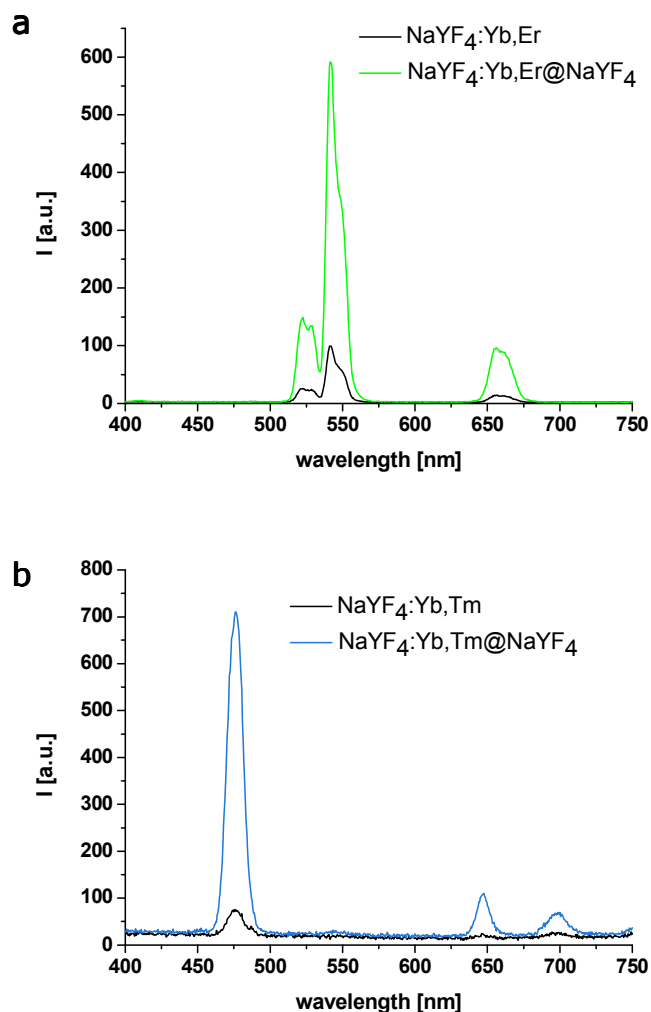
Figure 4.3: Luminescence spectra of 0.1wt% core and core-shell UCLNP dispersions in cyclohexane after excitation with a 980 nm CW diode laser. The emission peaks of NaYF$_4$:Yb,Er undergo a consistent 6-fold increase after coating with NaYF$_4$ (a). The enhancement of the emission peaks at 475, 646 and 696 nm for NaYF$_4$:Yb,Tm@NaYF$_4$ compared to NaYF$_4$:Yb,Tm was 10-, 5- and 3-fold, respectively (b).

Core and core-shell UCLNPs were transferred from cyclohexane into water. This allows for testing the efficiency of shielding of the core against solvent molecules by the NaYF$_4$ shell. The particles were rendered hydrophilic via a ligand exchange reaction in which the OA ligands on the surface are substituted for citric acid. This kind of surface modification will be discussed in the next section. Figure 4.4 offers a comparison of the luminescence spectra of 0.1wt% dispersions of the core and core-shell UCLNPs in cyclohexane and water. The upconversion emission is efficiently enhanced for NaYF$_4$:Yb,Er@NaYF$_4$ upon coating (Figure 4.4a black and green line; see also Figure 4.3a). Yet the quenching by water molecules is insufficiently suppressed (Figure 4.4a, grey and red line), whereas the green and the red peaks are not equally quenched. The emission of NaYF$_4$:Yb,Tm@NaYF$_4$ is also enhanced by coating (Figure 4.4b, black and

blue line) as it has already been shown in Figure 4.3b. For this type of particles in contrast the shielding from solvent molecules after coating with NaYF$_4$ is virtually complete (Figure 4.4b, grey and red line).
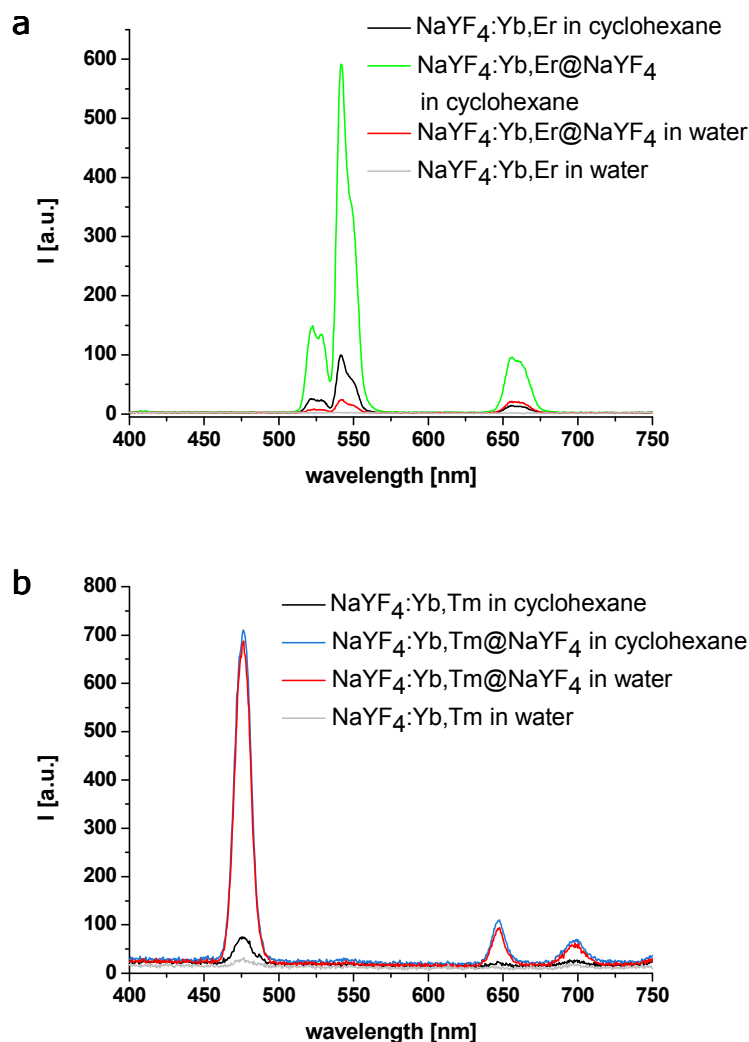
Figure 4.4: Upconversion luminescence spectra of 0.1wt% core and core-shell UCLNP dispersions in cyclohexane and water. The emission peaks of NaYF$_4$:Yb,Er@NaYF$_4$ (green line) are increased compared to the core particles (black line). Upon transfer from cyclohexane to water insufficient shielding becomes apparent (red and grey line) (a). The enhancement of the upconversion emission for NaYF$_4$:Yb,Tm@NaYF$_4$ (black line) compared to NaYF$_4$:Yb,Tm (blue line) is consistent even after changing the solvent from cyclohexane to water (red line) whereas core particles in water are prone to quenching (grey line) (b).

A closer look at the TEM pictures of the core-shell particles in Figure 4.1c and d reveals that a really continuous and dense shell of NaYF$_4$ is formed around Tm^{3+}-doped UCLNP seeds (Figure 4.5b). On the contrary, the shell around Er^{3+}-doped cores seems to be discontinuous and porous (Figure 4.5a). This explains the fact that upconversion emission is efficiently enhanced (Figure 4.3a) but quenching by water solvent molecules is insufficiently hampered (Figure 4.4a). Further, it is in accordance with the larger number of NaYF$_4$ particles formed by second nucleation in the

synthesis of $NaYF_4$:Yb,Er@$NaYF_4$ (Figure 4.1). The coating material rather grows to small particles than to a shell around the seeds.
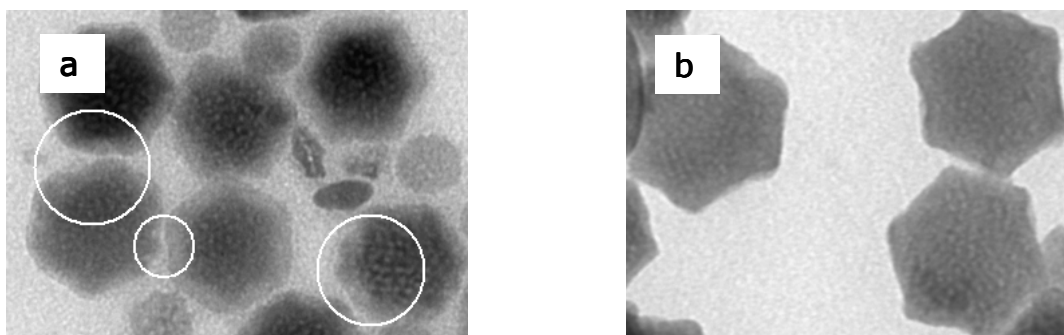
Figure 4.5: Magnification of the TEM pictures of core-shell $NaYF_4$:Yb,Er@$NaYF_4$ (a) and $NaYF_4$:Yb,Tm@$NaYF_4$ (b). The white spheres in (a) mark porous and discontinuous parts in the shell of Er^{3+}-doped seeds. This entails incomplete shielding from solvent molecules. In contrast, a complete shell is formed around Tm^{3+}-doped seeds (b).

Repeated syntheses have proven the diverging results for Er^{3+} and Tm^{3+}-doped seeds. The discrepancy between the diameters of the seed (Figure 3.5) may influence Ostwald ripening which is the general driving force for shell growth.[7] After nucleating of the coating material according to LaMer,[8,9] the $NaYF_4$-nuclei are smaller than the seed particles ($NaYF_4$:Yb,X). They dissolve and the material is deposited on the seeds resulting in the formation of the core-shell material ($NaYF_4$:Yb,X@$NaYF_4)$. It is assumed, that the tendency for dissolution and shell growth is weaker for a smaller difference in size between seeds and nuclei.

4.2. Ligand Exchange Reactions

Procedures to tune the dispersibilty of UCLNPs and to introduce functionalities to their surface are often combined. There are diverse protocols for the surface modification of all kinds of NPs. It is important to know about the surface characteristics of the material that has to be coated. UCLNPs prepared by co-precipitation exhibit hydrophilic behavior whereas those synthesized by thermal decomposition are hydrophobic. In general, the crystal lattice of the UCLNPs in this work consists of Na^+, Y^{3+} and F^- ions. Additionally, trivalent lanthanides of the sensitizer and the

activator ions are included. Thus, coordination by ligand molecules like EDTA, OA or OAm during synthesis is based on the interaction between the cations and the carboxylate or amino groups of the capping agent.

One type of surface modification for tuning solubility and introducing functionalities on NaYF$_4$ is based on these electrostatic interactions. So called ligand exchange (LE) reactions can be performed on UCLNPS that were prepared by thermal decomposition in order to substitute the OA on the particle surface. This has already been demonstrated with comparatively small molecules like hexanedioic acid,[10] as well as with polymers like polyacrylic acid,[11] polyethylene glycol phosphonate,[2] or polyvinylpyrrolidone.[12] These exchange reactions yielded hydrophilic from formerly hydrophobic NPs. By the deposition of bifunctional or multifunctional molecules on the particles, non-coordinating functionalities can be used for further bioconjugation.[10] Further, chemical modification of the OA ligands by oxidation can be accomplished thus rendering the NPs water dispersible and creating carboxy functionalities on the surface.[13]

Exchange reactions were performed by stirring UCLNPs that were prepared via thermal decomposition with an excess of the new ligand in an appropriate solvent or a solvent mixture at elevated temperature. The ligand that is desired to be deposited on the particles is required to be soluble in the solvent used. Further, the NPs have to be well dispersible therein. After this process, UCLNPs bearing the applied ligand were precipitated from the mixture and washed by repeated centrifugation-washing cycles to remove OA and excess exchange reagent. During the work for this thesis, it was found that the deposition of multifunctional polymers on UCLNPs prepared via thermal decomposition is little promising when monodispersible particles are requested. Crosslinking and flocculation occurs with long-chain polymers carrying several functional groups like polyethylenimine. Simultaneous coordination of the polymer to the surface of several particles can hardly be controled. A possible solution for this dilemma is substituting OA for small ligands in order to prevent

agglomeration and to yield the desired surface properties. On the basis of Lattuada's and Hatton's approach who performed several LE reactions on magnetic NPs,[14] OA molecules on UCLNPs were exchanged for ricinoleic acid (RA) and citric acid (CA). The main goal was to transfer the particles from apolar to polar solvents. It should be mentioned that a certain amount of OA might remain on the surface after LE since the reactions are based on a competitive process between the original and the desired ligand.

LE with RA yielded UCLNPs that were well dispersible in polar aprotic solvents like THF (tetrahydrofuran). Figure 4.6 displays DRIFT (Figure 4.6a) and FTIR spectra (Figure 4.6b) of the particles before (UCLNP@OA) and after the procedure (UCLNP@RA).
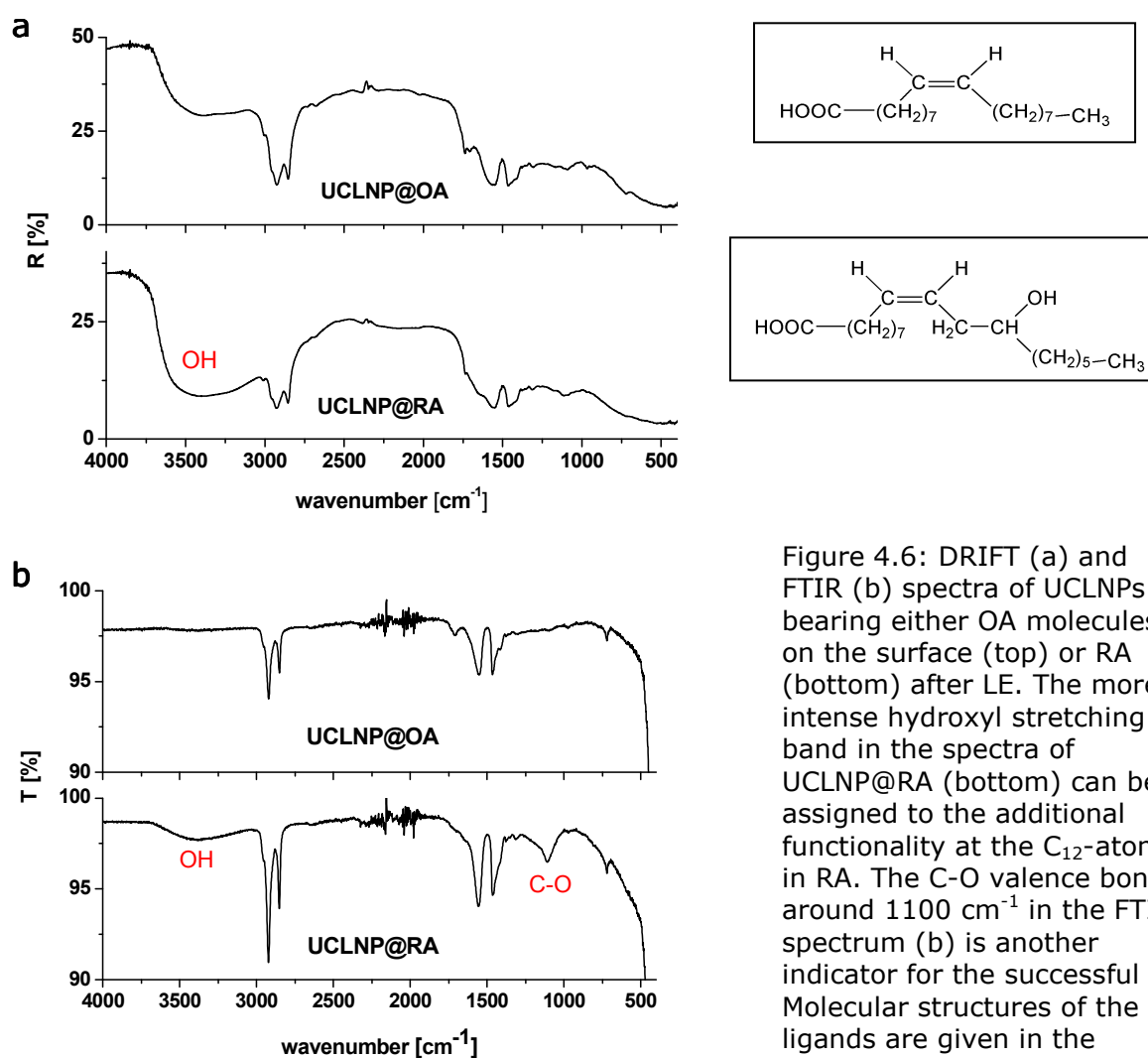
Figure 4.6: DRIFT (a) and FTIR (b) spectra of UCLNPs bearing either OA molecules on the surface (top) or RA (bottom) after LE. The more intense hydroxyl stretching band in the spectra of UCLNP@RA (bottom) can be assigned to the additional functionality at the C_{12}-atom in RA. The C-O valence bond around 1100 cm^{-1} in the FTIR spectrum (b) is another indicator for the successful LE. Molecular structures of the ligands are given in the frames next to (a).

The DRIFT and FTIR spectra of particles bearing OA on the surface were already discussed in section 3.2 (Figure 3.7a, b). The molecular structure of RA differs from that of OA by an additional hydroxyl group only (Figure 4.6). Hence, the spectra are quite similar except the hydroxyl band above 3100 cm^{-1} and the distinct C-O valence band of the secondary alcohol around 1100 cm^{-1} in the FTIR spectra (Figure 4.6b).

The same reaction was performed with CA as the exchange ligand. Thus, particles could be transferred from cyclohexane into aqueous solution. This was likewise carried out for the investigations on core-shell UCLNPs in section 4.1. CA is a tricarboxylic acid i.e. three functional groups can principally coordinate the cations on the particle surface. At least some of the carboxy functionalities should be available for further conjugation. However, attemps to attach aminofluorescein as a test molecule on UCLNP@CA have failed. The reaction was carried out via well established peptide coupling chemistry (DCC/NHS-activation of the carboxy groups)[15] followed by either dialysis of the reaction mixture or repeated centrifugation-washing-cycles to remove unreacted reagents. Neither the yellow color nor any fluorescence of aminofluorescein could be observed by the eye or by fluorimetry after the purification procedures. DRIFT (Figure 4.7a) and FTIR spectra (Figure 4.7b) proved a successful exchange of OA with CA. The distinct peaks at 2930 and 2860 cm^{-1} arising from the long hydrocarbon chains in OA are much smaller in the spectra of UCLNP@CA. The increased band above 3100 cm^{-1} and the distinct peak around 1100 cm^{-1} in the FTIR spectrum of UCLNP@CA (Figure 4.7b) can clearly be assigned to the hydroxyl group. Yet from the DRIFT spectrum taken of UCLNPs after reaction with aminofluorescein and dialysis (Figure 4.7a) it was found that there are hardly any ligand molecules left on the particles. It is suggested that after coupling of the test molecule to the CA ligands on the NP surface the conjugate of CA and the fluorophore is removed by the purification process.
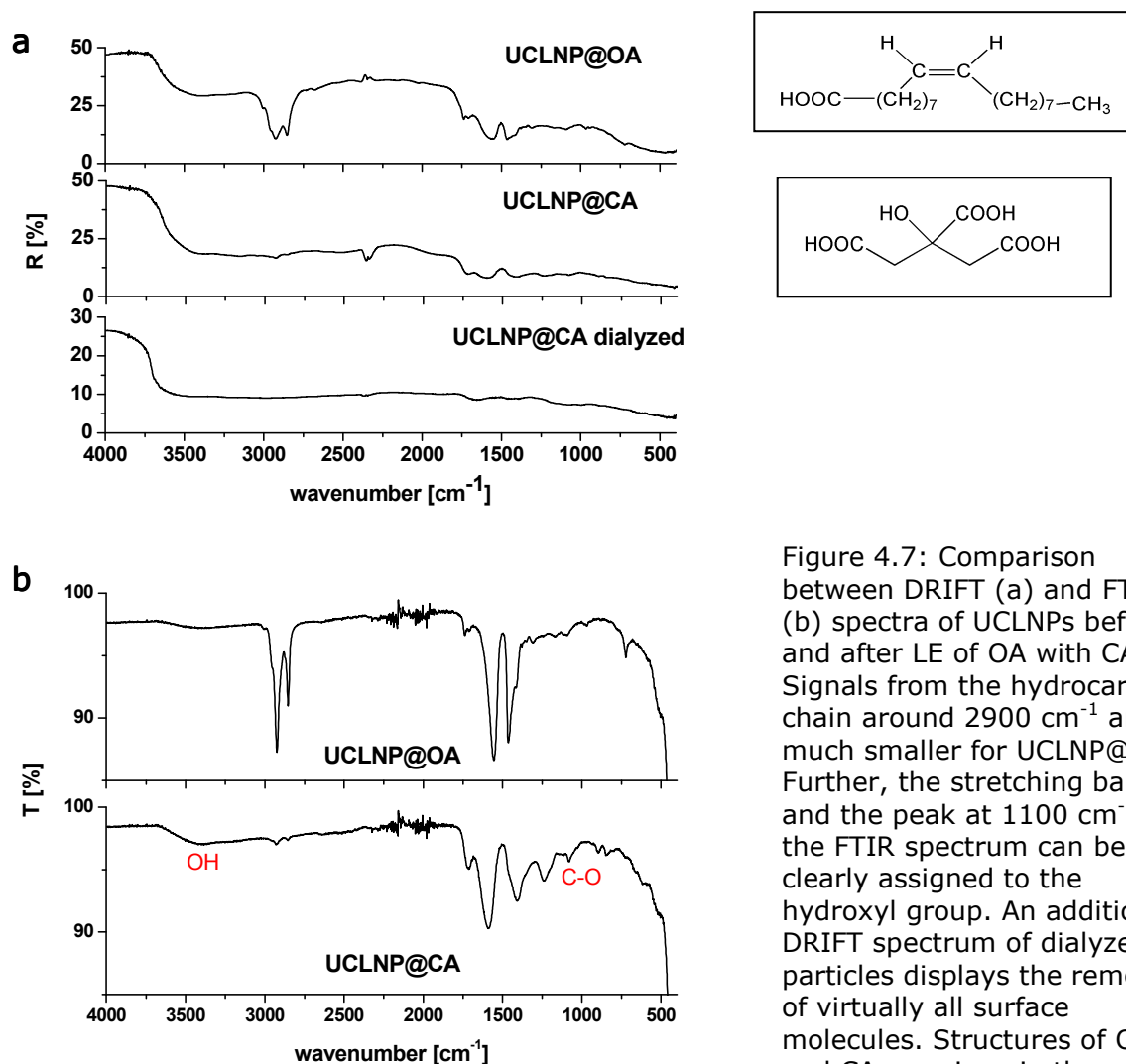
Figure 4.7: Comparison between DRIFT (a) and FTIR (b) spectra of UCLNPs before and after LE of OA with CA. Signals from the hydrocarbon chain around 2900 cm^{-1} are much smaller for UCLNP@CA. Further, the stretching band and the peak at 1100 cm^{-1} in the FTIR spectrum can be clearly assigned to the hydroxyl group. An additional DRIFT spectrum of dialyzed particles displays the removal of virtually all surface molecules. Structures of OA and CA are given in the frames next (a).

Hence, the electrostatic interaction between the carboxylic acids and the UCLNP surface is strong enough to stabilize the particles in different solvents but the surface ligands are not suitable for a stable coupling between UCLNPs and small molecules like fluorophores, maleimide or biotin for example. Nevertheless, LE reactions are straightforward and well suited for transferring UCLNPs in various solvents. UCLNP@CA for example were further investigated by Andreas Sedlmeier within his master thesis and applied for luminescent sensing of temperature in aqueous media.[16]

4.3. Coating of Upconverting Luminescent Nanoparticles with Silica – A Platform for Various Functionalizations

Another common approach towards surface engineering of NPs is encapsulation in a matrix of silica. Instead of electrostatic interaction between particle surface and ligand molecules, rather a shell is grown around NPs via polymerization of monomers. Once this is done, silica surfaces offer the possibility for various functionalizations via condensation of their free silanol groups with organosilanes what is commonly known as silanization. Additionally, silica or silica coated NPs are well dispersible in water and highly biocompatible.[17,18] In general there are two major methods for silica shell growth that are based on two common synthetic procedures for the formation of silica NPs: the Stöber method[19] and water-in-oil (W/O) microemulsion.[20]

4.3.1. The Stöber Method: Coating of Hydrophilic Nanoparticles

The coating procedure derived from the Stöber method[19] is carried out in aqueous alcoholic solution. The silica precursor tetraethoxysilane (TEOS) is hydrolyzed by alkaline catalysis with ammonia thus forming monosilicic acid. The acid is stable only in small concentrations in aqueous solutions and has a strong tendency towards intermolecular condensation.[21] This usually ends up in the formation of silica NPs or alternatively the growth of a silica shell on seed particles if these are available in the reaction mixture. This method can be applied to various particles,[22,23,24] whereas the unique requirement for successful and uniform silica coating is good dispersibility of the seed particles in the aqueous alcoholic solution. Hence, the procedure is suited to coat the particles prepared via co-precipitation followed by thermal treatment (see section 3.1). TEM pictures of the NPs coated likewise are presented in Figure 4.8 in different magnifications. The Stöber method yielded rather multiple than single encapsulated particles (Figure 4.8a). This could not be improved in repeated syntheses and it might be due in some parts to agglomerates which are formed during the

thermal treatment in the synthesis of the particles (Figure 3.1). The thickness of the silica shell was found to be around 45 nm (Figure 4.8b).
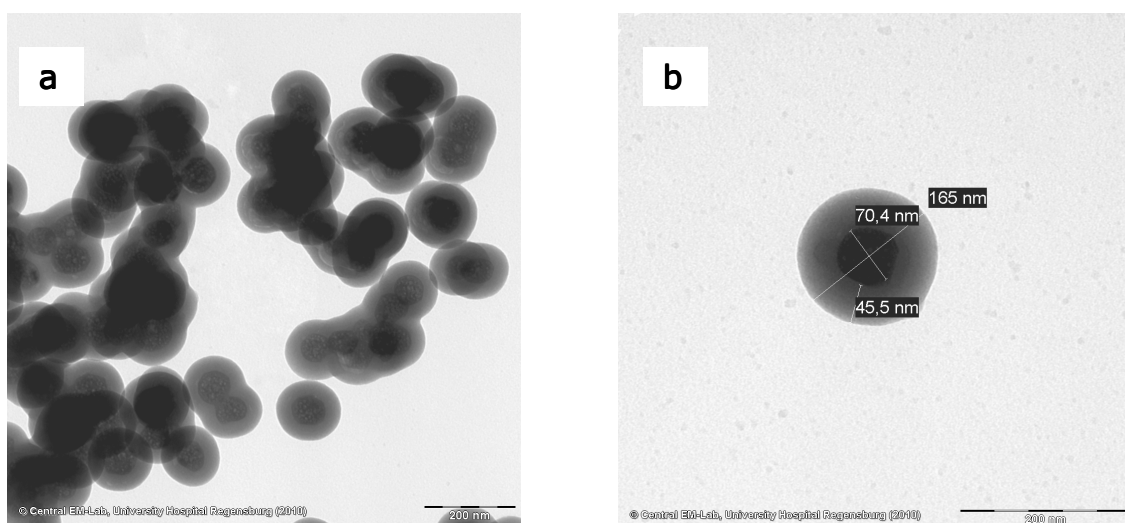
Figure 4.8: TEM pictures of UCLNPs synthesized via co-precipitation followed by thermal tretament and coated with a matrix of silica by the Stöber process. UCLNP@SiO$_2$ in 40,000x (a) and 80,000x magnification (b); the length of the scale bars is 200 nm.

Heike Mader intensly studied the silica coating of hydrophilic UCLNPs and their surface functionalization for use in click chemistries[25,26] thus it is not part of this work.

4.3.2. Water-in-Oil Microemulsion: Coating of Hydrophobic Nanoparticles

Silica coating via W/O, also called reverse microemulsion is generally applied to hydrophobic NPs like the UCLNPs derived from thermal decomposition (see section 3.2). In the synthesis according to the protocol of Jalil et al.,[18] the UCLNPs are dispersed in cyclohexane ("oil") together with the non-ionic surfactant Igepal CO-520 and a small amount of aqueous ammonia solution. After sonication the silica precursor TEOS is added and the mixture is stirred at room temperature for two days. There is no description for the mechanism of silica coating of UCLNPs in reverse microemulsion available. Investigations on QDs by Koole et al.[27] revealed that upon sonication first a LE between the OA on the particle surface and the hydrophilic headgroup of the surfactant molecules occurs. It has been established from the mechanism for silica particle formation in W/O

microemulsion[28] that further micelles containing water and ammonia are formed. TEOS is located at the interfaces between the surfactant and the UCLNPs or the water phase. The cations of the UCLNP surface can also be coordinated by the hydroxyl groups of partially or completely hydrolyzed precursor molecules. This allows for the transfer of the particles from the oil phase to the micelles by LE. Hydrolysis of TEOS and polymerizarion of the thus formed monosilicic acid takes place at the interface and results in the encapsulation of the particles in a matrix of silica.[27,28] UCLNP@SiO$_2$ are precipitated by the addition of acetone and washed by repeated centrifugation-washing cycles.

TEM pictures of the formed UCLNP@SiO$_2$ are given in Figure 4.9. More single coated NPs are obtained compared to the particles obtained by co-precipitation and coating via the Stöber method (Figure 4.8).
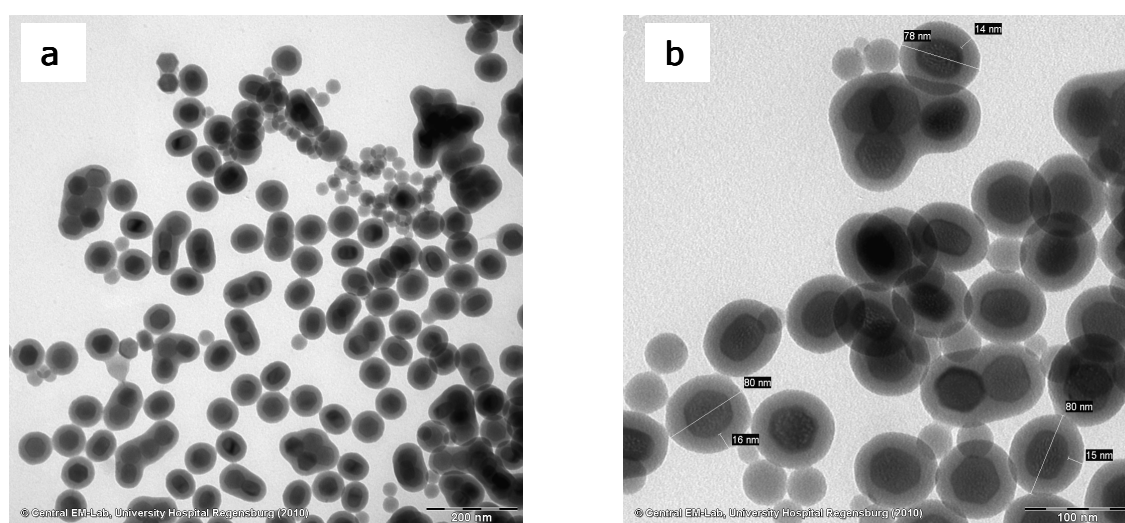
Figure 4.9: TEM pictures of UCLNPs synthesized via thermal decomposition and coated with a matrix of silica by a reverse microemulsion display the UCLNP@SiO$_2$ in 40,000x magnification with a scale bar of 200 nm (a) and 100,000x magnification with a scale bar of 100 nm (b).

The uniform silica shell (15 nm) resulted in an overall particle size below 100 nm. Second nucleation of SiO$_2$ leads to the formation of few silica NPs with a size around 30 nm. A distinct quenching of the upconversion emission upon silica coating and transfer in water was observed which can hardly be quantified due to the differences in mass of UCLNPs and UCLNP@SiO$_2$. The decrease in luminescence is reasonably due to surface

quenching effects caused by silanol groups of the silica shell (similar quenching effects have already been discussed in section 4.1).

In summary, hydrophobic UCLNPs synthesized by thermal decomposition are generally of smaller size than hydrophilic particles from co-precipitation (see section 3.3). The same holds for the respective silica capsules. Further, the possibility to increase the brightness or rather to shield their surface from quenching effects (see section 4.1) and the better uniformity renders them superior candidates for applications as labels or imaging agents. In the following these particles are referred to as UCLNP@SiO$_2$ without giving the explicit method of preparation.

4.3.3. Surface Functionalization of Silica Coated Upconverting Luminescent Nanoparticles

The surface of UCLNP@SiO$_2$ was further modified by silanization with different functionalities. Therefore, diverse reactive organosilanes were added to the microemulsion after one day and the reaction was continued as described above. Like TEOS, the reactive groups of the silanes are hydrolyzed in the water phase. Incorporation in the silica shell occurs via co-polymerization with the monosilicic acid. Table 1 summarizes the functional silanes used in the syntheses and the notation of the corresponding particles. Functionalities for common bioconjugation techniques like azide and alkyne for click chemistry,[29,30,31] maleimide and amino groups were chosen.[15] Various other alkoxy- or chlorosilanes may also be used. Integration of the silanes in the silica shell was investigated by DRIFT spectroscopy and comparison of the zeta potentials. Possible particle agglomeration was examined by TEM and photon correlation spectroscopy (PCS) also called dynamic light scattering (DLS). The reports of the zeta potential measurements and PCS can be found on the enclosed CD.
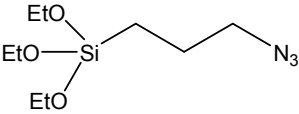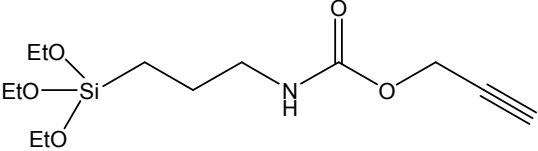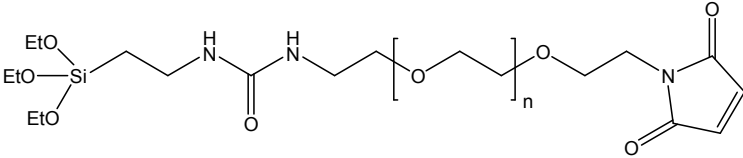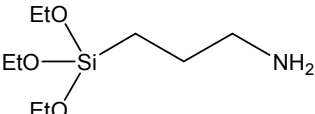
Organosilane used for surface functionalization	Particle notation
(3-azidopropyl) triethoxysilane (AzPTES)	UCLNP@SiO$_2$-N$_3$
O-(propargyloxy)-N-(triethoxy-silylpropyl)urethane (AlkyneTES)	UCLNP@SiO$_2$-CCH
silane polyethylene glycol maleimide (Silane-PEG-Mal)	UCLNP@SiO$_2$-PEG-Mal
(3-aminopropyl) triethoxysilane (APTES)	UCLNP@SiO$_2$-NH$_2$

Table 1: Summary of the reactive organosilanes that were used for surface functionalization of UCLNP@SiO$_2$.

Azide and Alkyne Moieties for Click Chemistry

The term "click chemistry" refers to some bioorthogonal reactions which allow for the specific and straightforward conjugation of molecules.[32] This concept had a great impact in diverse fields of research like material science, drug discovery and bioconjugation.[29,30] The most common example is the copper catalyzed 1,3-dipolar cycloaddition of azides and alkynes.[33] DRIFT spectra of UCLNP@SiO$_2$ functionalized with appropriate silanes (see Table 1) for this "click reaction" are displayed in Figure 4.10.
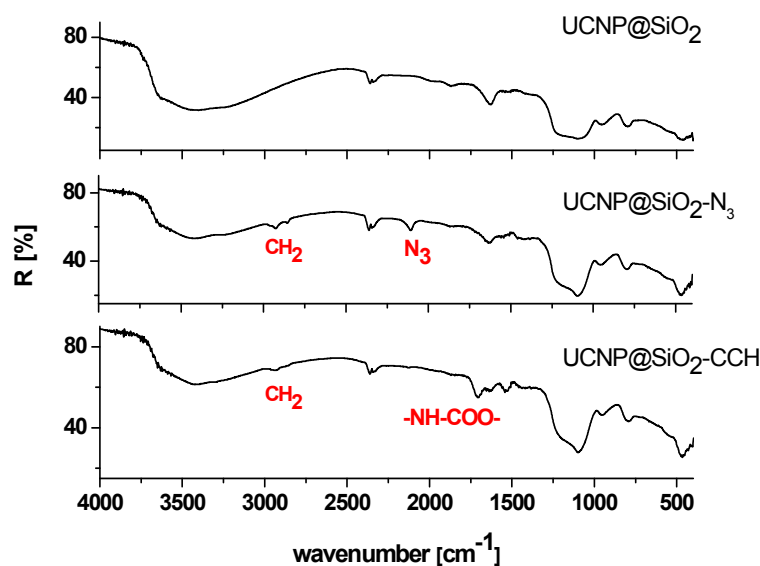
Figure 4.10: DRIFT spectra of UCLNP@SiO$_2$ compared to azide (UCLNP@SiO$_2$-N$_3$) and alkyne (UCLNP@SiO$_2$-CCH) functionalized particles. Characteristical peaks of the azido group (2110 cm^{-1}), the alkyl chains (2930, 2850 cm^{-1}) and the peptide bond in the chain of the AlkyneTES (1700 cm^{-1}) indicate the successful surface functionalization.

The IR signals from the functional moieties were found to be quite weak. Nevertheless, the characteristical peak of the azido group at 2110 cm^{-1} and the signals of the propyl chain around 2930 and 2850 cm^{-1} clearly indicate the presence of the azido silane on the UCLNP surface. The same holds for the peaks at approximately 2930 and 1700 cm^{-1} in the spectrum of UCLNP@SiO$_2$-CCH.

These results were further confirmed by the zeta potentials of the UCLNPs in deionized water (pH = 5). Particles coated with pure silica revealed a potential of -21.3 mV, whereas UCLNP@SiO$_2$-X (X = N$_3$, CCH) feature values of -11.1 and -6.2 mV respectively. Generally, silica surfaces are negatively charged at pH values above 2 due to their surface silanol groups and have negative zeta potentials.[34] The absolute value of the latter is decreased upon functionalization with uncharged functional groups which reduce the number of surface silanol groups and disturb the electrostatic repulsion between the particles. The impact of surface functionalization on particle agglomeration was further investigated by TEM and DLS. The hydrodynamic diameter of UCLNP@SiO$_2$ was determined to be 206 nm with a polydispersity index (PI) of 0.24 by PCS. The mean diameter measured with PCS is much bigger than the size of single encapsulated particles found by TEM (see Figure 4.9). On the one hand this is due to the fact that not the actual but rather the

hydrodynamic diameter is measured with DLS which is generally larger.[35] On the other hand the bigger multiple encapsulated particles also contribute to the measurement. Hence, changes in the PI served as an indicator for particle aggregation rather than the diameter obtained from PCS. Upon surface modification the measured diameters decreased to 174 nm (PI = 0.26) and 181 nm (PI = 0.17) for azide and alkyne functional moieties. The decrease in size is most probable due to a change in the hydrodynamic diameter upon functionalization. The quite consistent PI reveal no major agglomeration, whereas the TEM pictures of UCLNP@SiO$_2$-N$_3$ (Figure 4.11a) and UCLNP@SiO$_2$-CCH (Figure 4.11b) indicate more aggregation for alkyne modified NPs.
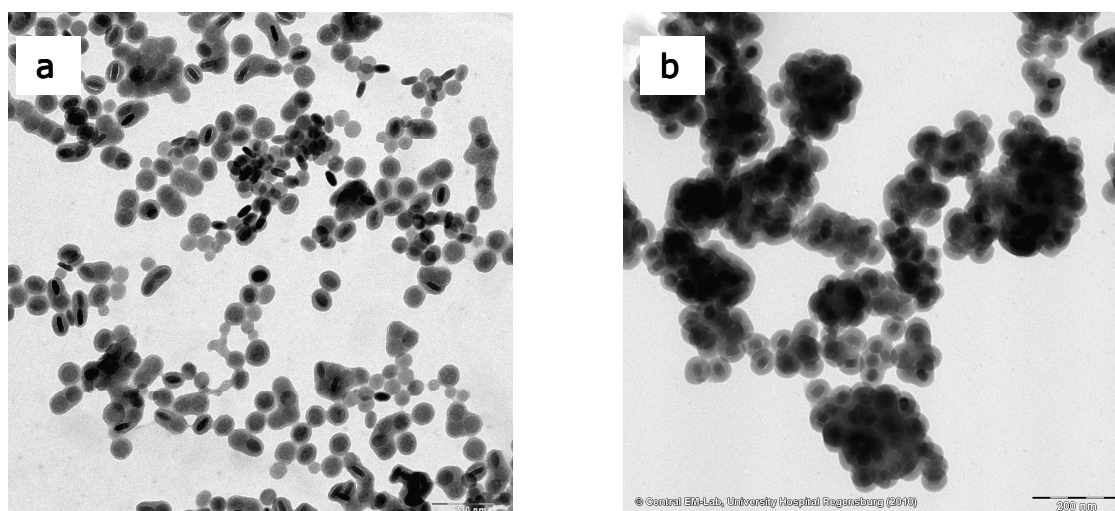
Figure 4.11: TEM pictures of UCLNP@SiO$_2$-N$_3$ (a) and UCLNP@SiO$_2$-CCH (b) in 40,000x magnification. The length of the scale bars is 200 nm.

To demonstrate the practicability of click reactions on the surface of UCLNP@SiO$_2$-N$_3$ and UCLNP@SiO$_2$-CCH, a fluorophore functionalized with the respective click moiety was conjugated to the particles via the copper catalyzed 1,3-dipolar cycloaddition of azides and alkynes (Figure 4.12). Excess reactants were removed by repeated centrifugation-redispersion cycles. Blank samples were prepared by performing the same procedure without addition of copper catalyst.
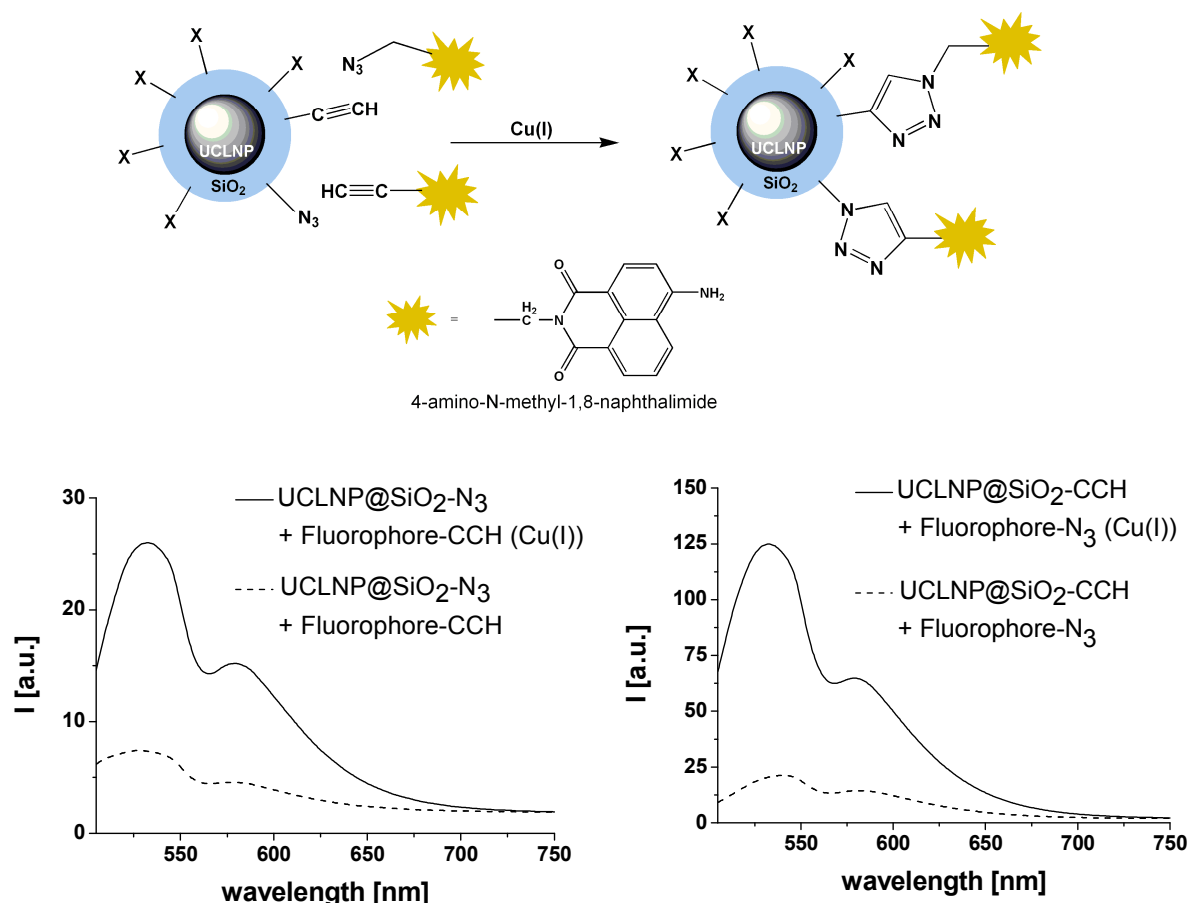
Figure 4.12: Schematic representation of copper catalyzed click conjugation of complementary fluorophores to the surface of UCLNP@SiO$_2$-X (X = N$_3$, CCH). The fluorescence spectra of 1wt% solutions of the likewise prepared particles in water (full line) and particles from the control experiment (dashed line) upon excitation of the fluorophore at 440 nm are depicted below the scheme.

The fluorescence spectra of the labeled particles upon excitation of the fluorophore at 440 nm are also displayed in Figure 4.12. The experiments without addition of copper resulted in distinct lower luminescence of the conjugate. The remaining fluorescence is due to some unspecific binding of the dye to the silica surface.[36]

Maleimide as a Thiol-Reactive Linker

Another organosilane that was used for surface functionalization is the commercially available silane-PEG-maleimide indicated in Table 1. Maleimides form stable thioethers upon an alkylation reaction of their double bond with sulfhydryl groups (Figure 4.13).[15]
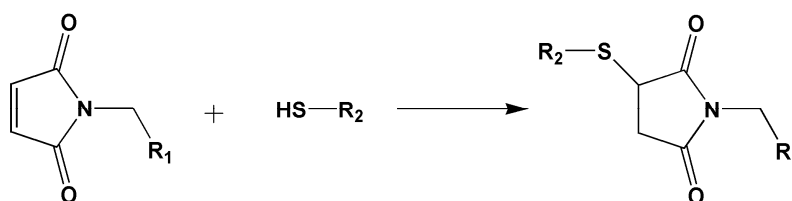
Figure 4.13: General alkylation reaction of maleimides with thiols resulting in a stable thioether linkage.

DRIFT spectra of UCLNP@SiO$_2$ compared to UCLNP@SiO$_2$-PEG-Mal (Figure 4.14) only give weak evidence of the incorporation of the silane in the silica shell. This was indicated by the signal around 2930 cm^{-1} that can be assigned to the hydrocarbons in the PEG chain. Yet the presence of maleimide groups could not be proven with IR spectroscopy.
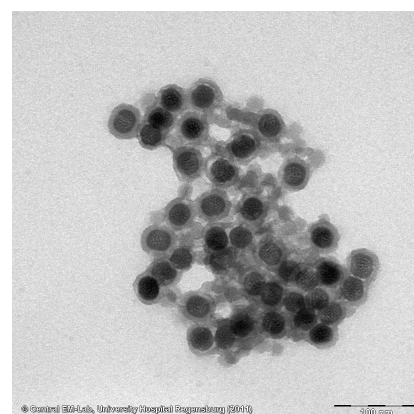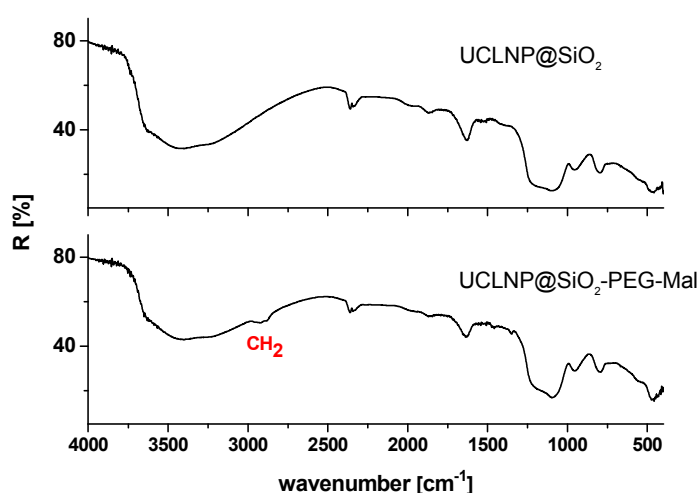
Figure 4.14: DRIFT spectra of UCLNP@SiO$_2$ compared to UCLNP@SiO$_2$-PEG-Mal display weak additional signals around 2930 cm^{-1} that can be assigned to the hydrocarbons in the polyethylene glycol chain. The TEM picture shows the particles functionalized with maleimide in 100,000x magnification, the scale bar is 100 nm.

The PEG tremendously reduced electrostatic repulsion between the particles. They did not flocculate in solution but the zeta potential of UCLNP@SiO$_2$-PEG-Mal was determined to be almost zero (-0.3 mV). The TEM picture in Figure 4.14 also hints at the particles being quite aggregated. The results of PCS (d = 179; PI = 0.25), in contrast, are in

good accordance with those of unmodified UCLNP@SiO$_2$ (see above) what might be due to a contribution of steric repulsion between the PEG chains.

For further verification of the presence of maleimide groups on the particle surface, HSA (human serum albumin) was labeled with FITC (fluorescein isothiocyanate) and reacted with UCLNP@SiO$_2$ and UCLNP@SiO$_2$-PEG-Mal, respectively. HSA bears one free thiol group on its cystein-34 residue which can form a stable thioether bond with maleimides. Contrary, the HSA-FITC conjugate should not bind to the plain silica surface for which reason this was used as a control experiment.
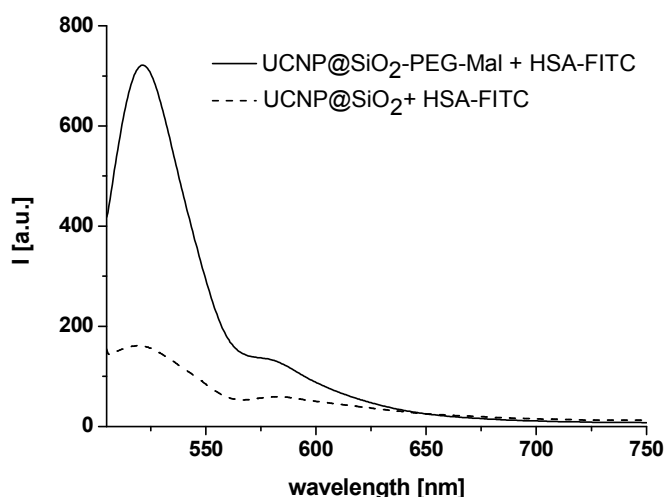
Figure 4.15: Fluorescence spectra of UCLNP@SiO$_2$ (dashed line) and UCLNP@SiO$_2$-PEG-Mal (full line) after reaction with a fluorophore labeled protein (HSA-FITC). The particles were purified by repeated centrifugation-washing cycles and redispersed in water. Spectra were collected upon excitation at 490 nm.

The reaction was allowed to proceed for 24 h before the particles were purified by repeated centrifugation-redispersion cycles. Fluorescence spectra upon excitation at 490 nm demonstrate the successful binding of HSA-FITC to UCLNP@SiO$_2$-PEG-Mal (Figure 4.15, full line), whereas the weaker fluorescence in the control experiment (Figure 4.15, dashed line) is due to some unspecific binding of the protein to the silica surface.[36] These particles and their application in a competitive heterogeneous immunoassay for the pesticide 2,4-D were further investigated by Raphaela Liebherr.[37]

Amino Functionalities

Amino groups are abundant in biology and hence popular targets for labeling procedures.[15] The common silane for introduction of amino groups on silica surfaces is APTES (Table 1). After synthesis and isolation from the microemulsion, UCLNP@SiO$_2$-NH$_2$ revealed a great tendency towards particle aggregation and precipitation. This is due to the opposite charges of the surface silanol (negatively charged) and surface amino groups (positively charged) at neutral pH. This disables electrostatic repulsion between the particles[38] and inverts the zeta potential from -21.3 mV (UCLNP@SiO$_2$) to 7.6 mV (UCLNP@SiO$_2$-NH$_2$). The PI was found to be 1.0, rendering PCS futile. Therefore, no TEM pictures were taken.

The presence of amino groups on the surface of UCLNP@SiO$_2$-NH$_2$ could not be definitely proven by DRIFT spectroscopy. The incorporation of APTES in the silica surface is only indicated by a weak signal of the propyl chain around 2930 cm^{-1} (Figure 4.16).
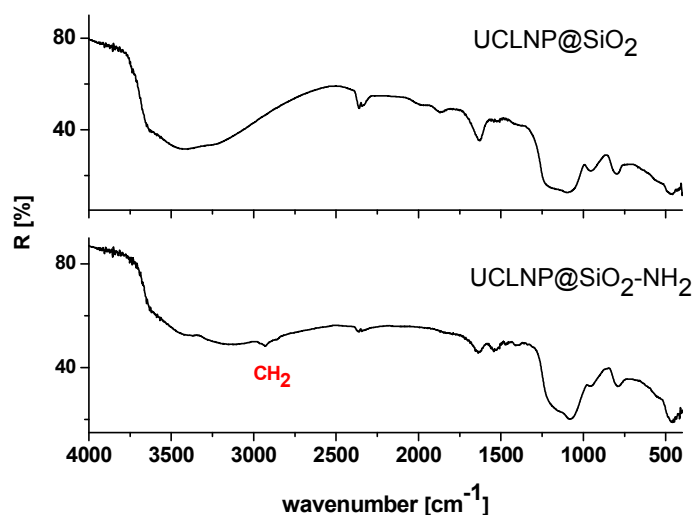
Figure 4.16: DRIFT spectra of UCLNP@SiO$_2$ compared to UCLNP@SiO$_2$-NH$_2$. The small IR signal around 2930 cm^{-1} can be assigned to the propyl chain of APTES that was used to functionalize the particle surface.

The chameleon label Py-1, a pyridinium analogon that reacts with primary amines, was used to get a qualitative verification of the presence of amino groups on the particles.[39] The fluorescent agent undergoes a remarkable color change from blue to red upon conjugation to primary amino groups, i.e. its absorbance maximum is shifted from 610 to 505 nm.[40] Upon

shaking and incubation at 37 °C the dark blue color of the chameleon label changed to red within a few minutes. A control experiment with non functionalized UCLNP@SiO$_2$ revealed no comparable color change. Figure 4.17 shows a photograph of the respective solutions in ethanol: UCLNP@SiO$_2$-NH$_2$ (colorless), Py-1 (dark blue), UCLNP@SiO$_2$-NH$_2$ + Py-1 (red), UCLNP@SiO$_2$ + Py-1 (green-blue; from left to right).

Figure 4.17 Color change of Py-1 from blue to red upon reaction with the amino functionalities on UCLNP@SiO$_2$-NH$_2$: UCLNP@SiO$_2$-NH$_2$, Py-1, UCLNP@SiO$_2$-NH$_2$ + Py-1 and the control experiment UCLNP@SiO$_2$ + Py-1 in ethanol (from left to right).

Thus, coating of UCLNPs with silica and modification of the surface of UCLNP@SiO$_2$ via reverse microemulsion is a simple and versatile method to generate labels for diverse biological applications. These posses the advantages of excitation in the NIR and variability regarding color and functionality. The latter is restricted since basic functionalities cause severe particle aggregation.

4.4. Encapsulation in Polystyrene

Other matrices for encapsulation of particles are polymers like polystyrene (PS). PSNPs or PS coated NPs are well dispersible in water and commonly considered as biocompatible. Usually encapsulation in polymers is achieved by radical polymerization of the respective monomers in an emulsion. For the entrapment of UCLNPs in PS an oil-in-water miniemulsion was applied comprising of water, SDS (sodium dodecyl sulfate), UCLNPs dispersed in cyclohexane and the styrene monomer. The UCLNPs, cyclohexane and the monomer form small droplets in the aqueous phase which are stabilized by the surfactant. Upon addition of a radical initiator, polymerization of the styrene occurs within the droplets

resulting in encapsulation of the NPs in the polymer. UCLNPs prepared via the thermal decomposition method were used since they are dispersible in the "oil" phase, an essential fact for efficient encapsulation. The TEM pictures in Figure 4.19 display the UCLNP@PS prepared via miniemulsion polymerization.
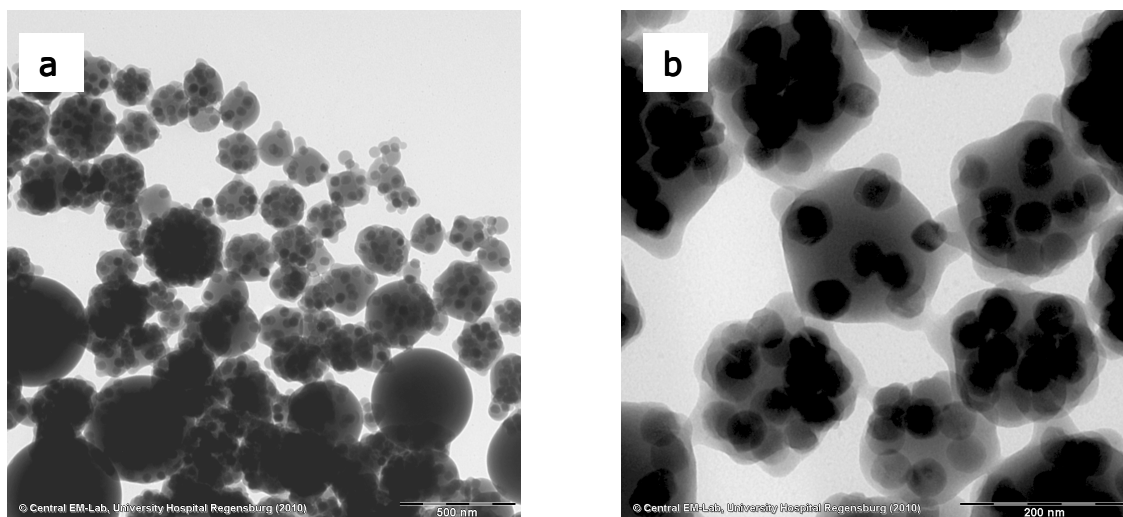
Figure 4.18: Typical TEM pictures of UCLNP@PS capsules formed by miniemulsion polymerization. Particles are depicted in 20,000x magnification with the scale bar being 500 nm (a) and 80,000x magnification with the length of the scale bar being 200 nm (b).

The procedure resulted almost exclusively in the inclusion of multiple particles with the size of the capsules ranging from 100 to 500 nm. Despite some quite large capsules, the particles did not settle from aqueous solution. PCS of an aqueous suspension revealed a mean hydrodynamic particle diameter of approximately 420 nm with a PI of 0.56 (see enclosed CD) which is due to the broad size distribution. In comparison, coating of UCLNPs with silica via reverse microemulsion resulted mainly in single coated particles or entrapment of a few NPs (see section 4.3.2). This is determined by the dimension of the droplets and micelles in which the particles are contained during polymerization. The size is 10 to 100 nm in the microemulsion for silica coating and 50 to 500 nm in the miniemulsion for coating with PS.[41] To a certain extend, the number of UCLNPs per nanosphere can be varied by changing the amount of nanophosphors which is added to the miniemulsion while keeping the other parameters constant. But the decreasing number of UCLNPs resulted

also in diminished uniformity of the sample. Figure 4.19 displays TEM pictures for three different amounts of particles that were added to the miniemulsion.
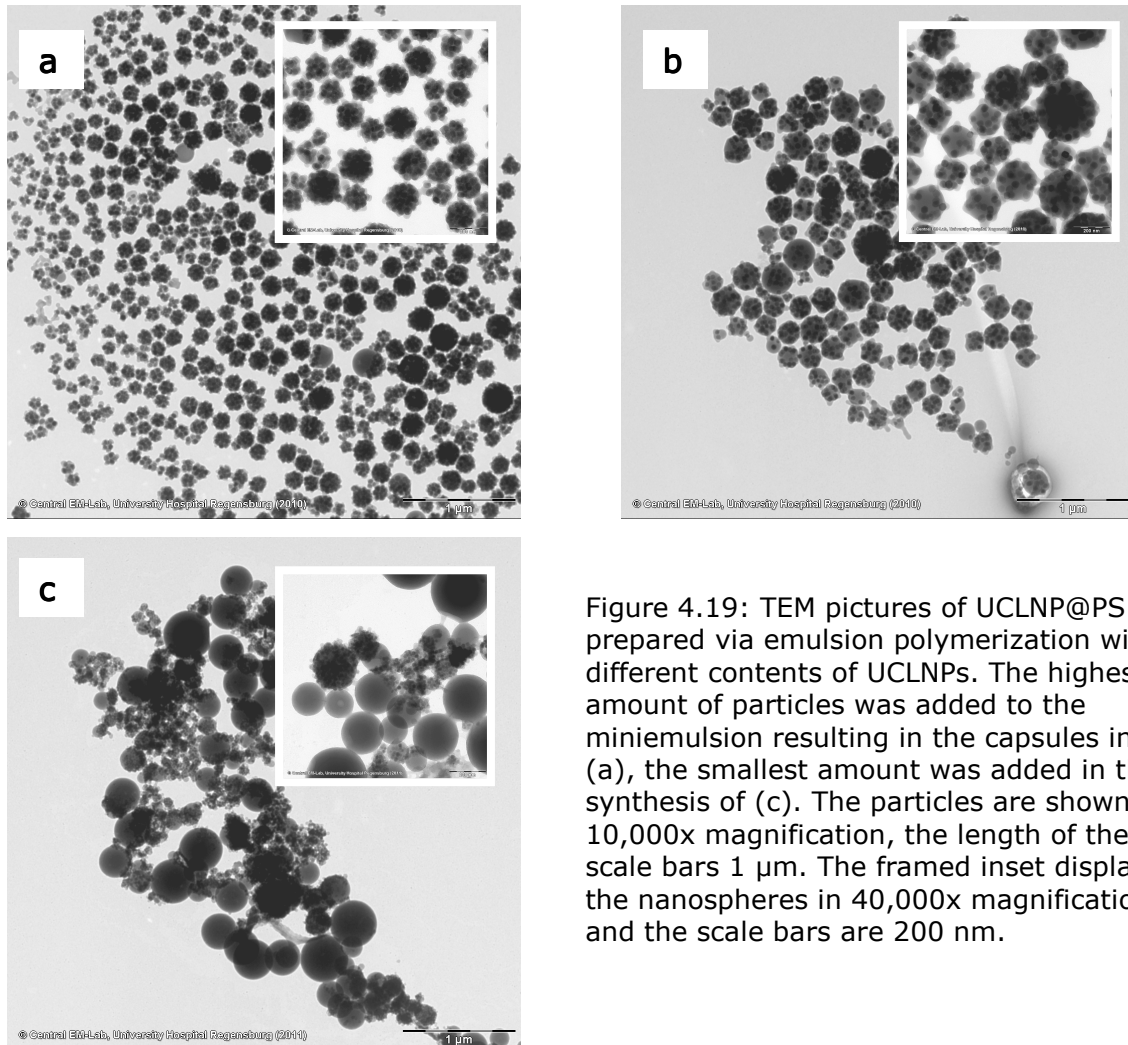
Figure 4.19: TEM pictures of UCLNP@PS prepared via emulsion polymerization with different contents of UCLNPs. The highest amount of particles was added to the miniemulsion resulting in the capsules in (a), the smallest amount was added in the synthesis of (c). The particles are shown in 10,000x magnification, the length of the scale bars 1 µm. The framed inset displays the nanospheres in 40,000x magnification and the scale bars are 200 nm.

The spheres in Figure 4.19a were synthesized in a reaction mixture containing the highest amount of UCLNPs. This resulted in PS capsules completely filled with UCLNPs with a size ranging from 50 to 500 nm. Figure 4.19b displays UCLNP@PS obtained from the reaction using half of the amount of nanophosphors. The average size increased, whereas the number of UCLNPs per capsule decreased. Further decrease of the amount of nanophosphors resulted in incomplete encapsulation and rather a formation of plain PSNPs (Figure 4.19c).

The miniemulsion process was intended for the co-encapsulation of magnetic NPs (MNPs) and UCLNPs in order to combine their properties. Like UCLNPs, iron oxide NPs can be prepared by thermal decomposition in an OA-OD mixture.[42] These particles also bear OA ligands on their surface and hence are applicable in polymer coating via emulsion polymerization. A mixture of UCLNPs and MNPs[43] was used in the synthesis described above resulting in PS capsules displayed in the TEM pictures in Figure 4.20.
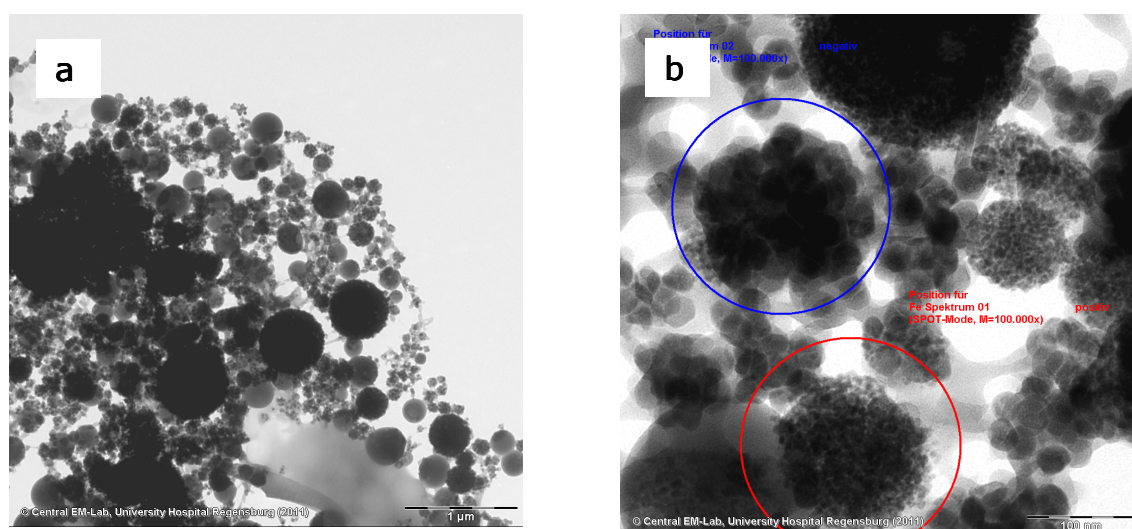
Figure 4.20: TEM pictures of PS capsules prepared via emulsion polymerization with a mixture of UCLNPs and MNPs in 10,000x magnification with a scale bar of 1 µm (a). A higher magnification (100,000x, the scale bar is 100 nm) reveals that the different kinds of NPs are separately encapsulated resulting in UCLNP@PS (blue circle) and MNP@PS (red circle) (b).

Generally, the nanospheres are less homogeneous and partly a PS matrix is rather formed than PS capsules (Figure 4.20a). UCLNPs and MNPs can be clearly distinguished since the nanophosphors are much larger than the iron oxide NPs. Notably the two types of NPs are encapsulated in a well separate form resulting in a mixture of UCLNP@PS and MNP@PS (Figure 4.20b) instead of the desired UCLNP/MNP@PS. That is most probable due to mutual magnetic attraction of the iron oxide NPs. This was further confirmed by EELS (electron energy loss spectroscopy). The respective spectra were compared to an iron reference spectrum, whereas only the investigated area in the red circle revealed the typical energy loss of iron around 712 eV (spectra see enclosed CD).

Hence, it was not possible to combine upconverting and magnetic properties in PS nanospheres by miniemulsion polymerization. Nevertheless, capsules of UCLNPs with different emission wavelength in varying ratios or UCLNP@PS with different organic fluorophores (subsequently embedded in the PS matrix)[44] are recommended for application in multiplexed encoding.[45]

4.5. References

1   Wang F, Wang J, Liu X (2010) *Direct Evidence of a Surface Quenching Effect on Size – Dependent Luminescence of Upconverting Nanoparticles.* Angew Chem Int Ed 49:1-6

2   Boyer J-C, Manseau M-P, Murray JI, van Veggel FCJM (2009) *Surface Modification of Upconverting NaYF$_4$ Nanoparticles with PEG-Phosphate Ligands for NIR (800 nm) Biolabeling within the Biological Window.* Langmuir 26:1157-1164

3   Wang Y, Tu L, Zhao J, Sun Y, Kong X, Zhang H (2009*) Upconversion Luminescence of β-NaYF$_4$: Yb^{3+}, Er^{3+}β-NaYF$_4$ Core/Shell Nanoparticles: Excitation Power Density and Surface Dependence.* J Phys Chem C 113:7164-7169

4   Vetrone F, Naccache R, Mahalingam V, Morgan CG, Capobianco JA (2009) *The Active Core/ Active Shell Approach: A Strategy to Enhance the Upconversion Luminescence in Lanthanide-Doped Nanoparticles.* Adv Funct Mater 19:2924-2929

5   Yi G-S, Chow G-M (2007) *Water-soluble NaYF$_4$:Yb,Er(Tm)/NaYF$_4$/Polymer Core/Shell/Shell Nanoparticles with Significant Enhancement of Upconversion Fluorescence.* Chem Mater 19:341-343

6   Guo H, Li Z, Quian H, Hu Y, Muhammad IN (2010) *Seed-mediated synthesis of NaYF$_4$:Yb,Er/NaGdF$_4$ nanocrystals with improved upconversion fluorescence and MR relaxivity.* Nanotechnology 21:125602

7   Liu B, Zeng HC (2005) *Symmetric and Asymmetric Ostwald Ripening in the Fabrication of Homogeneous Core-Shell Semiconductors.* Small 1:566-571

8   LaMer VK, Dinegar RH (1950) *Theorie, Production and Mechanism of Formation of Monodispersed Hydrosols.* J Am Chem Soc 72:4847-4854

9   Wang H-Q, Nann T (2011) *Upconverting Nanoparticles.* Springer Ser Fluoresc 7:115-132

10   Zhang Q, Song K, Zhao J, Kong X, Sun Y, Liu X, Zhang Y, Zeng Q, Zhang H (2009) *Hexanedioic acid mediated surface-ligand-exchange process for transferring NaYF$_4$:Yb/Er (or Yb/Tm) up-converting nanoparticles from hydrophobic to hydrophilic.* J Colloid Interf Sci 336:171-175

11   Xiong L, Yang T, Yang Y, Xu C, Li F (2010*) Long-term in vivo biodistribution imaging and toxicity of polyacrylic acid-coated upconversion nanophosphors.* Biomaterials 31:7078-7085

12   Johnson NJJ, Sangeetha NM, Boyer J-C, van Veggel CJM (2010) *Facile ligand-exchange with polyvinylpyrrolidone and subsequent silica coating of hydrophobic upconverting β-NaYF$_4$:Yb^{3+}/Er^{3+} nanoparticles.* Nanoscale 2:771-777

13   Chen Z, Chen H, Hu H, Yu M, Li F, Zhang Q, Zhou Z, Yi T, Huang C (2008) *Versatile Synthesis Strategy for Carboxylic Acid-functionalized Upconverting Naniphosphors as Biological Labels.* J Am Chem Soc 130:3023-3029

14   Lattuada M, Hatton TA (2007) *Functionalization of Monodisperse Magnetic Nanoparticles.* Langmuir 23:2158-2168

15   Hermanson GT (1996) *Bioconjugate Techniques.* Academic Press, New York

16   Sedlmeier A, Achatz DE, Wolfbeis OS (2012) *Erbium(III)-doped NaYF$_4$ nanoparticles for luminescent sensing of temperature.* Paper in preparation

17   Lu J, Liong M, Li Z, Zink JI, Tamanoi F (2010) *Biocompatibility, Biodistribution, and Drug-Delivery Efficiency of Mesoporous Silica Nanoparticles for Cancer Therapy in Animals.* Small 6:1794-1805

18   Jalil RA, Zhang Y (2008) *Biocompatibility of silica coated NaYF₄ upconversion fluorescent nanocrystals.* Biomaterials 29:4122-4128

19   Stöber W, Fink A, Bohn E (1968) *Controlled Growth of Monodisperse Silica Spheres in the Micron Size Range.* J Colloid Interface Sci 26:62-69

20   Tan W, Wang K, He X, Zhao XJ, Drake T, Wang L, Bagwe RP (2004) *Bionanotechnology Based on Silica Nanoparticles*. Med Res Rev 24:621-638

21   Alexander GB (1954) *The polymerization of monosilicic acid.* J Am Chem Soc 76:2094-2096

22   Liz-Marzán LM, Giersig M, Mulvaney P (1996) *Synthesis of Nanosized Gold-Silica Core-Shell Particles.* Langmuir 12:4329-4335

23   Kobayashi Y, Katakami H, Mine E, Nagao D, Konno M, Liz-Marzán LM (2005) *Silica coating of silver nanoparticles using a modified Stöber method.* J Colloid Interface Sci 283:392-396

24   Correa-Duarte MA, Giersig M, Liz-Marzán LM (1998) *Stabilization of CdSe semiconductor nanoparticles against photodegradation by a silica coating procedure.* Chem Phys Lett 286:497-501

25   Mader HS, Link M, Achatz DE, Uhlmann K, Li X, Wolfbeis OS (2010) *Surface-Modified Upconverting Microparticles and Nanoparticles for Use in Click Chemistries.* Chem Eur J 16:5416-5424

26   Mader HS (2010) *Surface Modification of Silica Particles and Upconverting Particles Using Click Chemistry.* Dissertation, University of Regensburg

27   Koole R, van Schooneveld MM, Hilhorst J, de Mello Donegá C, 't Hart DC, van Blaaderen A, Vanmaekelbergh D, Meijerink A (2008) *On the Incorporation Mechanism of Hydrophobic Quantum Dots in Silica Spheres by a Reverse Microemulsion Method.* Chem Mater 20:2503-2512

28   Bagwe RP, Yang C, Hilliard LR, Tan W (2004) *Optimization of Dye-Doped Silica Nanoparticles Prepared Using a Reverse Microemulsion Method.* Langmuir 20:8336-8342

29   Nwe K, Brechbiel MW (2009) *Growing Applications of "Click Chemistry" for Bioconjugation in Contemporary Biomedical Research.* Cancer Biother Radio 24:289-302

30   Moses JE, Moorhouse AD (2007) *The growing applications of click chemistry.* Chem Soc Rev 36:1249-1262

31   Wang Q, Chan TR, Hilgraf R, Fokin VV, Sharpless KB, Finn MG (2003) *Bioconjugation by Copper(I)-Catalyzed Azide-Alkyne [3+2] Cycloaddition.* J Am Chem Soc 125:3192-3193

32   Kolb HC, Finn MG, Sharpless KB (2001) *Click Chemistry: Diverse Chemical Function from a Few Good Reactions*. Angew Chem Int Ed 40:2004-2021

33   Rostovtsev VV, Green LG, Fokin VV, Sharpless KB (2002) *A Stepwise Huisgen Cycloaddtion Process: Copper (I) Catalyzed Regioselective "Ligation" of Azides and Terminal Alkynes.* Angew Chem Int Ed 41:2596-2599

34   Iler RK (1955) *The colloid chemistry of silica and silicates.* Cornell Univ Pr, Ithaca, NY

35   Finsy R (1994) *Particle sizing by quasi-elastic light scattering.* Adv Coll Interf Sci 52:79-143

36   Achatz DE (2008) *Fluorescent Silica Nanoparticles for Click Labeling of Proteins.* Diploma Thesis, University of Regensburg

37   Liebherr R (2011) *Thiol-Chemistry on Upconverting-Luminescent–Nanoparticles.* Master Thesis, University of Regensburg

38   Bagwe RP, Hilliard LR, Tan W (2006) *Surface Modification of Silica Nanoparticles to Reduce Aggregation and Nonspecific Binding.* Langmuir 22:4357-4362

39   Wetzl BK, Yarmoluk SM, Craig DB, Wolfbeis OS (2004) *Chameleon Labels for Staining and Quantifying Proteins.* Angew Chem Int Ed 43:5400-5402

40   Craig DB, Wetzl BK, Duerkop A, Wolfbeis OS (2005) *Determination of picomolar concentrations of proteins using novel amino reactive chameleon labels and capillary electrophoresis laser-induced fluorescence detection.* Electrophoresis 26:2208-2213

41   Schork J, Luo Y, Smulders W, Russum JP, Butte A, Fontenot K (2005) *Miniemulsion Polymerization.* Adv Polym Sci 175:129-255

42   Yu WW, Falkner JC, Yavuz CT, Colvin VL (2004) *Synthesis of monodisperse iron oxide nanocrystals by thermal decomposition of iron corboxylate salts.* Chem Comm:2306-2307

43   MNPs were kindly provided by Dr. Mark-Steven Steiner and prepared according to Lan Q, Liu C, Yang F, Liu S, Sun D (2007) *Synthesis of bilayer oleic acid-coated Fe₃O₄ nanoparticles and their application in pH-responsive Pickering emulsions.* J Coll Interf Sci 310:260-269

44   Behnke T, Würth C, Hoffmann K, Hübner M, Panne U, Resch-Genger U (2011) *Encapsulation of Hydrophobic Dyes in Polystyrene Micro- and Nanoparticles via Swelling Procedures.* J Fluoresc 21:937-944

45   Gorris HH, Ali R, Saleh SM, Wolfbeis OS (2011) *Tuning the Dual Emission of Photon-Upconverting Nanoparticles for Ratiometric Multiplexed Encoding.* Adv Mater 23:1652-1655

5. Multicolor Upconverting Luminescent Nanoparticles for Ratiometric Encoding

Multicolor imaging denotes an application of fluorescence microscopy which is intended to study biological interactions between different organelles, proteins, enzymes, cells etc. The different parts of interest need to be tagged with diverse colored labels in order to distinguish them. Usually combinations of fluorescein, rhodamine and cyanine dyes[1] or fluorescent proteins[2] are applied. These feature drawbacks like broad emission bands and the need of different excitation wavelengths that limit spectral separation and simultaneous imaging (see section 2.2.2).

The beneficial optical properties of UCLNPs render them ideal candidates for multicolor biological imaging and labeling: excitation with NIR light of a single wavelength suffices to excite particles that exhibit diverse colored emissions and the emission bands are well separated (compare section 2.2.3). In this work, UCLNPs were synthesized that emit five different colors. This was achieved by varying the doping ratio of the activator ions. The particles can clearly be distinguished by applying a ratiometric RGB read-out after one emission scan using single wavelength excitation at 980 nm. Further, these particles were coated with silica to render them water dispersible and to increase their biocompatibility. NRK (normal rat kidney) cells were tagged with the multicolor $UCLNP@SiO_2$ and images of the cells were taken by laser scanning microscopy.

5.1. Multicolor Upconverting Luminescent Nanoparticles

Different types of lanthanide doped $NaYF_4$ nanophosphors were synthesized via thermal decomposition as it was discussed in detail in chapter 3.2. $NaYF_4$:Yb,Er (20/2) emit mainly green light, while the maximum of the emission of $NaYF_4$:Yb,Tm (20/0.5) peaks in the blue spectral region. Hence, co-doping of Er^{3+} and Tm^{3+} should result in

turquoise luminescence. Er^{3+} activator ions generally exhibit brighter emission than Tm^{3+} ions (see section 3.1 and 3.2). Therefore, the optimized doping ratio of Tm^{3+} was kept constant (Yb^{3+}/Tm^{3+} = 20/0.5) and the percentage of Er^{3+} was gradually decreased from 1.5 to 0.01% to reduce its green emission and to determine the appropriate doping ratio for UCLNPs that nearly equally emit blue and green, hence turquoise light.
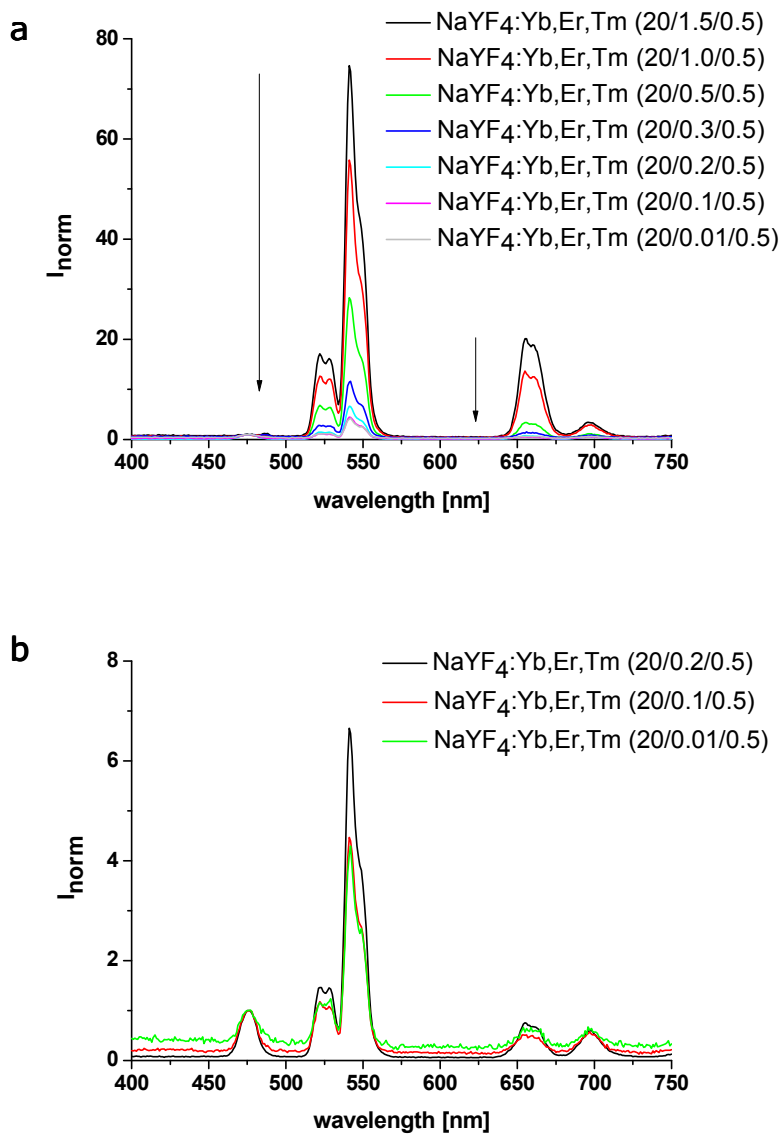
Figure 5.1: Upconversion luminescence spectra of $NaYF_4$:Yb,Er,Tm (20/1.5-0.01/0.5) normalized to the blue emission of Tm^{3+} at 475 nm (a). An enlarged spectrum of the three lowest Er^{3+} percentages reveals that the green and red emission peaks remain almost unchanged below 0.1% (b).

Figure 5.1a displays the spectra of $NaYF_4$:Yb,Er,Tm (20/1.5-0.01/0.5) normalized to the blue emission of Tm^{3+} at 475 nm. The green (520 and 540 nm) and the red emissions (655 nm) of Er^{3+} diminish with decreasing content. Figure 5.1b depicts the three lowest Er^{3+} ratios. The emission

remains quite constant below 0.1% of Er^{3+} while the overall brightness starts to decline. Hence, particles of the type $NaYF_4$:Yb,Er,Tm (20/0.1/0.5) were used in the following.

Further, orange and red appearing UCLNPs were prepared via thermal decomposition following an approach by Chen et al.[3] They utilzed tridoping of $NaYF_4$:Yb,Ho with Ce^{3+} to suppress the green emission of Ho^{3+} (see section 2.1.2) by cross-relaxation processes between these two ions. $NaYF_4$:Yb,Ho,Ce (20/2/15 or 30) were also synthesized via thermal decomposition. Figure 5.2 displays the upconversion luminescence spectra of orange emitting $NaYF_4$:Yb,Ho,Ce (20/2/15) and red emitting $NaYF_4$:Yb,Ho,Ce (20/2/30) normalized to the red emission peak of Ho^{3+} at 645 nm and a TEM picture of these tridoped UCLNPs.
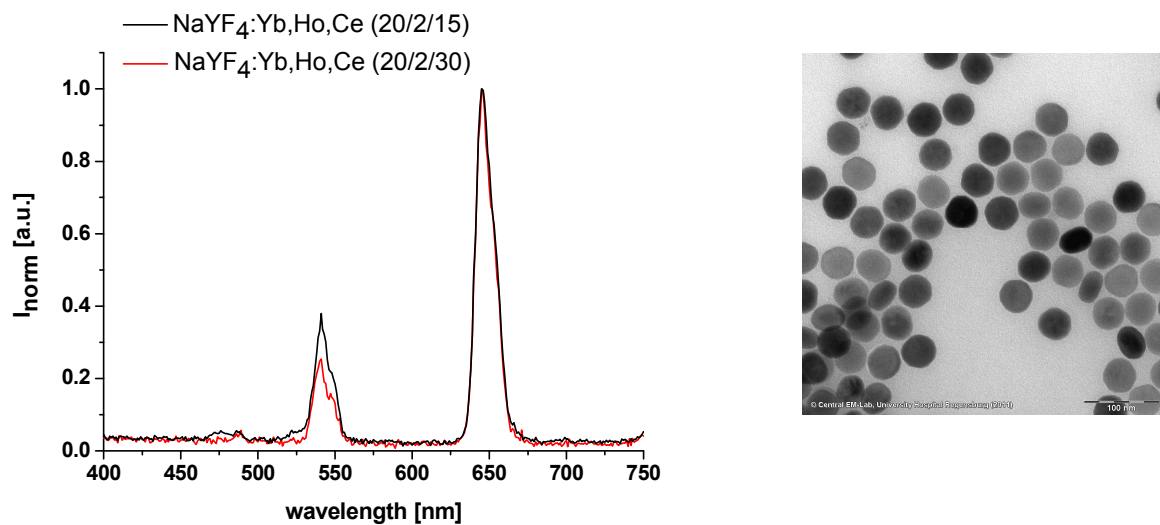
Figure 5.2: Upconversion luminescence spectra of $NaYF_4$:Yb,Ho,Ce (20/2/15 or 30) normalized to the red emission of Ho^{3+} at 650 nm. Next to the graphs a TEM picture of tridoped $NaYF_4$ is depicted revealing a mean particle diameter of 45 nm (100,000x magnification, the length of the scale bar is 100 nm).

Hence, five different types of UCLNPs were prepared that exhibit diverse visible emissions. The next step was to render these particles water dispersible and biocompatible. Coating with silica was preferably applied for this purpose instead of LE with CA. The latter is indeed capable of stabilizing the UCLNPs in aqueous solution. Yet the CA ligands might be detached from the surface or undesired exchange reactions might take

place in biological media (see chapter 4.2). Silica coating was carried out
by reverse microemulsion as it was described in detail in section 4.3.2.
Figure 5.3 displays the combined spectra of the multicolored UCLNP@SiO$_2$
in water and a picture of the emissions upon excitation at 980 nm with a
CW diode laser taken by a conventional camera.
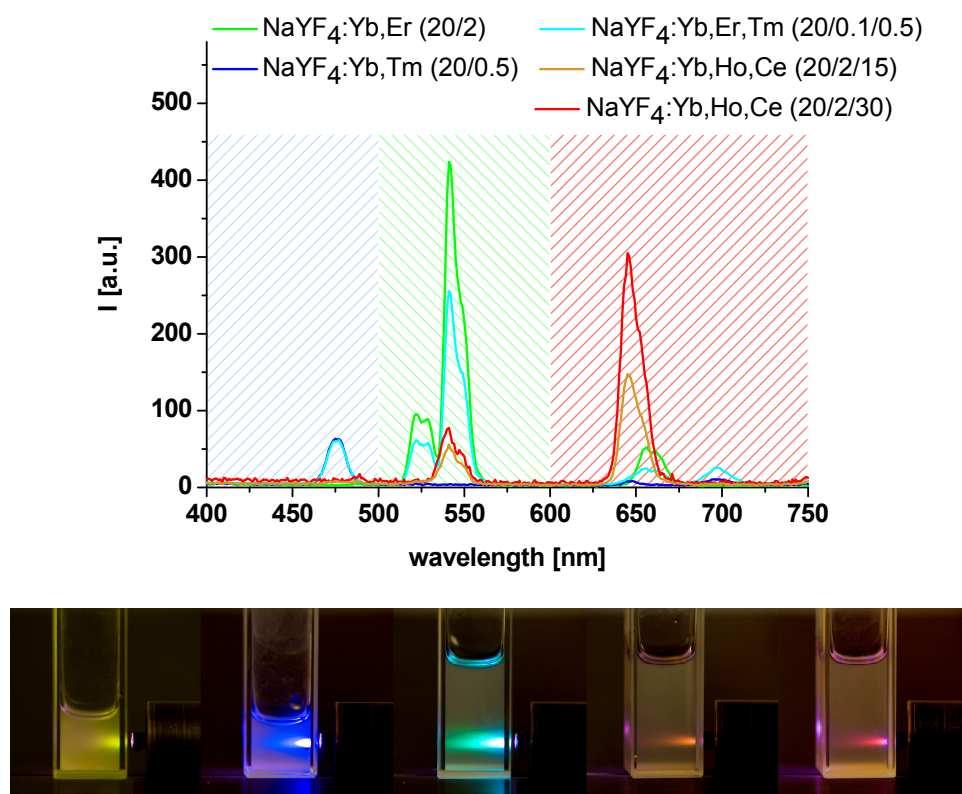
Figure 5.3: Upconversion luminescent spectra of multicolor UCLNP@SiO$_2$ in water
(0.1wt%). The spectrum of NaYF$_4$:Yb,Er (20/2) was divided by a factor of 25. The other
spectra display the actual intensity ratios without normalization. The peaks are well
separated in three main regions: 400 to 500 (blue), 500 to 600 (green), 600 to 750 nm
(red). Below the graphs a picture of the emission of the respective particles upon
excitation at 980 nm is illustrated: NaYF$_4$:Yb,Er (20/2), NaYF$_4$:Yb,Tm (20/0.5),
NaYF$_4$:Yb,Er,Tm (20/0.1/0.5), NaYF$_4$:Yb,Ho,Ce (20/2/15), NaYF$_4$:Yb,Ho,Ce (20/2/30)
from left to right.

The emission intensities are not normalized. Except the emission of
NaYF$_4$:Yb,Er (20/2) the spectra display the actual intensity ratios. Since
NaYF$_4$:Yb,Er (20/2) are much brighter than the other UCLNPs, their
spectrum was divided by a factor of 25. The emission peaks are well
separated in three main areas spanning 400 to 500 (blue), 500 to 600
(green) and 600 to 750 nm (red). Hence, the particles can be clearly

distinguished by the ratios from the integrals of the respective spectral regions allowing for a ratiometric RGB (red-green-blue) read-out. Here the principle is demonstrated only for a selection of five types of UCLNPs whose emitted light can be clearly identified by the naked eye. However, the possibility to tune the signal intensity ratio of the UCLNPs gradually by varying the dopant concentration allows for a huge number of different RGB codes that are ideally suited for multiplexed encoding.

UCLNP@SiO$_2$	Notation	$I_{norm}(R)$	$I_{norm}(G)$	$I_{norm}(B)$
NaYF$_4$:Yb,Er (20/2)	NP_1	0.13	1.00	-
NaYF$_4$:Yb,Tm (20/0.5)	NP_2	0.18	-	1.00
NaYF$_4$:Yb,Er,Tm (20/0.1/0.5)	NP_3	0.20	1.00	0.15
NaYF$_4$:Yb,Ho,Ce (20/2/15)	NP_4	1.00	0.36	-
NaYF$_4$:Yb,Ho,Ce (20/2/30)	NP_5	1.00	0.23	-

Table 2: The simplified notation and the corresponding RGB ratios for the multicolor UCLNP@SiO$_2$ are summarized in the table. The ratios were obtained from the integrals of the baseline corrected spectra from 600 to 750 nm (red, R), 500 to 600 nm (green, G) and 400 to 500 nm (blue, B) which were standardized to the area containing the respective emission maximum.

In the following, the multicolor silica coated UCLNPs are denoted according to Table 2 for simplification. The RGB ratios of the particles were derived from the integrals of the graphs in the particular spectral region (see above; baseline corrected) and were standardized to the region with the maximal emission, respectively.

5.2. Biocompatibility

It was intended to tag NRK cells with the diverse types of multicolor UCLNPs. An AlamarBlue® cell viability assay was performed in order to get an indication for the concentration of UCLNP@SiO$_2$ that can be used for incubation with NRK cells. This test is based on an oxidation-reduction indicator that fluoresces and changes its color upon reduction of the medium during cell growth (for a detailed protocol see Experimental Part). Confluently grown NRK cells were incubated with different amounts of

UCLNP@SiO$_2$ at 37 °C in a 96-well microtiter plate (MTP) for 24 h. Control experiments without NPs (maximal growth) and with Triton (minimal growth) were performed. The results of the assay are displayed in Figure 5.4a.

a

% maximum growth (y-axis)

Bars: without NPs, 0.5 µg/mL, 1.0 µg/mL, 5.0 µg/mL, 10.0 µg/mL, 50.0 µg/mL, 100.0 µg/mL, 200.0 µg/mL, Triton
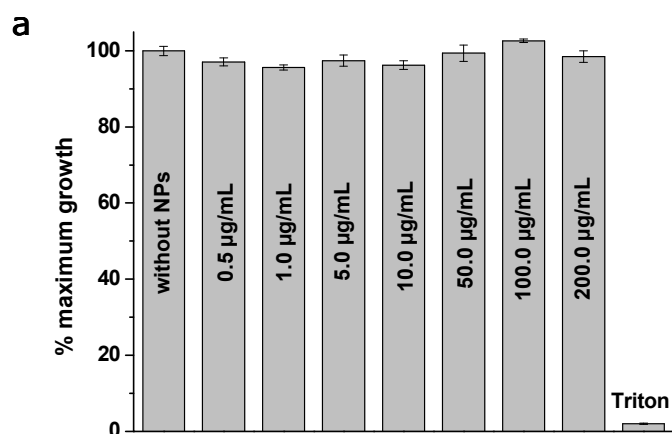
Figure 5.4: Results of the AlamarBlue® cell viability assay of NRK cells incubated with different amounts of UCLNP@SiO$_2$ at 37 °C for 24 h (a). Standard deviations were obtained from six wells representing six parallel experiments. Micrographs from NRK cells treated with 5.0 (left), 50.0 (middle) and 200.0 µg/mL (right) revealed a morphological abnormality for the highest NP concentration (b).

b

5.0 µg/mL   50.0 µg/mL   200.0 µg/mL
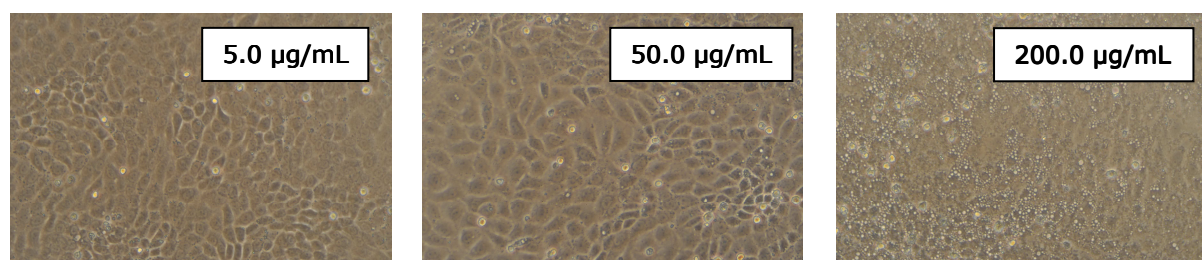
Particle concentrations ranging between 0.5 µg/mL and 200.0 µg/mL revealed no cytotoxicity in the assay or hindrance of cell proliferation. However, light microscopy revealed a morphological abnormality for cells treated with the highest concentration of UCLNP@SiO$_2$ (Figure 5.4b, right). These results are in good agreement with report on findings about cytotoxicity of pure silica NPs[4] and demonstrate that coating with silica is convenient if water dispersibility and biocompatibility is desired.

5.3. Fluorescence Imaging

Confluent NRK cell monolayers were incubated with different amounts of
NP_1-5 (1.0 to 100.0 µg/mL). The cells were thoroughly washed to
remove excess NPs and fixed with 4% (v/v) paraformaldehyde. Images of
the cells were taken by laser scanning microscopy. Due to the lack of an
instrument with a NIR laser excitation source in CW mode, measurements
were performed on a Zeiss LSM 710 equipped with a short-pulsed laser
that is conventionally used for TPLSM. Surprisingly the particle uptake was
quite poor even for the highest applied particle concentration. Figure 5.5
displays micrographs[5] of cells treated with 0.1 mg/mL UCLNP@SiO$_2$
solutions.
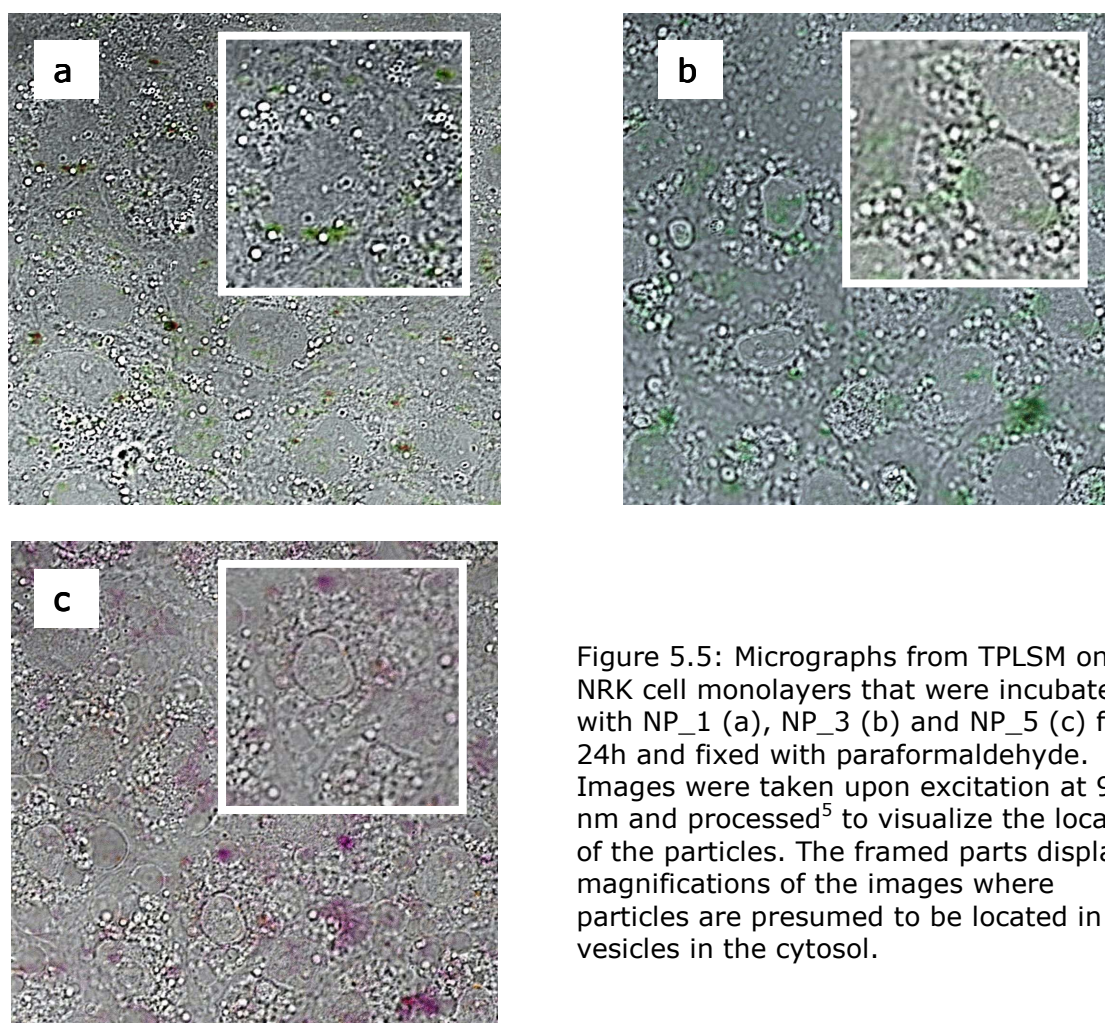
Figure 5.5: Micrographs from TPLSM on
NRK cell monolayers that were incubated
with NP_1 (a), NP_3 (b) and NP_5 (c) for
24h and fixed with paraformaldehyde.
Images were taken upon excitation at 980
nm and processed[5] to visualize the location
of the particles. The framed parts display
magnifications of the images where
particles are presumed to be located in
vesicles in the cytosol.

Generally, many factors like size, charge and surface characteristics but also cell type and microenvironment impact the pathway and efficiency of the uptake.[6] Reports on differently sized (30 to 280 nm) and shaped silica NPs revealed the formation of non-uniform aggregates in the perinuclear region after non-specific cellular uptake.[7] This is due to encapsulation in vesicular or cytosolic compartments. Due to their size these particles did not penetrate the nucleus.[8] A similar behavior was expected for the multicolored, silica coated UCLNPs since they posses an identical surface and feature a similar size. Unfortunately, it could not be ascertained whether the few particles that could be imaged are really incorporated inside the cells. At least some of them seem to be arranged in vesicles somewhere around the nucleus (see magnifications in Figure 5.5). Notably, the RGB ratios of NP_1-5 calculated from the TPLSM images (Table 3)[9] are not consistent with the RGB ratios obtained from the integration of the upconversion emission spectra (Figure 5.3, Table 2).

UCLNP@SiO_2	Notation	$I_{norm}(R)$	$I_{norm}(G)$	$I_{norm}(B)$
$NaYF_4$:Yb,Er (20/2)	NP_1	0.85	1.00	-
$NaYF_4$:Yb,Tm (20/0.5)	NP_2	0.78	1.11	1.00
$NaYF_4$:Yb,Er,Tm (20/0.1/0.5)	NP_3	0.96	1.00	0.25
$NaYF_4$:Yb,Ho,Ce (20/2/15)	NP_4	1.00	0.65	-
$NaYF_4$:Yb,Ho,Ce (20/2/30)	NP_5	1.00	0.65	-

Table 3: RGB ratios obtained from the TPSLM images as described in Ref. 6.

First, a kind of „red shift" can be observed. Especially for NP_1-3 the intensity in the region from 600 to 750 nm is enhanced. This is probably due to the different detection systems. Upconversion luminescence spectra (Figure 5.3) were collected using a fluorometer without correction, i.e. the photomultiplier (PMT) is not of equal efficiency at all wavelengths. Usually it is less sensitive to red light. The PMT detector of the microscope features a linear efficiency across the VIS spectrum. Further variations from the RGB ratios in Table 2 might be due to the different kinds of excitation sources. Despite the same excitation wavelength (980 nm),

emission was induced either by using a CW laser diode to collect the luminescence spectra or a short-pulsed laser for microscopy which is actually intended for TPE. Conceivably, the transitions upon continuous irradiation (Figure 2.2) might be different from those favored by short-pulsed NIR light.

In summary, the multicolor UCLNPs described in this chapter constitute a promising material for multiplex encoding applications. Particles with numerous RGB-codes can be synthesized by selective damping of the narrow emission peaks (Figure 5.1 and Figure 5.2). New equipment like a CCD camera with NIR LED excitation in accordance to a recently published approach towards "Photographing Oxygen Distribution"[10] can enable new applications. The silica coated NPs exhibit good biocompatibility. Yet there is a need to optimize the protocol for incorporation of the NPs in cells to achieve an improved loading. Cells tagged with multicolor UCLNPs are good candidates for *in vivo* cell tracking. Further, the spectral characteristics of the UCLNPs under short-pulsed NIR excitation have to be investigated or a microscope with CW NIR laser excitation is desirable.

5.4. References

1   Kobayashi H, Hama Y, Koyama Y, Barrett T, Regino CAS, Urano Y, Choyke PL (2007) *Simultaneous Multicolor Imaging of Five Different Lymphatic Basins Using Quantum Dots.* Nano Lett 7:1711-1716

2   Hoffmann RM (2005) *The Multiple Uses of Fluorescent Proteins to Visualize Cancer In Vivo.* Nat Rev Cancer 5:796-806

3   Chen G, Liu H, Somesfalean G, Liang H, Zhang Z (2009) *Upconversion emission tuning from green to red in Yb^{3+}/Ho^{3+}-codoped $NaYF_4$ nanocrystals by tridoping with Ce^{3+} ions.* Nanotechnology 20:385704

4   Jin Y, Lohstreter S, Pierce DT, Parisien J, Wu M, Hall C, Zhao JX (2008) *Silica Nanoparticles with Continuously Tunable Sizes: Synthesis and Size Effects on Cellular Contrast Imaging.* Chem Mater 20: 4411-4419

5   The cells treated with NP_1-5 were investigated by TPLSM under excitation with a 980 nm fs-pulsed raster scanning laser beam (5 mW). Images of the VIS emission (400 to 750 nm) of a focused area were collected within spectral windows of 10 nm each. Stacked images of these spectral regions were obtained which were processed with freely available software for microscopy from MacBiophotonics (ImageJ; www.macbiophotonics.ca). The stack was

converted to single images. These were combined (addition of intensities) for the red, green and blue spectral regions which are defined in the main text. Thus three images for each particle type were obtained. The micrographs in Figure 5.5 were generated by an overlay of these three pictures with a phase contrast micrograph using Jasc Paint Shop Pro 7.

6   Unfried K, Albrecht C, Klotz L-O, von Mikecz A, Grether-Beck S, Schins RPF (2007) *Cellular response to nanoparticles: Target structures and mechanism.* Nanotoxicology 1:52-71

7   Huang X, Teng X, Chen D, Tang F, He J (2010) *The effect of the shape of mesoporous silica nanoparticles on cellular uptake and cell function.* Biomaterials 31:438-448

8   Lu F, Wu S-H, Hung Y, Mou C-Y (2009) *Size Effect on Cell Uptake in Well-Suspended, Uniform Mesoporous Silica Nanoparticles.* Small 5:1408-1413

9   The stacks from TPLSM were subjected to the same process as in Ref 5. The three images (R, G, B) that were obtained for each particle type were stacked. Obvious particle aggregates were selected and measured using the respective ImageJ tools. The obtained intensities were standardized to the intensity of the image (R, G or B) for which the maximum was expected according to Table 2.

10   Wang X, Meier RJ, Link M, Wolfbeis OS (2010) *Photographing Oxygen Distribution.* Angew Chem Int Ed 49:4907-4909

6. Luminescent Sensing of Oxygen Using a Quenchable Probe and Upconverting Nanoparticles

It was already noted in section 2.3.4 that UCLNPs, despite their beneficial optical properties, have been rarely used for purposes of optical chemical sensing.[1,2,3] So far, almost all existing schemes for sensing oxygen are based on the (dynamic) quenching of the luminescence of appropriate probes like Pt(II) and Pd(II) porphyrins and metal-ligand complexes of Ru(III) and Ir(III) by oxygen. However, the emission of UCLNPs is not at all quenched by oxygen and thus cannot be used for direct sensing. On the other hand, the probes known to date cannot be photoexcited by NIR light nor do they give the effect of upconversion. In the sensing scheme presented herein, UCLNPs are used as kind of nanolamps whose visible emission acts as the light source that is causing photoexcitation of an iridium(III) complex. The fluorescence of this complex, in turn, is dynamically quenched by oxygen.[4]

6.1. Selection of Material and Preparation of the Sensor Film

$NaYF_4$:Yb,Tm prepared by the co-precipitation method followed by thermal treatment (see chapter 3.1) was chosen as the material for the UCNLPs acting as nanolamps. These UCLNPs, on excitation with a 980 nm diode laser, give a dual emission with bands in the blue and red part of the spectrum. Graph A in Figure 6.1 displays the spectrum collected from particles immobilized in a matrix of ethyl cellulose. It is noteworthy that, contrary to the spectra collected from particles in solution (see Figure 3.3), the blue peak at 450 nm (Figure 2.2) can be observed. It was perceived that the emission of the particles may serve as the excitation light source for a probe for oxygen, which by itself cannot be photoexcited with continuous NIR laser light. The cyclometalated iridium(III) coumarin complex [Ir(C_S)_2(acac)] C_S = 3-(benzothiazol-2-yl)-7-diethylamino-1-benzopyran-2-on,[5] was chosen as the quenchable probe for oxygen

because its absorbance has a maximum at 468 nm (graph B in Figure 6.1) that strongly overlaps the two shortwave emissions (at 450 and 475 nm) of the UCLNPs. Its green to yellow luminescence (graph C in Figure 6.1) has a maximum at 568 nm, is strongly quenched by oxygen, and has only minimal overlap with the red emission of the UCLNPs at wavelengths above 630 nm. As a result, band C can be easily separated from these using an interference filter.
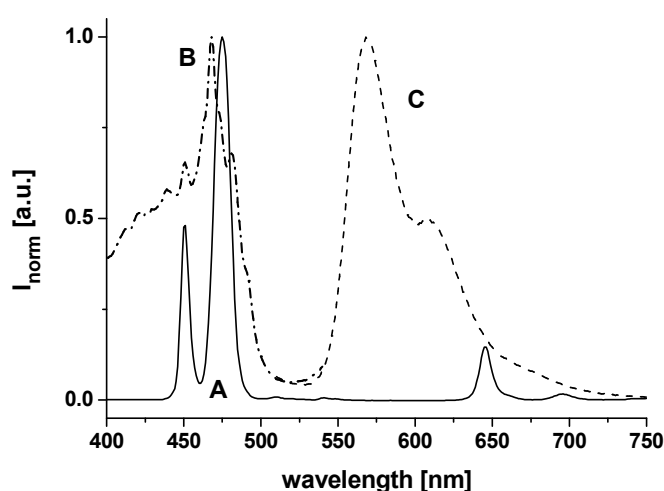
Figure 6.1: Normalized excitation and emission spectra showing the spectral overlap of the emission of the $NaYF_4$:Yb,Tm NPs with the absorption of the oxygen probe $[Ir(C_S)_2(acac)]$. A) Emission spectrum of the nanoparticles in an ethyl cellulose matrix after photoexcitation at 980 nm with a CW diode laser; B) absorbance, and C) emission spectrum of $[Ir(C_S)_2(acac)]$.

To obtain a sensor layer for continuous sensing of oxygen, the UCLNPs and the oxygen probe were incorporated in a thin layer of EC (ethyl cellulose) as described in the Experimental Part. EC is easily penetrated by oxygen,[6] the permeability coefficient P being $11 \cdot 10^{13}$ cm^2 $(s\ Pa)^{-1}$. The sensor film was prepared by first dissolving the iridium(III) probe, the UCLNPs and EC in THF, then spreading this mixture onto a glass plate, and then leaving the solvent to evaporate.

6.2. Upconversion Based Luminescent Sensing of Oxygen

The yellow and slightly opaque sensor film (with a thickness of 1.8 to 2.0 µm) was placed in a flow-through cell in order to acquire luminescence spectra and to study quenching by molecular oxygen by passing gases

with varying fractions of oxygen over it. The complete emission spectrum (from 400 to 750 nm) of the sensor film after excitation at 980 nm with a CW diode laser (3W) in an atmosphere of argon is shown in Figure 6.2. Compared to graph A in Figure 6.1, the intensities of the emission bands of the UCLNPs that peak at 450 and 475 nm (bands A and B in Figure 6.2a) are significantly reduced in intensity, because they are absorbed (screened off) by the iridium(III) complex.
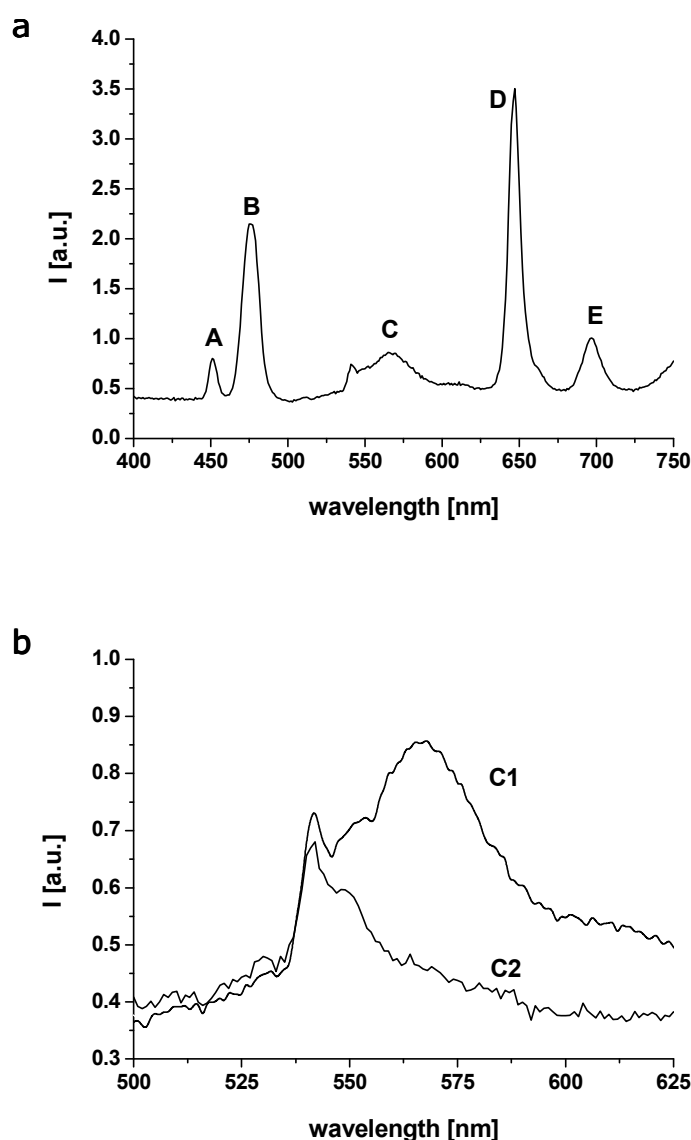
Figure 6.2: Visible spectra of an ethyl cellulose sensor film containing the NaYF$_4$:Yb,Tm UCLNPs and the oxygen probe [Ir(C$_S$)$_2$(acac)] following photoexcitation at 980 nm. (a) Compared to Figure 6.1, the blue emission bands of the UCLNPs (A, B) are screened off by the oxygen probe. The intensities of their red peaks (D, E) are unaffected. The iridium(III) complex is photoexcited by the UCLNPs (C). (b) The decrease in size of the peak at 568 nm (A1) in argon, A2) after exposure to argon containing 20% oxygen) clearly indicates the quenching of [Ir(C$_S$)$_2$(acac)] by oxygen. T = 24 °C; atmospheric pressure.

The intensities of the red bands (bands D and E in Figure 6.2a) of the UCLNPs and their ratio remain unaffected, but their relative contributions to the overall emission are of course much larger now. The appearance of

the luminescence of the probe [Ir(C_S)$_2$(acac)] (band C in Figure 6.2a) proves that the probe is photoexcited by the emission of the NPs even though the luminescence quantum yields of UCLNPs are rather small,[7] typically less than 1%. Figure 6.2b shows a magnification of the emission spectra of the sensor film between 500 and 625 nm in an atmosphere of argon and in a gas that contains 80% nitrogen and 20% oxygen. The emission of the iridium complex with its maximum at 568 nm (bands C1 and C2) is quenched by oxygen. A more careful look at band C1 and C2 reveals that there is a small contribution (a shoulder on the left side of the band) that originates from the UCLNPs, probably a result of the presence of traces of Er^{3+} ions.

This effect is interpreted to be a result of the UCLNPs acting as nanolamps inside the sensor film, with their blue emission being absorbed (and converted into green-yellow luminescence) by the iridium complex. Fluorescence resonance energy transfer[8] (as invoked in cases where upconverting particles were used as labels in bioassays)[9,10,11] is unlikely to occur to a substantial extent given the average distance between the two emitters which is far above the Förster distance of typically 7 to 10 nm. This fact has also been pointed out by Morgan et al.[12] The respective Stern-Volmer plots[13] (Figure 6.3; average of 5 independent measurements for each oxygen concentration) reveal three interesting findings: (i) The Stern-Volmer plot resulting from direct excitation of the iridium probe is highly linear, whereas that of the indirectly excited probe is strongly curved; (ii) the slopes of the Stern-Volmer plots differ strongly depending on whether the sensor film is excited conventionally at 475 nm (using a xenon lamp; see plot I), or whether excitation is performed at 980 nm by the NPs (plot II); and (iii) the precision (expressed as the standard deviation; Figure 6.3) is much higher for conventional excitation. This shall be discussed and interpreted below.
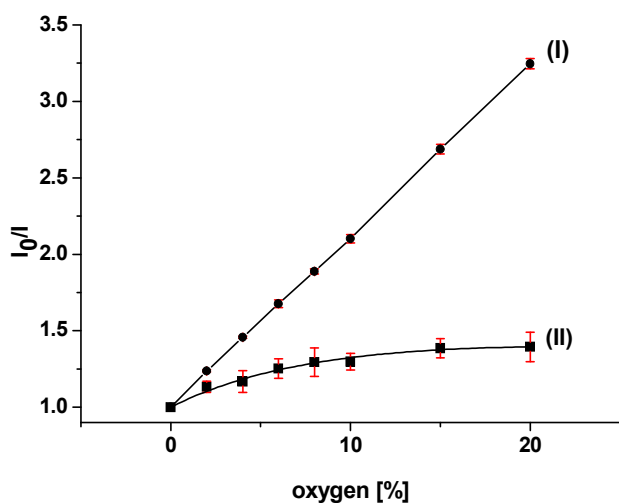
Figure 6.3: Stern-Volmer plots of the quenching by oxygen of the emission of an ethyl cellulose sensor film containing the oxygen probe $[Ir(C_S)_2(acac)]$ and the $NaYF_4$:Yb,Tm UCLNPs. Plot (I) was obtained after direct excitation of the iridium probe at 475 nm by using a xenon lamp, and plot (II) was obtained after diode laser excitation of the UCLNPs at 980 nm and monitoring the green emission of the iridium probe

Both the difference in the slope and the shape of the plots can be interpreted in terms of different microenvironments of the iridium-based probes for oxygen. Illumination at 475 nm will photoexcite all of the probe molecules dissolved in ethyl cellulose. The overwhelming majority of them are freely accessible to oxygen. Dynamic quenching therefore will be highly efficient, and the respective Stern-Volmer plot (plot I in Figure 6.3) is linear ($R^2 = 1$). The quenching constant (K_{sv}) was calculated to be $0.112\%^{-1}$. If, however, the sensor film is illuminated with the 980 nm diode laser, photoexcitation will occur via the luminescence of the UCLNPs, which act as nanolamps inside the sensor film. As a result, probe molecules located close to the UCLNP and to a lesser extend in the bulk of the film will be photoexcited. Those located close to the nanoparticles will not be freely accessible to oxygen, but rather be shielded on one side by the NPs from being quenched. The situation of dynamic quenching of the luminescence of fluorophores in two kinds of (micro)environments can be fit with the so-called two-site-model,[14]

$$\frac{I}{I_0} = \frac{f_1}{1 + K_1 \cdot [O_2]} + \frac{f_2}{1 + K_2 \cdot [O_2]}$$ (Equation 1)

where f_1 and f_2 are the fractions of the two processes contributing to the total emission ($f_1 + f_2$ being 1), and K_1 and K_2 being the Stern-Volmer

constants for each component, respectively. One may differentiate collectively between two types of molecules: iridium(III) probes quite close to the particles and less accessible by oxygen, and those somewhat farther away but still not as amenable as the probe molecules in the bulk sensor film. The two-site model (Equation 1) gives quenching constants of 0.101 and $0.0037\%^{-1}$ for K_1 and K_2, with weighting factors f_1 and f_2 of 0.41 and 0.59, respectively ($R^2 = 0.896$). Not unexpectedly, the higher quenching constant still is lower than the one for unhindered quenching ($0.112\%^{-1}$, see above). The same situation of course also holds if the sensor is photoexcited at 475 nm but in this case the fraction of the iridium complex that is less accessible to oxygen is negligibly small compared. This small fraction has no effect on the dynamics of quenching (f_2 in the two-site model is virtually zero), and the Stern-Volmer plot therefore is highly linear. This interpretation of the quenching mechanisms involved is further corroborated by the highly linear response of a sensor film containing the iridium probe only but no UCLNPs.[5] The large differences in precision (viz. in the standard deviation) does not come as a surprise since the xenon lamp can uniformly illuminate the whole sensor film and hence much more probe molecules than can the UCLNP nanolamps. This results in an overall higher signal and a lower standard deviation due to a much better signal-to-noise ratio.
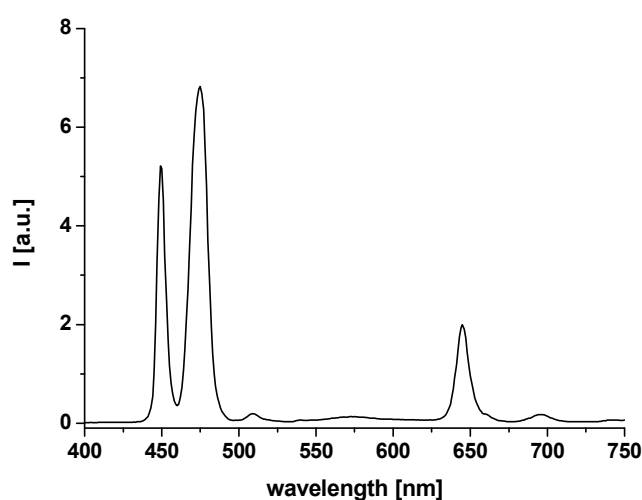
Figure 6.4: Visible spectra of the ethyl cellulose sensor film containing the UCLNPs and the oxygen probe following photoexcitation at 980 nm. The relative concentration of $[\text{Ir}(C_S)_2(\text{acac})]$ was reduced whereupon the excitation efficiency by the nanolamps and the emission of the probe decreased tremendously.

Measurements were also performed with sensor films containing different relative concentrations of UCLNPs and iridium complex. The excitation efficiency and the slope of the Stern-Volmer plot of the 980 nm laser based sensor film do not significantly change when using higher concentrations of the oxygen probe. When using less of the iridium(II) complex and the same concentration of NPs, the efficiency of excitation of the probe by the UCLNP nanolamps became marginal (Figure 6.4). Attempts to further increase in the fraction of UCLNPs in the sensor film lead to particle aggregation.

Figure 6.5 shows time traces of the signal at 568 nm with changing levels of oxygen after excitation at 475 nm (plot a) and 980 nm (plot b).
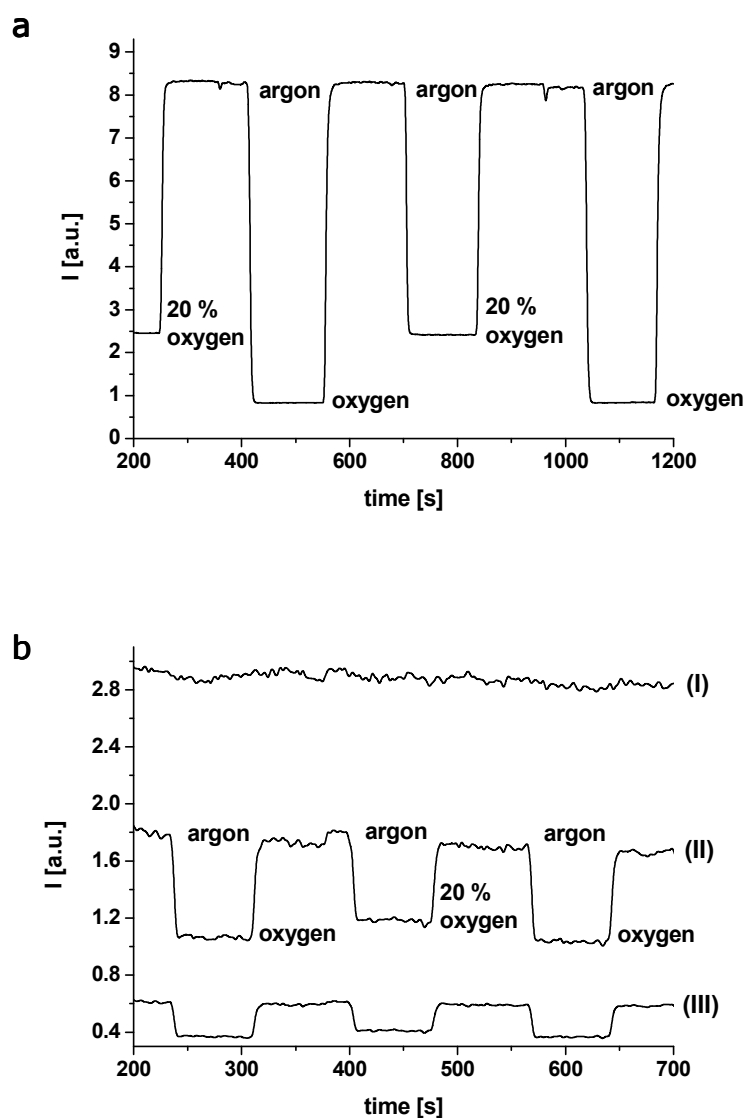
Figure 6.5: Time traces obtained with the oxygen sensor film and showing response times, reversibility, and relative signal changes. Signal obtained by (a) direct photoexcitation of the iridium(III) oxygen probe at 475 nm using a xenon lamp and (b) under photoexcitation of the UCLNPs at 980 nm and recording the green emission of the iridium probe at 568 nm when cycling between argon, nitrogen containing 20% oxygen, and pure oxygen. In (b) emissions were collected at 696 nm (trace (I)) and at 568 nm (trace (II)). Plot (III) gives the (much less noisy) ratio of the two signals (I_{568}/I_{696}).

In case of excitation at 980 nm, the emission of the UCLNPs at 696 nm also was collected (with a time delay of <1 s (caused by the instrument). The response of the sensor layer is fully reversible, and its response time is between 10 to 12 s for both excitation wavelengths. Figure 6.5 also reveals that the time trace obtained with conventional excitation (plot a) is more stable than the rather noisy trace obtained at 980 nm excitation (plot b). The larger noise in Figure 6.5b(II) is due to the overall weaker emission of the oxygen probe obtained via excitation at 980 nm, and thus a smaller signal-to-noise ratio (as discussed above), but it is probably also due to fluctuations of the intensity of the diode laser. Such fluctuations can be eliminated, in principle, by referencing the (green) signal of the iridium probe at 568 nm to the red peak of the UCLNPs at 696 nm (see band E in Figure 6.2). This band is neither involved in the photoexcitation nor does it overlap the emission of the iridium complex (Figure 6.1), and is thus an excellent reference signal that undergoes the same fluctuations as the diode laser. A fluorometer was used to determine the ration I_{568}/I_{696} within 1 s, and indeed a much less noisy signal (see trace (III) in Figure 6.5b) is obtained by forming the ratio of the signal traces (I) and (II). Obviously, however, fluctuations occurring in a time regime of less than 1 s and effects of delayed emission of the nanoparticles cannot be eliminated by this method. Also the nanolamps are suspected to cause local heating,[15] and this may lead to temperature-dependent differences in the intensity of the effects of temperature on the relative ratio of the two emission bands of the UCLNPs and the quantum yield of the iridium probe. In fact, it is presumed that the slight signal drift in Figure 6.5b(I) is partially due to local warming of the sensor film in close proximity to the UCLNPs. Moreover, the temperature dependence of the particular transitions in the UCLNPs is known not to be uniform.[16,17]

In summary, the first sensor for oxygen that can be excited with CW NIR light has been designed. Further, a new type of ratiometric readout was demonstrated. The components and materials used are readily available, and the merits of working at such long excitation wavelength

have been already discussed, the main benefit being the complete absence of luminescence background that can be strong in samples such as serum.[18] Similar approaches have been already demonstrated for pH,[1] carbon dioxide[3] and ammonia.[2] However, these are based on a quite different sensing method utilizing an inner filter effect of non-fluorescent probes. It is assumed that the method presented here can be extended to numerous other fluorescent sensing probes for various analytes.

6.3. References

1   Sun L-N, Peng H, Stich MIJ, Achatz DE, Wolfbeis OS (2009) *pH sensor based on upconverting luminescent lanthanide nanorods.* Chem Commun:5000-5002

2   Mader HS, Wolfbeis OS (2010) *Optical Ammonia Sensor Based on Upconverting Luminescent Nanoparticles.* Anal Chem 82:5002-5004

3   Ali R, Saleh SM, Meier RJ, Azab HA, Abdelgawad II, Wolfbeis OS (2010) *Upconverting nanoparticles based optical sensor for carbon dioxide.* Sensor Actuat B-Chem:150:126-131

4   Achatz DE, Meier RJ, Fischer LH, Wolfbeis OS (2011) *Luminescent Sensing of Oxygen Using a Quenchable Probe and Upconverting Nanoparticles.* Angew Chem Int Ed 50:260-263

5   Borisov SM, Klimant I (2007) *Ultrabright Oxygen Optodes Based on Cyclometalated Iridium (III) Coumarin Complexes.* Anal Chem 79:7501-7509

6   Brandrup J, Immergut EH, Grulke EA (1999) *Polymer Handbook 4th ed.,* Wiley & Sons, NY

7   Boyer J-C, van Veggel FCJM (2010) *Absolute quantum yield measurements of colloidal $NaYF_4:Er^{3+},Yb^{3+}$ upconverting nanoparticles.* Nanoscale 2:1417-1419

8   Miller JN (2005) *Fluorescent energy transfer methods in bioanalysis.* Analyst 130,:265-270

9   Morgan CG, Dad S, Mitchell AC (2008) *Present status of, and future prospects for, upconverting phosphors in proximity-based bioassay.* J Alloys Comp 451:526-529.

10   Kuningas K, Rantanen T, Ukonaho T, Lövgren T, Soukka T (2005) *Homogeneous Assay Technology Based on Upconverting Phosphors.* Anal Chem 77:7348-7355

11   Wang L, Yan R, Huo Z, Wang L, Zeng J, Bao J, Wang X, Peng Q, Li Y (2005) *Fluorescence Resonant Energy Transfer Biosensor Based on Upconversion-Luminescent Nanoparticles.* Angew Chem Int Ed 44:6054-6057

12   The authors of Ref. 9 state that "assay formats other than FRET are possible and in particular near-field coupling of upconverted emission to conventionally labeled microspheres or energy transfer from 'whispering gallery' modes at the surface of upconverting microspheres are ... possible alternatives."

13   Demas JN, DeGraff BA Coleman PB (1999) *Oxygen Sensors Based on Luminescence Quenching.* Anal Chem 71:793A-800A

14   Carraway ER, Demas JN, DeGraff BA (1991) *Luminescence quenching mechanism for microheterogeneous systems.* Anal Chem 63:332-336

15   Tikhomirov VK, Driesen K, Rodriguez VD, Gredin P, Mortier M, Moshchalkov VV (2009) *Optical nanoheater based on the Yb^{3+}-Er^{3+} co-doped nanoparticles.* Opt Express 17:11794-11798

16   Wade SA, Collins SF, Baxter GW (2003) *Fluorescence intensity ratio technique for optical fiber point temperature sensing.* J Appl Phys 94: 4743-4756

17   Fischer LH, Harms GS, Wolfbeis OS (2011) *Upconverting Nanoparticles for Nanoscale Thermometry.* Angew Chem Int Ed 50:4546-4551

18   Wolfbeis OS, Leiner M (1985) Mapping of the total fluorescence of human blood serum as a new method for its characterization. Anal Chim Acta 167:203-215

7.   Nanoparticles for Luminescent Sensing of Oxygen Using Near-Infrared Excitation

7.1. Oxygen Nanosensors Based on Upconverting Luminescent Nanoparticles

Initially, the aim was to transfer the sensing scheme based on UCLNPs and a quenchable probe for oxygen presented in the previous chapter from the sensor film to NPs. These particles were intended for the determination of oxygen distribution in cells and tissue using NIR excitation. For this purpose, $NaYF_4$:Yb,Tm encapsulated in PS (see section 4.4) were combined with the oxygen probe $[Ru(dpp)_3]TMSPS_2$ by a soaking procedure that physically entraps the transition metal complex in the polymer matrix. PS is well permeable for oxygen (P = 2.6 • 10^{13} cm^2 (s Pa)$^{-1}$).[1] Further, the excitation and emission bands of $[Ru(dpp)_3]^{2+}$ exhibit a good spectral overlap with the blue and red emitting UCLNPs (Figure 7.1) similar to the iridium(III) which was used for the sensor film in chapter 6.
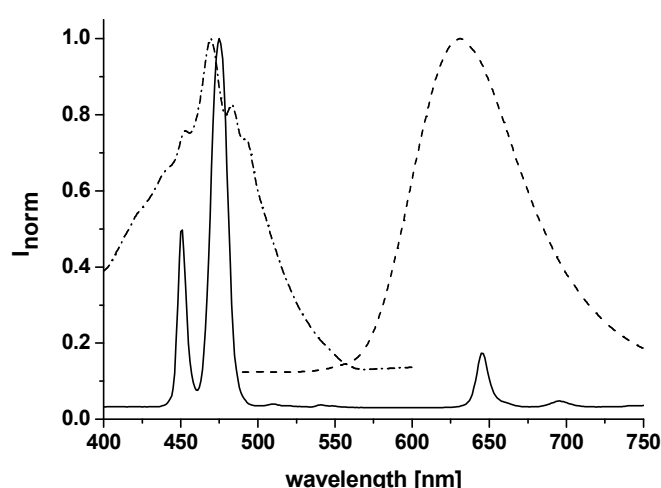
Figure 7.1: Normalized excitation and emission spectra display the spectral overlap of the emission of the $NaYF_4$:Yb,Tm UCLNPs (solid line) with the absorption of the oxygen probe $[Ru(dpp)_3]^{2+}$ (dashed-dotted line). Further, the emission of the oxygen probe (dashed line) is depicted.

The co-encapsulation of the nanophosphors and the oxygen probe should provide the spatial arrangement of the components for efficient excitation of the ruthenium(II) complex by the UCLNPs nanolamps upon excitation at 980 nm. Aqueous solutions of $NaYF_4$:Yb,Tm@PS as well as of

NaYF$_4$:Yb,Tm@NaYF$_4$@PS soaked with [Ru(dpp)$_3$]TMSPS$_2$ revealed too much scattering at concentrations required for a sufficient luminescence signal. Hence, NaYF$_4$:Yb,Tm@PS co-doped with the oxygen probe were spread on a glass plate, dried at room temperature and placed in a flow-through cell. This chamber was equipped with a fiber optic for 980 nm diode laser excitation and emission collection via another fiber optic cable. Figure 7.2a displays the spectrum upon CW NIR excitation. As it was already described in detail for a similar concept in chapter 6, the blue emission of the UCLNPs is reduced since the particles act as nanolamps for the excitation of the ruthenium(II) probe. The emission maximum of the latter is shifted to a lower wavelength compared to the emission spectrum collected from solution (Figure 7.1) and emerges around 600 nm.
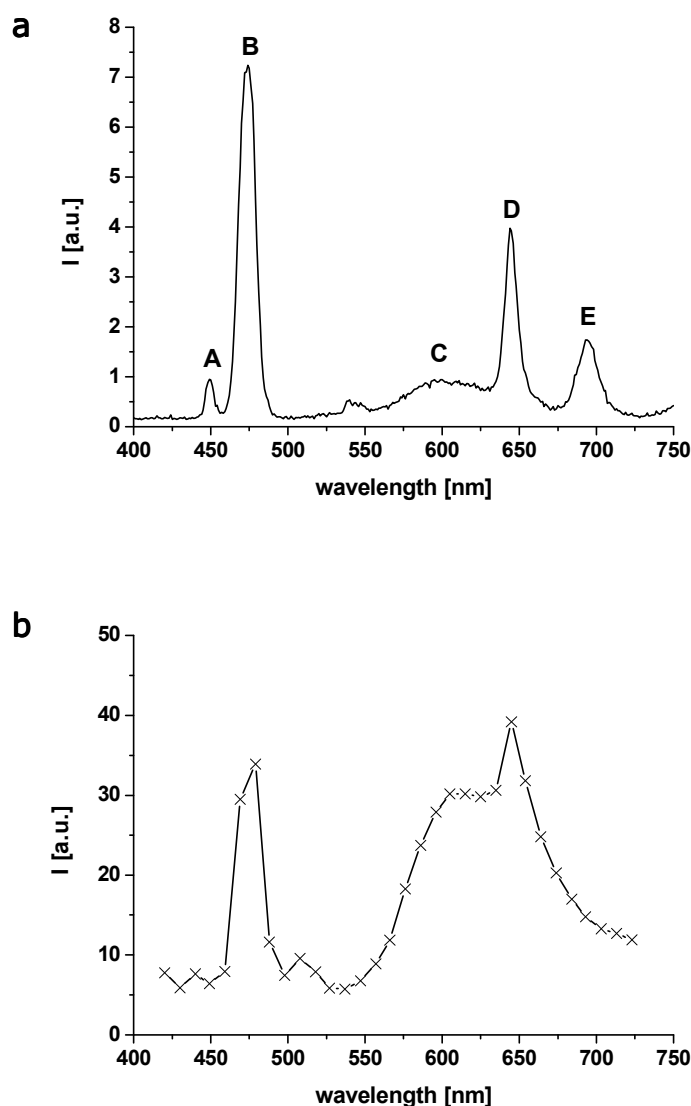
Figure 7.2: Upconversion luminescence spectrum of dried UCLNP@PS capsules that were soaked with the oxygen probe [Ru(dpp)$_3$]TMSPS$_2$ upon excitation with a 980 nm CW diode laser (a). The blue emission of the UCLNPs (band A, B) is screened off by the oxygen probe (compare Figure 6.2a). The probe molecules are photoexcited by the nanophosphors (C). The red emissions of the UCLNPs are almost unaffected (band D, E). Compared to spectrum (a), the emission of the oxygen probe upon excitation with a short-pulsed 980 nm laser is intensified (b). This reveals that not only excitation by the UCLNP nanolamps but also by the pulsed laser beam via TPE occurs.

These oxygen nanosensors were further investigated by laser scanning microscopy with a 980 nm short-pulsed laser as excitation source (compare section 5.3). During these experiments it was learnt that the oxygen probe [Ru(dpp)$_3$]TMSPS$_2$ displays efficient luminescence not exclusively upon excitation by the UCLNP nanolamps but also upon two-photon excitation (TPE) by the NIR laser pulses. This was revealed by the luminescence spectrum of the capsules constructed from two-photon laser scanning microscopy (TPLSM) using wavelength-resolved emission collection (Figure 7.2b).[2] Under short-pulsed NIR laser excitation the nanosensor particles display an tremendously enhanced emission of the ruthenium(II) complex around 600 nm compared to CW NIR laser excitation (Figure 7.2a). These results and the lack of a microscope equipped with a CW NIR excitation source made the use of UCLNPs as "transmitter" of NIR excitation to the probe molecules in the sensor particles impossible.

7.2. Particles for Sensing of Oxygen Based on Two-Photon Excitation

7.2.1. Preparation of the Sensor Particles, Experimental Setup

Instead of the approach of using UCLNPs as nanolamps described above, commercially available PSNPs were loaded with the oxygen probe [Ru(dpp)$_3$]TMSPS$_2$ and investigated for TPE based oxygen sensing. Amino-modified PSNPs with a suitable average size of 85 ± 19 nm were on hand and used for this purpose. The soaking procedure was done in a modification of the method of Behnke et al.[3] by swelling the particles in a THF-water mixture in presence of the ruthenium(II) complex. Thus well dyed PS nanospheres, denoted as PSNP(Ru) in the following, were obtained. The size and the size distribution of the PSNPs were determined by PCS before and after the swelling procedure to exclude dissolving or aggregation of the PSNPs by THF. They were found to be well monodisperse before (117 ± 3 nm; PI = 0.07) and after (121 ± 3 nm; PI

= 0.04) the loading with dye molecules while the hydrodynamic radius of the particles remains virtually unchanged (see enclosed CD). Further, the hydrodynamic radius is in good accordance with the average particle size (85 ± 19 nm) given in the specifications of the distributor.

The luminescence of aqueous solutions of PSNP(Ru) (0.4wt%) upon continuous VIS and short-pulsed NIR laser excitation was investigated. The 488 nm emission of an argon laser is well suited for conventional excitation of the ruthenium(II) probe (see excitation spectrum in Figure 7.1). For TPE, a mode-locked Ti:sapphire laser with an output wavelength of 830 nm and an average pulse duration of 75 fs was applied. The setup and the procedure of the measurements are described in detail in the Experimental Part. The wavelength for TPE was chosen according to Kawamata et al.[4] who estimated the TPA cross-section of the ruthenium(II) complex to be 210 GM at 830 nm.[5]

7.2.2. Investigations on Laser Power Dependency

The nature of the absorption process under both types of laser excitation was examined by measuring the luminescence as a function of the laser power. The solution was irridiated with the respective laser beam and the excitation power of the argon laser was varied between 0.03 to 2.54 mW, the power of the Ti:sapphire laser between 25 and 125 mW. The laser power was raised and again decreased to the lowest output while acquiring spectra between 215 and 780 nm in certain intervals. A comparison of the emission upon conventional absorption and TPA normalized to 630 nm is displayed in Figure 7.3a. The bands are congruent despite the different excitation mechanism. The diverging cut-offs are due to filters in the optical path of the respective laser. Further, the double-logarithmic plots of laser power versus emission intensity for VIS (Figure 7.3b) and NIR laser excitation (Figure 7.3c) are displayed.
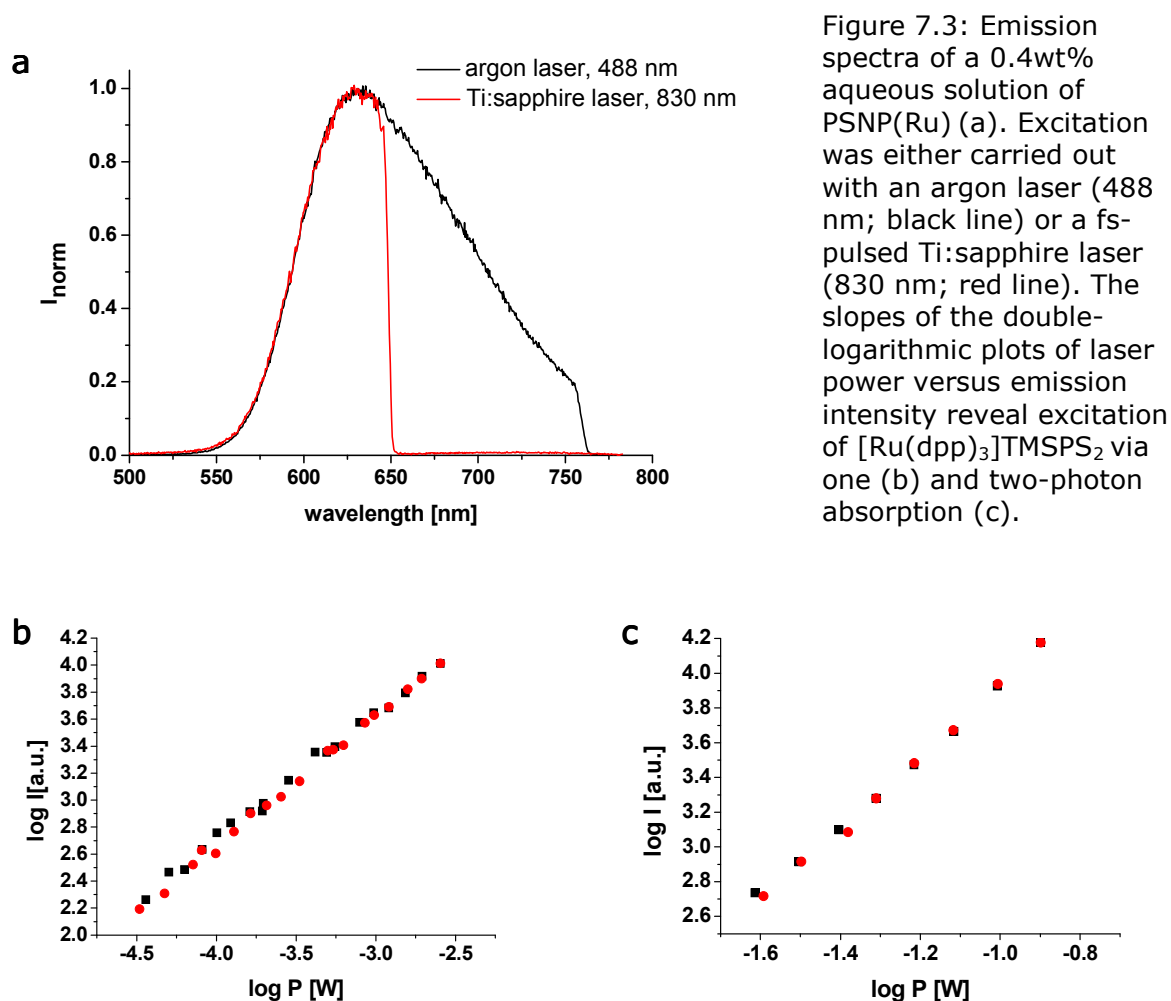
Figure 7.3: Emission spectra of a 0.4wt% aqueous solution of PSNP(Ru) (a). Excitation was either carried out with an argon laser (488 nm; black line) or a fs-pulsed Ti:sapphire laser (830 nm; red line). The slopes of the double-logarithmic plots of laser power versus emission intensity reveal excitation of $[Ru(dpp)_3]TMSPS_2$ via one (b) and two-photon absorption (c).

Both correlations are linear within the investigated range. The average slopes are found to be 0.95 (Figure 7.3b) and 2.04 (Figure 7.3c) clearly revealing the absorption of one photon of the wavelength 488 nm and two photons of the wavelength 830 nm.

7.2.3. Sensing of Oxygen with One- and Two-Photon Excited Luminescence

$[Ru(dpp)_3]TMSPS_2$ is a well established probe for sensing oxygen demanding a simple blue LED as the light source.[6] Due to the congruent emission spectra upon one- and two-photon absorption (Figure 7.3a), both excitation pathways were expected to populate the same triplet state whose emission is efficiently quenched by oxygen. Hence, the response of

the luminescence upon VIS and short-pulsed NIR laser excitation was investigated and compared. Oxygen-free aqueous solutions containing PSNP(Ru) were flushed for 5 min. each with argon-oxygen mixtures of raising oxygen content (20, 40, 60, 80, 100%). These were prepared using a home-made computer controlled gas mixing device and passed through the solution with a cannula. Spectra of the solutions upon excitation with both laser types were acquired using a CCD camera. During the measurements a slight signal drift was observed when the solutions were flushed with the respective gas mixture for more than 5 min. Further, it was essential to start with oxygen-free particle suspensions and to raise the oxygen content of the gas flow from 20 to 100 %. It was not possible to obtain reproducible results from the same solution when the percentage of oxygen was again decreased. This is supposed to be due to incomplete saturation of the water phase with the respective gas mix after 5 min. Nevertheless, this time interval was chosen to allow for a reasonable performance of the experiment.
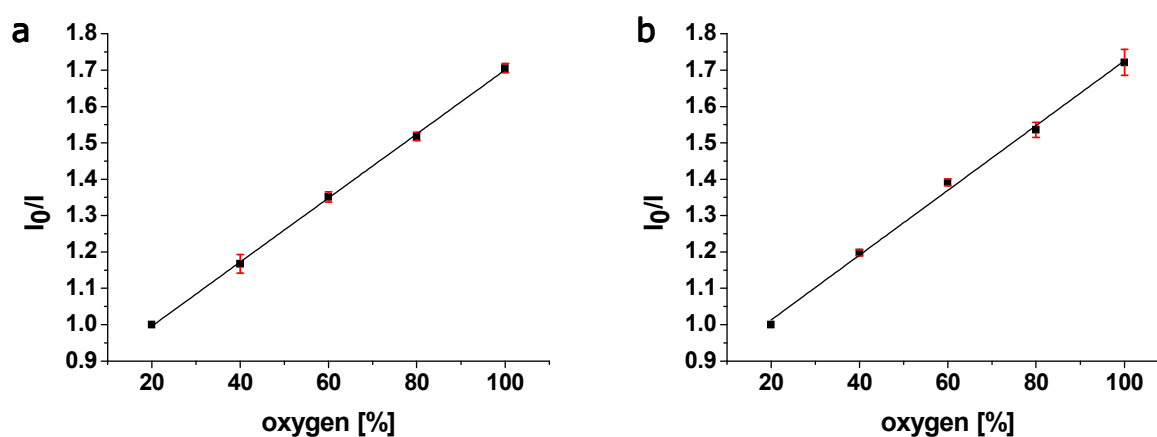
Figure 7.4: Stern-Volmer plots of the emission quenching by oxygen of [Ru(dpp)$_3$]TMSPS$_2$ encapsulated in PSNPs in aqueous solution. The oxygen nanoprobes were excited either with an argon laser (488 nm; (a)) or a fs-pulsed Ti:sapphire laser (830 nm; (b)). Identical quenching efficiencies were obtained for both excitation sources with oxygen concentrations ranging from 20 to 100%.

The measurements were carried out according to the protocol given in detail in the Experimental Part yielding highly reproducible results. The respective Stern-Volmer plots obtained from VIS and NIR excitation

(average of 3 independent measurements for each oxygen concentration) are displayed in Figure 7.4. Both plots are linear ($R^2 = 1$) according to the Stern-Volmer relation

$$\frac{I_0}{I} = 1 + K_{SV} \cdot [O_2]$$
(Equation 2)

with a high precision expressed as the standard deviation. The quenching constants (K_{sv}) were calculated to be 0.009%$^{-1}$, respectively.

Hence, the oxygen probe [Ru(dpp)$_3$]TMSPS$_2$ is also well suited for sensing of oxygen upon TPE. This constitutes a new approach since so far conventional oxygen probes were combined with different kinds of antennas (see section 2.3.4).[7,8,9] This might be mainly due to the fact that platinum(II) porphyrins were utilized as the oxygen sensitive part of these nanosensor. Compared to the ruthenium(II) complex used here, these porphyrins offer some general advantages in oxygen sensing applications like more narrow excitation and emission bands and a higher sensitivity.[10] Nevertheless, their TPA cross-sections are very low, in the order of a few GM units.[11] Moreover, the combination with antenna molecules yields TPA cross-sections that still are usually below 100 GM.[12] In contrast, [Ru(dpp)$_3$]TMSPS$_2$ offers a comparatively high TPA cross-section of 210 GM[4] without further modifications. Additionally, the sensor NPs described above can be easily prepared from commercially available products.

7.3. Investigations on Multicellular Spheroids Using Confocal and Two-Photon Laser Scanning Microscopy

The PSNP(Ru) were intended to be tested for two-photon excitation based oxygen sensing in deep tissue. Multicellular spheroids (MCS) of a breast cancer cell line (MCF-7; Michigan Cancer Foundation-7) were chosen as model system. Over the last decades, such spheroids have become popular 3D model systems since they mimic living tissues (especially tumors) much better than cell monolayers.[13] The spheroids can be grown

to diameters of several 100 microns within a few days after their formation. It was reported that a microenvironment evolves inside the spheroids when they exceed a certain diameter of about 500 μm. It consists of a necrotic core, a viable but quiescent cell layer in the middle, and viable and proliferating outer cells.[14,15] The penetration depth of CLSM (< 100 μm)[16] is not sufficient to gain information from the interior of the MCS. So far, parameters like pH or oxygen distribution in their interior were mainly investigated using microelectrodes.[17] Nonlinear excitation with NIR light in TPLSM offers enhanced tissue penetration compared to CLSM and is a non-invasive method. The PSNP(Ru) sensor particles were tested for imaging the oxygen distribution in MCS via TPLSM. It is assumed that oxygen diffusion is not hindered throughout the spheroids. The necrotic core does not consume oxygen and hence the fluorescence signal from oxygen sensitive probes in the center of the MCS is expected to be quenched. In contrast the viable cell layers consume oxygen entailing a higher luminescence signal. The experiments were carried out in cooperation with the workgroup of Prof. Wegener and particularly Christina Hupf who incorporated the NPs in the spheroids and investigated their distribution therein.

7.3.1. Biocompatibility of the Sensor Nanoparticles

Prior to incorporation, the biocompatibility of PSNP(Ru) was tested by performing an AlamarBlue® cell viability assay (see also section 5.2) according to the protocol that is described in detail in the Experimental Part. MCF-7 cells were grown to confluent monolayers in a 96-well microtiter plate (MTP) and incubated with a different number of the sensor NPs at 37 °C for 24 h. The number of NPs per volume was calculated according to Equation 3 which is given in the Experimental Part. Again control experiments without particles (maximal growth) and with Triton (minimal growth) were performed. The results of the assay are displayed in Figure 7.5. The particles reveal minor cytotoxicity with a cell growth of still 87% for the highest concentration of NPs tested.
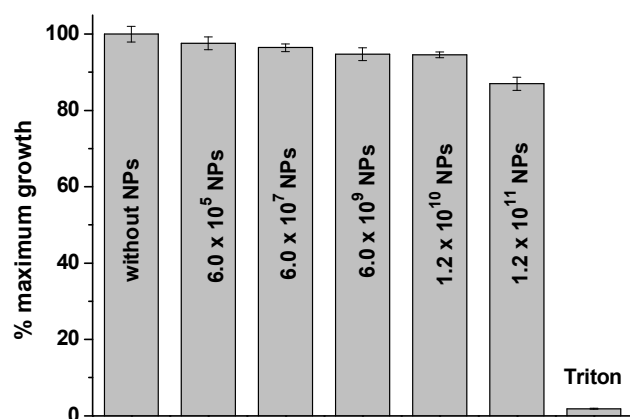
Figure 7.5: Results of the AlamarBlue® cell viability assay of MCF-7 cells incubated with different amounts ($\sim 10^6$ to 10^{11}) of PSNP(Ru) at 37 °C for 24 h. Standard deviations were obtained from six wells representing six parallel experiments.

Further the spheroid formation and growth in the presence of the amino-modified PSNP(Ru) was monitored. It is assumed that cell uptake of the NPs occurs and hence also incorporation in the interior of the MCS. The procedure was established and carried out by Christina Hupf within her master thesis (details see Experimental Part).[18]
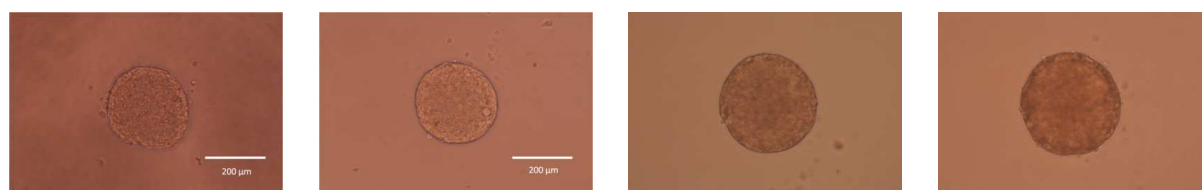
Figure 7.6: MCF-7 spheroids were incubated with different amounts of PSNP(Ru) during their formation. The phase contrast micrographs display an spheroid exemplarily after one, two, five and six days (from left to right) after the transfer of the cells to agarose-coated microtiter plates. The length of the scale bars is 200 µm.

Figure 7.6 displays phase contrast micrographs of a MCF-7 spheroids exposed to latex beads during its formation. Formation of the MCS is not impacted by the presence of the NPs. There are slightly smaller in size compared to MCS grown without particles.[18] However, these pictures do not reveal whether the latex beads were assimilated by the cells or how they are distributed in the spheroid.

7.3.2. Visualization of the Sensor Nanoparticles Inside Multicellular Spheroids Using Laser Scanning Microscopy

Cell uptake of the PSNP(Ru) and their distribution inside the MCS was investigated using laser scanning microscopy. Both, conventional one-photon excitation with an argon laser (488 nm) and TPE with a short-pulsed NIR laser (860 nm), were applied and compared regarding penetration depth. The spheroid that was investigated was allowed to grow for 8 days after incubation with the NPs (1.2 $\cdot$ 10^{10} NPs). The diameter of the spheroid was found to be about 450 nm (Figure 7.7a). Micrographs of this spheroid recorded upon conventional excitation (Figure 7.7b) and TPE (Figure 7.7c) are displayed showing xy-sections in diverse z-planes from the surface to the central plane.

Figure 7.7: Phase contrast micrograph of a MCF-7 spheroid that was allowed to grow for 8 days after incubation with PSNP(Ru) during its formation. The length of the scale bar is 100 µm revealing a total diameter of about 450 µm (a). Xy-sections of this MCS obtained from CLSM (λ_{exc} = 488 nm; (b)) and TPLSM (λ_{exc} = 860 nm; (c)) in diverse z-planes (0 to 165 µm) are displayed.
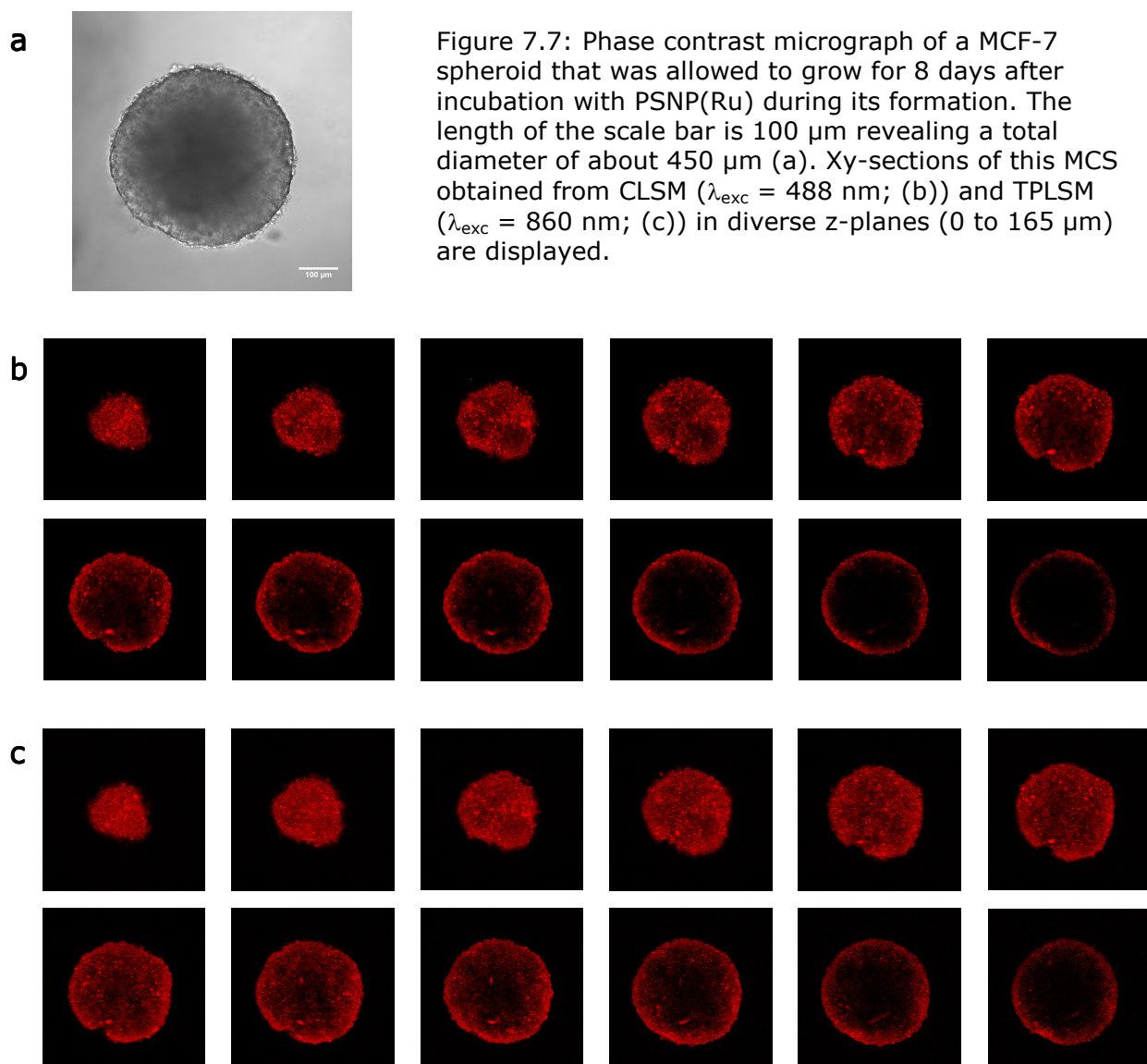
The z-plane resolved images indicate a somewhat higher penetration depth of the short-pulsed NIR laser beam (Figure 7.7c) compared to CLSM (Figure 7.7b) using the argon laser. The tissue penetration was further quantified by measuring the signal intensity of the luminescence across the spheroid along the x-axis of each micrograph.[19]
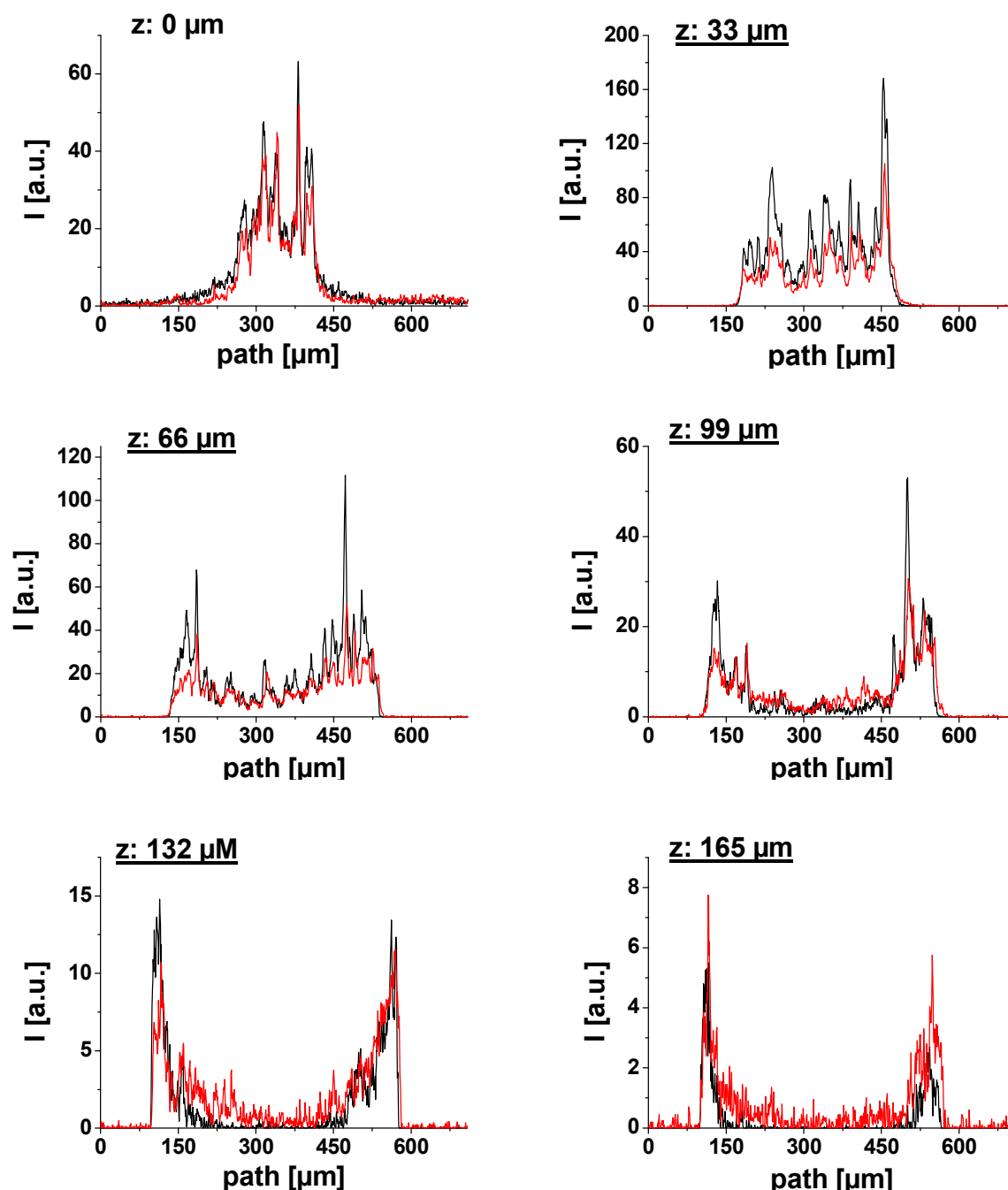
Figure 7.8: Intensity plots across the spheroid along the x-axis in different z-planes for VIS (black lines) and NIR excitation (red lines). For a z-depth of about 100 µm and more a slightly higher penetration depth for TPE can be observed.

Figure 7.8 displays the plots of the signal intensity upon excitation at 488 nm (black lines) and excitation at 860 nm (red lines) for certain z-planes. Surprisingly, there is only a minor difference between the results obtained from CLSM and TPLSM. Above 100 µm a slightly higher penetration depth can be observed upon short-pulsed NIR excitation. One conceivable reason for this is that the NIR light features the ability to penetrate tissue deeper than VIS light but the resulting VIS emission of the PSNP(Ru) at 630 nm is weakened at its way out of the spheroid. Secondly, it is not ensured whether the NPs are homogeneously distributed across MCS as a whole or mainly located in the outer cell layers. Further investigations on ultra-thin cross sections of the spheroids (after fixation, dehydration and embedding in a synthetic resin) were performed by TEM. Unfortunately, the PSNPs are dissolved during the preparation protocol rendering it impossible to make an educated guess about their location inside the spheroid. However, the difference in signal intensity between the outer cell layers and layers deeper in the interior of the MCS (Figure 7.7, Figure 7.8) can not be ascribed to varying oxygen concentrations.

Hence, imaging of the oxygen distribution could not be accomplished inside the tumor model system using TPE of the PSNP(Ru) nanosensor. Nevertheless, the particles are equally capable of sensing of oxygen upon conventional VIS and short-pulsed NIR excitation. Not only luminescence of oxygen sensitive probes is quenched but also their lifetime. Thus time-resolved measurements can overcome limitations of the intensity-based experiment while maintaining the benefit of higher penetration depth of NIR excitation light. Further investigations on oxygen sensing with PSNP(Ru) and the particle distribution inside MCS are required.

7.4. References

1   Brandrup J, Immergut EH, Grulke EA (1999) *Polymer Handbook 4th ed.,* Wiley & Sons, NY

2   NaYF$_4$:Yb,Tm@PS soaked with [Ru(dpp)$_3$]TMS$_2$ were spread on a microscopy slide. The sample was investigated by laser scanning microscopy under excitation with a 860 nm fs-pulsed raster scanning laser beam (256 mW). Images of the VIS emission (400 to 750 nm) of a focused region were collected within spectral windows of 10 nm each. The integrated intensities of these images were used for the construction of Figure 7.2b.

3   Behnke T, Würth C, Hoffmann K, Hübner M, Panne U, Resch-Genger U (2011*) Encapsulation of Hydrophobic Dyes in Polystyrene Micro- and Nanoparticles via Swelling Procedures.* J Fluoresc 21:937-944

4   Kawamata J, Ogata Y, Yamagishi A (2002) *Two-Photon Fluorescence Property of Tris(4,7-Diphenyl-1,10-phenantroline)ruthenium(II)perchlorate.* Mol Cryst Liq Cryst 379:389-394

5   Goeppert-Mayer unit; 1 GM = 10^{-50} cm^{4}s/photon

6   Apostolidis A, Klimant I, Andrzejewski D, Wolfbeis OS (2004) *A Combinatorial Approach for Development of Materials for Optical Sensing of Gases.* J Comb Chem 6:325-331

7   Lebedev AY, Troxler T, Vinogradov SA (2008) *Design of Metalloporphyrin-Based Dentritic Nanoprobes for Two-Photon Microscopy of Oxygen.* J Porphyr Phtalocya 12:1261-1269

8   Wu C, Bull B, Christensen K, McNeill J (2009) *Ratiometric Single-Nanoparticle Oxygen Sensors for Biological Imaging.* Angew Chem Int Ed 48:2741-2745

9   McLaurin EJ, Greytak AB, Bawendi MG, Nocera DG (2009) *Two-Photon Absorbing Nanocrystal Sensors for Ratiometric Detection of Oxygen.* J Am Chem Soc 131:12994-13001

10   Amao Y (2003) *Probes and Polymers for Optical Sensing of Oxygen.* Microchim Acta 143:1-12

11   Kruk M, Karotki A, Drobizhev M, Kuzmitsky V, Gael V, Rebane A (2003) *Two-photpn absorption of tetraphenylporphyrin free base.* J Luminesc 105:45-55

12   Briñas RP, Troxler T, Hochstrasser RM, Vinogradov SA (2005) *Phosphorescent Oxygen Sensor with Dentritic Protection and Two-Photon Absorbing Antenna.* J Am Chem Soc 127:11851-11862

13   Pampaloni F, Reynaud EG, Stelzer EHK (2007*) The third dimension bridges the gap between cell culture and live tissue.* Nat Rev Mol Cell Biol 8:839-845

14   Wartenberg M, Acker H (1995) *Quantitative Recording of Vitality Patterns in Living Multicellular Spheroids by Confocal Microscopy.* Micron 5:395-404

15   Lin R-Z, Chang H-Y (2007) *Recent advances in three-dimensional multicellular spheroid culture for biomediacl research.* Biotechnol J 3:1172-1184

16   Helmchen F, Denk W (2005) *Deep tissue two-photon microscopy.* Nat Methods 2:932-941

17   Mueller-Klieser W, Freyer JP, Sutherland RM 1986) *Influence of glucose and oxygen supply conditions on the oxygenation of multicellular spheroids.* Br J Cancer 53:345-353

18   Hupf C (2012) *Impact of Nanoparticles on Two- and Three-Dimensional Cell Cultures.* Master Thesis, University of Regensburg

19   Measurements on the microscope yielded z-stacks of the spheroid under the two different excitation modes. A linear range across the spheroid along the x-axis of this stacks was selected and measured using the respective tools of the MacBiophotonics ImageJ software.

8. Experimental Part

8.1. Materials and Methods

All chemicals and solvents were purchased in analytical grade from Merck (www.merck-chemicals.de), Sigma-Aldrich (www.sigma-aldrich.com) and ABCR (www.abcr.de) and were used without further purification unless otherwise stated.

Luminescence excitation and emission spectra based on VIS light were acquired with a Jasco FP6300 luminescence spectrometer (www.jascoinc.com). Upconversion luminescence spectra were recorded on a Varian Cary Eclipse fluorometer (www.varianinc.com). The latter was equipped with an external, continuously adjustable 980 nm fiber optic CW diode laser (5 W maximum power; from Roithner Lasertechnik; www.roithner-laser.com). Spectra are uncorrected and were collected in the Bio-, Chemiluminescence mode of the instrument at an output power of 1 W with an emission slit width of 5 nm and a PMT voltage of 900 V unless otherwise stated.

TEM pictures were recorded at the department of pathology of the University Hospital Regensburg on a 120 kV LEO 912AB from Zeiss (www.zeiss.de) equipped with a CCD-camera.

FTIR spectra were recorded with a Varian 670-IR spectrometer, XRD spectra with a Stadi P from STOE & CIE (www.stoe.com) at the Institute of Inorganic Chemistry, University of Regensburg (workgroup Prof. Dr. Pfitzner). DRIFT spectroscopy was performed with a Jasco FT/IR-610 (www.jascoinc.com), TGA with a Perkin-Elmer TGA 7 (www.perkinelmer.com) at the Institute of Physical Chemistry, University of Regensburg (workgroup Prof. Dr. Kunz).

PCS was also performed at the Institute of Physical Chemistry with a Malvern Zetasizer 3000. Zeta potential was measured with a Malvern Zetasizer Nano S (www.malvern.com).

Phase contrast microscopy was performed on a Nikon Diaphot equipped with a digital camera D 5000 from Nikon (www.nikon.com). CLSM and TPLSM images were taken on a Zeiss LSM 710 (controlled by ZEN software) equipped with an argon laser and a tuneable Chameleon Coherent MRU-X1 modelocked Ti:sapphire laser (www.coherent.com) for TPE.

8.2. Syntheses of Upconverting Luminescent Nanoparticles

8.2.1. Synthesis of NaYF$_4$:Yb,X (X = Er^{3+}, Tm^{3+}) via Co-precipitation Followed by Thermal Treatment

Synthesis of NaYF$_4$:Yb,X (X = Er^{3+}, Tm^{3+}) via co-precipitation followed by thermal treatment was carried out according to the protocol of Yi et al.[1] The molar ratio of Y^{3+}/Yb^{3+}/X^{3+} was 78/20/2 in NaYF$_4$:Yb,Er and 79.5/20/0.5 in NaYF$_4$:Yb,Tm. Therefore, 0.2 M aqueous stock solutions of EDTA (Titriplex III) and the hexahydrates of YCl$_3$ (99,990%), YbCl$_3$ (99,900%), ErCl$_3$ (99,995%) or TmCl$_3$ (99,990%) were prepared. The solutions of the RE chlorides were adjusted to pH 2 using hydrochloric acid. Afterwards, the respective volumes for the desired doping ratios (see Table 4) were mixed with EDTA. In parallel, NaF (2.1 g) was dissolved in 60.0 mL of water. The RE-EDTA mixture was rapidly injected into the fluoride solution with a syringe under vigorous stirring which was continued for 1 h. The particles were collected by centrifugation and washed two times with water and two times with ethanol by repeated centrifugation-redispersion cycles (4,000 rpm, 30 min.). A colorless solid was obtained and dried at 50 °C for 1 h and ground in a mortar. Portions of 100 mg each were put in round bottom flasks (25.0 mL), thoroughly flushed with argon and closed with a glass stopper. These were placed in a muffle furnace and heated to 400 °C in 30 min. The particles were tempered for 5 h at ambient temperature. After cooling to room temperature, the particles were again ground in a mortar and stored in solid phase at room temperature.

UCLNPs	0.2 M EDTA [mL]	0.2 M YCl$_3$ [mL]	0.2 M YbCl$_3$ [mL]	0.2 M ErCl$_3$ [mL]	0.2 M TmCl$_3$ [mL]
NaYF$_4$:Yb,Er (20/2)	20.0	15.6	4.0	0.4	-
NaYF$_4$:Yb,Tm (20/0.5)	20.0	15.9	4.0	-	0.1

Table 4: Volumes of 0.2 M stock solutions used for preparation of NaYF$_4$:Yb,X (X = Er^{3+}, Tm^{3+}) via co-precipitation. The total amount of RE ions was held at 4.000 mmol and the ratio of RE^{3+}/EDTA was 1/1.

8.2.2. Synthesis of NaYF$_4$:Yb,X (X = Er^{3+}, Tm^{3+}) via Thermal Decomposition

Synthesis of NaYF$_4$:Yb,X (X = Er^{3+}, Tm^{3+}) by thermal decomposition was performed according to a protocol of Li et al.[2] The doping ratio was 78/20/2 in NaYF$_4$:Yb.Er and 79.5/20/0.5 in NaYF$_4$:Yb,Tm. A total amount of 1.000 mmol of the hexahdrates of YCl$_3$ (99,990%), YbCl$_3$ (99,900%), ErCl$_3$ (99,995%) or TmCl$_3$ (99,990%) were mixed with OA (vegetable, Ph Eur; 6 mL) and OD (technical grade, 90%; 15.0 mL) in a 100.0 mL round bottom flask (see Table 5). The suspension was heated under vigorous stirring to 150 °C in an oil bath for 30 min. to dissolve the salts. In parallel, NH$_4$F (4.000 mmol/ 0.1484 g) and NaOH (2.500 mmol/ 0.1000 g) were dissolved in 10.0 mL of methanol and added dropwise to the cooled RE solution during stirring. The suspension was stirred for two hours at room temperature before heating to 90 °C for 30 min. under a flow of argon to remove the methanol. After cooling to room temperature, the mixture was transferred in a 50.0 mL three-necked round bottom flask equipped with an air cooler and an internal temperature sensor. Under a very gentle flow of argon the suspension was stirred and heated to 300 °C using a mantle connected to a control device and the internal temperature sensor. Argon was turned off once this temperature was reached. The temperature was curtailed within a very close interval of 300 ± 2 °C for 90 min. The solution was allowed to cool to room temperature and UCLNPs were precipitated by adding 15.0 mL of ethanol and collected by

centrifugation (4,000 rpm, 10 min.). After washing twice with ethanol and once with acetone by repeated centrifugation-redispersion cycles, the off-white solid was dried, ground in a mortar and stored at room temperature.

UCLNPs	Y^{3+} [mmol]/[g]	Yb^{3+} [mmol]/[g]	Er^{3+} [mmol]/[g]	Tm^{3+} [mmol]/[g]
NaYF$_4$:Yb,Er (20/2)	0.780/ 0.2366	0.200/ 0.0775	0.020/ 0.0076	-
NaYF$_4$:Yb,Tm (20/0.5)	0.795/ 0.2412	0.200/ 0.0775	-	0.005/ 0.0019

Table 5: Amounts of RE precursor salts of the respective ions used for the synthesis of NaYF$_4$:Yb,X (X = Er^{3+}, Tm^{3+}) via thermal decoposition.

8.2.3. Synthesis of Multicolor Upconverting Luminescent Nanoparticles

The multicolor UCLNPs were synthesized via thermal decomposition (see section 8.2.2). The RE precursors that have been used additionally for the preparation of NaYF$_4$;Yb,Ho,Ce[3] are HoCl$_3$ • 6 H$_2$O and CeCl$_3$ • 7 H$_2$O. The amounts of OA (6.0 mL), OD (15.0 mL), NaOH (2.500 mmol/ 0.1000 g) and NH$_4$F (4.000 mmol/ 0.1484 g) were constant for all types of particles.

UCLNPs	Y^{3+} [mmol] [g]	Yb^{3+} [mmol] [g]	Er^{3+} [mmol] [g]	Tm^{3+} [mmol] [g]	Ho^{3+} [mmol] [g]	Ce^{3+} [mmol] [g]
NaYF$_4$:Yb,Er (20/2)	0.780 0.2366	0.200 0.0775	0.020 0.0076	-	-	-
NaYF$_4$:Yb,Tm (20/0.5)	0.795 0.2412	0.200 0.0775	-	0.005 0.0019	-	-
NaYF$_4$:Yb,Er,Tm (20/0.1/0.5)	0.794 0.2409	0.200 0.0775	0.001 0.0004	0.005 0.0019	-	-
NaYF$_4$:Yb,Ho,Ce (20/2/15)	0.630 0.1911	0.200 0.0775	-	-	0.020 0.0076	0.150 0.0559
NaYF$_4$:Yb,Ho,Ce (20/2/30)	0.480 0.1456	0.200 0.0775	-	-	0.020 0.0076	0.300 0.1118

Table 6: Amounts of RE precursor salts of the respective ions used for the synthesis of multicolor UCLNPs via thermal decoposition.

8.3. Surface Modification of Upconverting Luminescent Nanoparticles

8.3.1. Synthesis of NaYF$_4$:Yb,X@NaYF$_4$ (X = Er^{3+}, Tm^{3+})

The synthesis of NaYF$_4$:Yb,X@NaYF$_4$ (X = Er^{3+}, Tm^{3+}) was performed in a modification of the protocol of Guo et al.[4] YCl$_3$ · 6 H$_2$O (0.500 mmol/ 0.1517 g) was added to OA (3.0 mL) and octadecene (7.5 mL) and the mixture was heated to 150 °C in an oil bath under stirring to obtain a clear yellowish solution. In parallel, 0.0940 g of NaYF$_4$:Yb,Er (20/2) or NaYF$_4$:Yb,Tm (20/0.5) synthesized via thermal decomposition as described above were suspended in 5.0 mL of hexane by sonication. The particles were added dropwise to the cooled RE solution and heated to 80 °C under a flow of argon to remove the hexane. NH$_4$F (2.000 mmol/ 0.0742 g) and NaOH (1.250 mmol/ 0.0500 g) were dissolved in 10.0 mL of methanol and added dropwise to the UCLNP-RE-mixture under stirring and heated to 90 °C under a flow of argon to remove the methanol. After cooling to room temperature, the suspension was transferred into a 50.0 mL three-necked round bottom flask equipped with a gas inlet, an air cooler and an internal temperature sensor. The mixture was heated to 260 °C while stirring and gentle flushing with argon. As soon as the temperature was reached, the argon flow was turned off and the temperature was kept at 260 ± 2 °C for one hour. After cooling to room temperature, the core-shell UCLNPs were precipitated by adding 15.0 mL of ethanol and collected by centrifugation (4,000 rpm, 10 min.). The particles were washed twice with ethanol and once with acetone by repeated centrifugation-redispersion cycles. After drying at room temperature over night, the particles were ground in a mortar and stored in solid form.

8.3.2. Ligand Exchange Reactions with Carboxylic Acids

Ligand exchange reactions of the oleic acid on UCLNPs prepared via thermal decomposition were performed according to an approach of Lattuada et al.[5] The nanophosphors (0.1200 g) were dispersed in a

mixture (1:1) of DMF (dimethylformamide) and DCB (1,2-dichlorbenzene) using a sonication bath. RA (3.350 mmol/ 1.0000 g) or CA monohydrate (0.540 mmol/ 0.1140 g) was added and the mixture was stirred for 24 h at 100 °C. After cooling to room temperature, UCLNP@RA were precipitated by the addition of 40.0 mL of methanol and 2.0 mL of water, UCLNP@CA by the addition of 40.0 mL of diethylether. The particles were isolated by centrifugation and the RA treated UCLNPs were washed three times with aceton, the CA treated NPs three times with methanol by repeated centrifugation-washing cycles. The obtained nanophosphors were dried, ground in a mortar and stored at room temperature.

8.3.3. Silica Coating via the Stöber Method

UCLNPs (30.0 mg) prepared via the co-precipitation method followed by thermal treatment were dispersed in 80.0 mL of ethanol and 7.5 mL of water in a 100 mL round bottom flask by means of a sonication bath (10 min.). 0.5 mL of an aqueous ammonia solution (25%) were added, the flask was sealed with a glass stopper and the dispersion was heated to 40 °C under gentle stirring. After the addition of 0.1 mL of TEOS, the mixture was kept at this temperature for 3 h. UCLNP@SiO$_2$ were collected by centrifugation (4,000 rpm, 20 min.) and washed three times with ethanol and one time with water by repeated centrifugation-redispersion cycles. The silica coated nanophosphors were redispersed in 10.0 mL of water and stored in a head-over tumbling unit to prevent accelerating agglomeration.

8.3.4. Silica Coating via Reverse Microemulsion

Coating of UCLNPs prepared by thermal decomposition was carried out according to the protocol of Jalil et al.[6] The nanophosphors (7.4 mg) were dispersed in 10.0 mL of cyclohexane in a 10 mL round bottom flask by sonication. Igepal CO-520 (0.5 mL) was added and mixed with the solvent

by shaking to form a homogeneous solution. Ammonia solution (25% in water; 80 µL) was added, the flask was sealed and sonicated for 20 min. Finally TEOS was added (0.180 mmol/ 40 µL) and the emulsion was stirred at 600 rpm for 48 h. UCLNP@SiO$_2$ were precipitated by adding 5.0 mL of acetone, collected by centrifugation (10,000 rpm, 10 min.) and washed three times with an ethanol-water mixture (1:1) by repeated centrifugation-redispersion cycles. Such coated particles were redispersed in 7.4 mL of water and stored in a head-over tumbling unit to prevent accelerating agglomeration.

8.3.5. Functionalization of UCLNP@SiO$_2$

Functionalization of UCLNPs prepared via thermal decomposition and coated with silica by the reverse microemulsion method was carried out by adding the appropriate silane during the coating procedure described above in section 8.3.4 after 24 h of stirring. The respective amounts which were added are summarized in Table 7. It is reported on pure silica NPs that an amount of the organosilane that is below 5% of the total amount of TEOS that was used for their synthesis is to saturate the surface with functionalities.[7] Hence, a somewhat higher amount of organosilane was added here.

Silane	Amount	Percentage of total TEOS
AzPTES	21.0 µmol, 5.0 µL	12%
AlkyneTES	16.0 µmol, 5.0 µL	9%
Silane-PEG-Mal	12.5 µmol, 25.0 mg	7%
APTES	23.0 µmol, 5.0 µL	13%

Table 7: List and amount of silanes used for surface functionalization of UCLNP@SiO$_2$.

8.3.6. Conjugation Reactions to Functionalized UCLNP@SiO$_2$

Click Reactions

Aqueous stock solutions of copper sulfate (0.1 M) and sodium ascorbate (0.1 M) were freshly prepared. The fluorophores bearing either an azido or an alkyne groups were dissolved in ethanol (1.0 mg/mL). 2.0 mL of UCLNP@SiO$_2$-N$_3$ or UCLNP@SiO$_2$-CCH prepared according to section 8.3.5 were combined with 250 L of the corresponding fluorophore solution for click reaction. After addition of 10 µL of the copper sulfate and 40 µL of the sodium ascorbate solution, the reaction mixtures were shaken at room temperature over night. The blank experiments were carried out in the same way without addition of the copper catalyst. The particles were collected by centrifugation (10,000 rpm, 10 min.) and washed five times with ethanol and one time with water by repeated centrifugation-washing cycles. The particles were redispersed in 2.0 mL of water and comparative fluorescence spectra were collected from 505 to 750 nm upon excitation at 440 nm.

Testing for Maleimide

HSA was labeled with FITC according to the following protocol: HSA (5.0 mg) was dissolved in 1 mL sodium bicarbonate buffer (BCB; 1 M, pH 9), FITC was dissolved in DMSO (1.0 mg in 100 µL). 5 µL of the FITC stock solution was added to the protein and the reaction mixture was shaken for 1.5 h at room temperature with protection from light. Gel filtration with Sephadex G-25 (www.gehealthcare.com) was used to remove unreacted dye molecules. The dimensions of the column applied were 10.0 cm (height) x 2.5 cm (diameter), the eluent was BCB (1 M, pH 9).

2.0 mL of UCLNP@SiO$_2$-PEG-Mal prepared according to section 8.3.5 were combined with 200 µL of the solution containing the labeled protein (see above). For the blank experiment, 2.0 mL of UCLNP@SiO$_2$ were used instead. The solutions were shaken over night at room temperature and centrifuged at 2,500 rpm for 10 min. Unbound protein was removed by

repeated centrifugation-washing cycles (four times, 2.0 mL BCB each). The particles were resuspended in 2.0 mL BCB and fluorescence spectra were collected from 510 to 750 nm upon excitation at 490 nm.

Staining Amino Groups with Py-1

2.0 mL of UCLNP@SiO$_2$-NH$_2$ in water prepared according to section 8.3.5 were centrifuged, the supernatant was discarded and the pellet was redispersed in 2.0 mL of ethanol. 1.0 mg of the fluorophore Py-1 was dissolved in 1.0 mL of methanol. The particles, 5 µL triethylamine and 50 µL of the fluorophore solution were combined and incubated at 37 °C under shaking. In the control experiment the same procedure was applied to UCLNP@SiO$_2$.

8.3.7. Encapsulation in Polystyrene

Encapsulation of multiple UCLNPs prepared via thermal decomposition was performed according to the protocol of Qian et al.[8] Different amounts of nanophosphors (see Table 8) were dispersed in a mixture of 0.5 mL of cyclohexane and 0.5 mL of freshly distilled styrene by sonication. In parallel, 0.0400 g SDS were dissolved in 25.0 mL of water in a 100.0 mL three-neck round bottom flask. The particle solution was added dropwise to the aqueous phase under stirring and the mixture was sonicated for 5 min. to form a milky emulsion. The flask was equipped with a gas inlet, a reflux condenser and a stopper. The reaction mixture was flushed with nitrogen for 10 min. Afterwards, K$_2$S$_2$O$_8$ (10.0 mg) was added and the emulsion was heated to 80 °C under moderate stirring. After the temperature was reached, the gas flow was turned off and heating was continued for 24 h. UCLNP@PS were collected by centrifugation (10,000 rpm, 10 min.) and washed three times with water by repeated centrifugation-redispersion cycles. The supernatant was carefully removed using a Pasteur pipette to avoid loss of the particles since the pellets were

partly not solid. The encapsulated nanophosphors were redispersed in water and stored in a head-over tumbling unit.

Amount of UCLNPs (MNPs)	Corresponding TEM picture
47.0 mg	Figure 4.19a
20.0 mg	Figure 4.18, Figure 4.19b
6.0 mg	Figure 4.19c
15.0 mg (5.0 mg)	Figure 4.20

Table 8: Amounts of nanophosphors used for the synthesis of UCLNP@PS and the corrsponding TEM pictures showing the respective capsules.

8.4. Sensing of Oxygen Based on Upconverting Luminescent Nanoparticles

8.4.1. Preparation of the Sensor Film

EC with an ethoxyl content of 46% was obtained from Sigma-Aldrich and used without further purification. The oxygen probe [Ir(C_S)$_2$(acac)] was kindly provided by Sergey Borisov.[9]

The sensor film was prepared by dissolving 1.0 mg [Ir(C_S)$_2$(acac)] in 200 µL of a solution of EC in THF (1.1wt%). NaYF$_4$:Yb,Tm NPs (1.0 mg) prepared via co-precipitation followed by thermal treatment (see section 8.2.1) were added, the resulting sensor cocktail was sonicated for 5 min. and then spread onto a glass plate. The solvent was left for evaporation under a hood upon which an orange-colored and slightly opaque sensor film was obtained.

8.4.2. Sensing of Oxygen

The sensor film was placed in a flow-through cell. A fiber optic cable conveyed either light from the 980 nm CW diode laser or from the xenon lamp of an Aminco Bowman luminescence spectrometer to the sensor layer. A second one served to collect luminescence emitted by the sensor

film and to convey it to the spectrofluorometer. Gas mixtures were prepared using a home-made computer controlled gas mixing device consisting of two Mass Flo-Controllers (MKS Instruments, Munich; www.mksinst.com) with gases from Linde (www.linde.de) and passed through the cell. Emission spectra were then recorded at an emission slit width of 5 nm, either by photoexcitation with the externally adjustable 980 nm fiber optic diode laser in case of upconversion, or with the 200 W xenon lamp of the spectrometer at 475 nm.

8.5. Polystyrene Nanoparticles for Luminescent Sensing of Oxygen

8.5.1. Loading of Polystyrene Nanoparticles with [Ru(dpp)$_3$]TMSPS$_2$

Amino-modified PSNPs (Polybead® Amino 0.10 Micron Microspheres; 2.6% Solids-Latex in water) were purchased from Polysciences, Inc. (www.polysciences.com). The oxygen probe [Ru(dpp)$_3$]TMSPS$_2$ was kindly provided by Dr. Matthias Stich. The soaking procedure was carried out in a modification of the protocol of Behnke et al.[10] 500 µL of the particle suspension were diluted with 2.0 mL of distilled water. The ruthenium(II) complex (1.0 mg) was dissolved in 100 µL of THF and the solution was added to the PSNPs. The mixture was respectively shaken and sonicated for 1 min. Afterwards, the THF was removed on a rotary evaporator (220 mbar, room temperature) over a period of 2 h while a total amount of 2.0 mL of distilled water was added once in a while. The solid content of the solution was determined to be 4.0 mg/mL. The number of PSNP(Ru) per volume was calculated according to the following equation[11]

$$\frac{NP}{mL} = \frac{6 \cdot 10^{12} \cdot solid\,(g/mL)}{\rho \cdot \pi \cdot d^3} \qquad \text{(Equation 3)}$$

with ρ(PS) = 1.05 g/mL and d = 0.085 µm yielding 1.2 · 10^{13} NP/mL. The yellow to orange suspension was stored at 4 °C.

8.5.2. One- and Two-Photon Laser Spectroscopy

Laser spectroscopy was performed on dye loaded PSNPs at the research group of Prof. John Lupton in the Physics Departement of the University of Regensburg. A Spectra-Physics 2045 E argon laser (www.newport.com) in combination with a Semrock LL01-488 (www.semrock.com) laser clean up filter was used for one-photon excitation at 488 nm (430 µW). For TPE at 830 nm a Spectra-Physics Tsunami mode-locked Ti:sapphire laser with a nominal repitition rate of 80 MHz was applied (130 mW). The average pulse duration of the latter was 75 fs which was determined with an APE PulseCheck autocorrelator (www.ape-berlin.de). The direction of polarization was vertical in the excitation and detection pathway with an optical path of 90°. The laser beam was directed through a half-micro quartz cuvette (fixed in a cuvette holder) closely above the bottom to which the particle solutions (400 µL each) were added with a syringe. Detection was focused to the laser beam with a Semi-Apochromat objective LUCPLFLN 40x from Olympus (www.olympusamerica.com). Luminescence emission was collected by an Acton SP2356 from Princeton Instruments (www.princetoninstruments.com) equipped with a grid (150 lines/mm) and a frame transfer CCD Pixis 400 (Princeton Instruments). The integration time was 20 s. A Semrock BLP01-488R long-pass filter was used in the detection path of the argon laser, a Semrock FF01-680/SP multiphoton short-pass emission filter for emission collection upon TPE.

Before the measurements, the aqueous solution containing 0.4wt% PSNP(Ru) of was degassed by bubbling a flow of argon through it for 1.5 h. Gas mixtures were prepared using the home-made computer controlled gas mixing device (see section 8.4.2). The gas flow was directed to the cuvette by a flexible tube and a cannula. The tube and the cannula were fixed in a way that the gas bubbles emerged closely above the laser beam in the solution without crossing it. A gas flow containing 20% oxygen and 80% argon was passed through the empty cuvette while 400 µL of the degassed particle solution were added by a syringe. After 5 min. of continuous bubbling a spectrum was resorded and the gas mixture was

changed to 40% oxygen and 60% argon. The next spectrum was collected again after 5 min. and the procedure was continued with gas mixtures of 60, 80 and 100% oxygen content before the particle solution was removed from the cuvette. The next series of measurement was performed with another 400 µL of the degassed solution.

8.6. Cell Experiments

All cell experiments were performed by members of the workgroup of Prof. Wegener, Institute of Analytical Chemsitry, Chemo- and Biosensors, University of Regensburg. Two different cell types were used in this work (NRK, MCF-7). The compositions of the respective culture media are listed below.

Culture medium NRK cells
Dulbecco's Modified Eagles Medium (DMEM)
+ NaHCO$_3$ (3.70 g/L)
+ D-glucose (4.50 g/L)
+ fetal calf serum (5% v/v)
+ L-glutamine (1 mM)
+ penicillin (0.10 g/L)
+ streptomycin (0.10 g/L)

Culture Medium MCF-7 cells
Earle's Minimal Essential Medium (MEM)
+ NaHCO$_3$ (2.20 g/L)
+ D-glucose (4.50 g/L)
+ fetal calf serum (10% v/v)
+ pyruvat (0.11 g/L)
+ glutamine (2 mM)
+ penicillin (0.10 g/L)
+ streptomycin (0.10 g/L)

8.6.1. AlamarBlue® Cell Viability Assay

The cells (NRK or MCF-7) were grown to confluence in the respective culture medium in 96-well microtiter plates (MTPs). The stock solutions of the NPs were diluted with medium. The culture medium was removed from the confluent cell layers and 200 µL of the particle solutions were added per well. For the control experiments 200 mL of pure medium was added instead. The plates were incubated at 37 °C with 5% CO_2 for 24 h. After 23 h 0.2% (v/v) Triton-X-100 were added to the wells for the negative control (0% viability). The liquid was again removed from the wells of the MTP and substituted for 200 µL of a solution containing 1/10 AlamarBlue® in PBS^{++} (phosphate buffered saline containing 0.90 mM $CaCl_2$, 0.52 mM $MgCl_2$ and 0.16 mM $MgSO_4$) with 1.0 g/L glucose. The plates were incubated at 37 °C without CO_2 for 12 h. The resulting fluorescence was read on a MTP reader (Fluoroskan Ascent from ThermoFischer Scientific; www.thermoscientific.com) using 544 nm excitation and 590 nm emission collection wavelength.

8.6.2. Loading of NRK Cells with Multicolor Upconverting Luminescent Nanoparticles

Incubation of NRK cells with the multicolor UCLNP@SiO$_2$ was carried out by Michaela Sperber. The NRK cells were cultured in DMEM according to a standard protocol and grown close to confluence in 8-well plates. The stock solutions of the silica coated nanophosphors (1.0 mg/mL; see section 8.3.4) were diluted with medium (1.0 to 100.0 µg/mL) and 200 µL of the particle solutions were added per well. After incubation at 37 °C with 5% CO_2 for 24 h, the cell layers were washed to remove excess particles and fixed with paraformaldehyde (4% v/v).

8.6.3. Integration of Polystyrene Nanoparticles in MCF-7 Spheroids

The formation of the spheroids and their loading with the dyed PSNPs (see section 8.5) was carried out by Christina Hupf according the following protocol which is also given in her master thesis.[12]

Culture flasks with a growth area of 12.5 cm^2 (4.0 mL of MEM, see above) were used for cultivation in an incubator at 37 °C with 5% CO_2. The cells were allowed to grow close to confluence before the culture medium was removed and 500 µL PBS⁻⁻ with 1 mM EDTA was added. After 2 min. at 37 °C the buffer was removed and substituted for 500 µL of a 0.25% trypsin-EDTA solution. After incubation for 3 to 4 min., detachment of the cells was controlled using an inverted microscope. Upon the addition of 2.0 mL of MEM the cell suspension was centrifuged (200 x g, 5 min) in sterile centrifuge tubes. The supernatant was removed and the pellet was resuspended in 2.0 mL MEM. The number of cells was determined using a Bürker hemacytometer. 3000 cells/well were seeded in agarose-coated 96-well MTPs (50 µL of a sterile 1.5% w/v agarose solution in serum free MCF-7 culture medium). Incubation with the NPs was done during spheroid formation and growth. Therefore, PSNP(Ru) (6 • 10^{10} NPs; calculated according to Equation 3) were added to the wells before the plate was sealed with parafilm and incubated at 37 °C under orbital shaking for 4 h at 120 rpm and further over night at 50 rpm. Afterwards, the plate was transferred to the usual incubator unit. In the ideal case one spheroid grows in each well.

8.7. References

1   Yi G, Lu H, Zhao S, Ge Y, Yang W, Chen D, Guo L-H (2004) *Synthesis, Characterization, and Biological Application of Size-Controlled Nanocrystalline NaYF$_4$:Yb,Er Infrared-to-Visible Up-Conversion Phosphors.* Nano Lett 4:2191-2196
2   Li Z, Zhang Y (2008) *An efficient and user-friendly method for the synthesis of hexagonal-phase NaYF$_4$:Yb, Er/Tm nanocrystals with controllable shape and upconversion fluorescence.* Nanotechnology 19: 345606

3   Chen G, Liu H, Somesfalean G, Liang H, Zhang Z (2009) *Upconversion emission tuning from green to red in Yb^{3+}/Ho^{3+}-codoped NaYF$_4$ nanocrystals by tridoping with Ce^{3+} ions.* Nanotechnology 20:385704

4   Guo H, Li Z, Quian H, Hu Y, Muhammad IN (2010) *Seed-mediated synthesis of NaYF$_4$:Yb,Er/NaGdF$_4$ nanocrystals with improved upconversion fluorescence and MR relaxivity.* Nanotechnology 21:125602

5   Lattuada M, Hatton TA (2007) *Functionalization of Monodisperse Magnetic Nanoparticles.* Langmuir 23:2158-2168

6   Jalil RA, Zhang Y (2008) *Biocompatibility of silica coated NaYF$_4$ upconversion fluorescent nanocrystals.* Biomaterials 29:4122-4128

7   Deng G,Markowitz MA, Kust PR, Gaber BP (2000) *Control of Surface Expression of Functional Groups on Silica Particles.* Mat Sci Eng C 11:165-172

8   Qian H, Li Z, Zhang Y (2008) *Multicolor polystyrene nanospheres tagged with up-conversion fluorescent nanocrystals.* Nanotechnology 19:255601

9   Borisov SM, Klimant I (2007) *Ultrabright Oxygen Optodes Based on Cyclometalated Iridium (III) Coumarin Complexes.* Anal Chem 79:7501-7509

10   Behnke T, Würth C, Hoffmann K, Hübner M, Panne U, Resch-Genger U (2011) *Encapsulation of Hydrophobic Dyes in Polystyrene Micro- and Nanoparticles via Swelling Procedures.* J Fluoresc 21:937-944

11   http://tools.invitrogen.com/content/sfs/manuals/mp05000.pdf

12   Hupf C (2012) *Impact of Nanoparticles on Two- and Three-Dimensional Cell Cultures.* Master Thesis, University of Regensburg

9.   Summary

The thesis describes the synthesis, characterization and modification of NPs that are qualified for imaging and sensing using NIR excitation. One particle type that was investigated is nanosized RE doped $NaYF_4$ (UCLNPs). Excitation with a CW diode laser results in VIS emission.

Green and blue emitting UCLNPs were synthesized either by co-precipitation followed by thermal treatment or by thermal decomposition. The former yielded particles in sizes ranging from 80 to 120 nm in a mixture of α- and β-phase $NaYF_4$. The synthesis was straightforward but lacks homogeneity of the particles and reproducibility. These UCLNPs were well dispersible in aqueous solutions. The second method, in contrast, produced smaller (25 to 40 nm) and well uniform RE-doped $NaYF_4$ NPs with a narrow size distribution ($\pm$ 5 nm) and a pure hexagonal crystal lattice. The particles were highly hydrophobic due to surface ligand molecules and further modifications were necessary for applications in aqueous media.

Diverse surface modifications were performed on UCLNPs. Particles obtained from both syntheses were coated with silica by different methods to render them either water-dispersible and/ or biocompatible and primed for surface functionalization. The latter was demonstrated for silica coated UCLNPs that were synthesized by thermal decomposition. They were successfully functionalized with azido, alkyne, maleimide and amino groups. The nanophosphors obtained from thermal decomposition were subjected to further modifications. Coating with a shell of $NaYF_4$ efficiently enhanced their brightness and hampered quenching by solvent molecules. LE reactions with carboxylic acids were applied to tune their dispersibility. Further, capsules containing multiple UCLNPs were prepared by entrapment in a matrix of PS. Thus a pool of particles that exhibit various characteristics was generated.

Multicolor UCLNPs for imaging applications were synthesized via thermal decomposition by selective damping of emission peaks. The particles featured narrow emission bands upon excitation with a 980 nm CW diode laser. These were well separated in three regions of the VIS spectrum (red, green and blue). The particles could be identified by their RGB-codes what was demonstrated for five types of nanocrystals that obviously emitted different colors. The approach can be further extended enabling multiplexes ratiometric encoding. Coating with silica rendered the NPs water dispersible and well biocompatible turning them into promising candidates for cell tracking.

In addition, luminescent sensing of oxygen using a quenchable probe and UCLNPs was presented by combining both components in a gas permeable sensor film. The UCLNPs acted as nanolamps upon excitation in the NIR and their VIS luminescence excited the dye molecules. Their emission, in turn, is dynamically and fully reversible quenched by oxygen. Thus the first sensor for oxygen that can be excited with CW NIR light was designed.

The second material that was dealt with in this work are amino-modified PSNPs that were loaded with the oxygen sensitive dye [Ru(dpp)$_3$]TMSPS$_2$. It was demonstrated that these particles are capable of sensing oxygen in aqueous solution upon TPE with a short-pulsed NIR laser. The PSNP(Ru) are good candidates for the determination of oxygen distribution in tissue. Imaging of oxygen inside MCS, a tumor model system, unfortunately failed necessitating further investigations on these PS nanosensors.

10. Zusammenfassung

Innerhalb der Arbeit wurden Nanopartikel (NP) entwickelt, die Bildgebung und Sensorik basierend auf Anregung mit kurzwelliger Infrarotstrahlung (NIR) ermöglichen. Zum einen wurden Partikel aus $NaYF_4$, dotiert mit Ionen der seltenen Erden untersucht (UCLNP). Diese können mit einem kontinuierlichen NIR Laser angeregt werden, woraufhin sie im sichtbaren Spektralbereich emittieren (Upconversion).

Grün oder blau lumineszierende Partikel wurden mit Hilfe zweier Methoden synthetisiert. Durch Co-Präzipitation und anschließende thermische Behandlung entstanden NP in einer Größe von 80 bis 120 nm und einer gemischten Kristallstruktur aus α- und β-$NaYF_4$. Diese Methode ist unkompliziert, liefert aber kein homogenes Material und ist schwer reproduzierbar. Die so erhaltenen UCLNP sind in Wasser gut dispergierbar. Als zweite Synthesemethode wurde die thermische Zersetzung angewandt. Dabei entstanden viel kleinere (25 bis 45 nm) und einheitliche (± 5 nm) $NaYF_4$ Partikel mit hexagonaler Kristallstruktur. Aufgrund von Ligandmolekülen, die an die Oberfläche koordiniert sind, hatten diese Partikel sehr hyrophobe Eigenschaften und konnten nur nach weiterer Modifikation der Oberfläche in wässrigen Lösungen angewendet werden.

Diverse Oberflächenmodifikationen wurden an den Partikeln durchgeführt. UCLNP aus beiden Synthesen wurden durch verschiedene Verfahren mit Silica ummantelt um sie in Wasser dispergierbar und/ oder biokompatibel zu machen, und für weitere Oberflächenfunktionalisierungen vorzubereiten. Letzteres wurde für Silica ummantelte NP, die durch thermische Zersetzung hergestellt wurden, demonstriert. Azid-, Alkin-, Maleimid- und Aminofunktionalitäten konnten auf ihrer Silica-Oberfläche nachgewiesen werden. Durch thermische Zersetzung gewonnene UCLNP wurden noch weiteren Modifikationen unterworfen. Eine Hülle aus $NaYF_4$ verstärkte ihre Emisson und unterdrückte gleichzeitig ein Löschen der Lumineszenz durch Lösungsmittelmoleküle. Ligand-Austauschreaktionen mit Carbonsäuren ermöglichten Dispergierbarkeit in unterschiedlichen

Medien. Zudem wurden Kapseln, die gleichzeitig mehrere UCLNP enthalten, durch Einschluss in eine Matrix aus Polystyrol hergestellt. Somit wurde eine Auswahl von Partikeln mit unterschiedlichen Eigenschaften generiert.

Für bildgebende Verfahren wurden durch thermische Zersetzung UCLNP synthetisiert, die Licht verschiedener Farben emittieren. Dies wurde durch selektive Abschwächung bestimmter Emissionswellenlängen erreicht. Die Emissionsbanden dieser Partikel nach NIR Anregung sind schmalbandig und können sehr gut drei Bereichen des sichtbaren Spektrums (rot, grün und blau) zugeordnet werden. Diese NP besitzen demnach RGB-Codes über die sie eindeutig identifizierbar sind. Das wurde hier für fünf augenscheinlich verschiedenfarbig lumineszierende Typen von UCLNP demonstriert. Das Prinzip kann aber auf eine Vielzahl unterschiedlicher Codes ausgeweitet werden und macht somit ratiometische Verschlüsselung möglich. Eine Ummantelung mit Silica ermöglichte es die Partikel in Wasser zu überführen und es konnte gute Biokompatibilität nachgewiesen werden. Das macht sie zu einem vielversprechenden Material für Zell-Verfolgung und -Zuordnung.

Zusätzlich wurden UCLNP mit einer Sauerstoffsonde durch Einbettung in einen gas-permeablen Film zu einem optischen Sensor kombiniert. Die Partikel fungierten als Nanolampen, die nach Anregung im NIR im sichtbaren Spektralbereich emittierten und ihrerseits die Farbstoffmoleküle anregten. Deren Emission wurde dynamisch und vollständig reversibel durch Sauerstoff gelöscht. Somit wurde der erste optische Sauerstoffsensor präsentiert, der auf Anregung mit kontinuierlichem NIR Licht basiert.

Das zweite Material das in dieser Arbeit untersucht wurde sind aminomodifizierte PSNP, die mit dem sauerstoffsensitiven Komplex [Ru(dpp)$_3$]TMSPS$_2$ dotiert wurden. Es konnte erstmals gezeigt werden, dass mit diesen Partikeln Sauerstoffsensorik in wässrigen Lösungen basierend auf Zwei-Photonen-Anregung durch einen gepulsten Laser

möglich ist. Diese NP sind prinzipiell geeignet für die Bildgebung der Sauerstoffverteilung in Geweben. Der Versuch Sauerstoff im Inneren von multizellulären Sphäroiden, einem Tumor-Modellsystem, zu messen schlug leider fehl. An dieser Art von Nanosensoren sind daher weitere Untersuchungen   nötig.

11. Curriculum Vitae

PERSONAL DATA

Name	Daniela Eva Achatz
Date of Birth	12.04.1983
Place of Birth	Bogen

EDUCATION

09/1989 – 07/1993	Grundschule Ascha
08/1993 – 06/2002	Veit-Höser-Gymnasium Bogen
06/2002	Graduation (Abitur)

STUDIES

10/2003 – 03/2005	Studies of biology at the Universität of Regensburg
04/2005 – 12/2007	Studies of chemistry at the Universität of Regensburg
01/2008 – 09/2008	Diploma thesis at the University of Regensburg (Supervisor Prof. O. S. Wolfbeis); "*Fluorescent Silica Nanoparticles for Click Labeling of Proteins*"
11/2008 – present	Ph. D. thesis at the University of Regensburg (Supervisor Prof. O. S. Wolfbeis)
07/2010	Visiting scientist at the Institut of Biotechnology, University of Turku, Finland

PUBLICATIONS

P. Kele, G. Mezó, D. E. Achatz, O. S. Wolfbeis, **Dual Labeling of Biomolecules by Using Click Chemistry: A Sequential Approach**, *Angew. Chem. Int. Ed.,* 2009, 48, 344-347

D. E. Achatz, G. Mezó, P. Kele, O. S. Wolfbeis, **Probing the Activity of Matrix Metalloproteinase II with a Sequentially Click-Labeled Silica Nanoparticle FRET Probe**, *ChemBioChem*, 2009, 10, 2316-2320

L.-N. Sun, H. Peng, M. I. J. Stich, D. E. Achatz, O. S. Wolfbeis, **pH sensor based on upconverting luminescent lanthanide nanorods**, *Chem. Commun.*, 2009, 5000-5002

H. S. Mader, M. Link, D. E. Achatz, K. Uhlmann, X. Li, O. S. Wolfbeis, **Surface-Modified Upconverting Microparticles and Nanoparticles for Use in Click-Chemistries**, *Chem.-Eur. J.*, 2010, 16, 5416-5424

D. E. Achatz, F. J. Heiligtag, X. Li, M. Link, O. S. Wolfbeis, **Colloidal silica nanoparticles for use in click chemistry-based conjugations and fluorescent affinity assays**, *Sens. Actuators B*, 2010, 150, 211-219

M. Link, P. Kele, D. E. Achatz, O. S. Wolfbeis, **Brightly fluorescent purple and blue labels for amines and proteins**, *Bioorg. Med. Chem. Lett.*, 2011, 21, 5538-5542

D. E. Achatz, R. Ali, O. S. Wolfbeis, **Luminescent Chemical Sensing, Biosensing and Screening using Upconverting Nanoparticles**, *Top. Curr. Chem.*, 2011, 300, 29-51

M. M. Rubner, D. E. Achatz, H. S. Mader, J. A. Stolwijk, J. Wegener, G. S. Harms, O. S. Wolfbeis, H-A. Wagenknecht **DNA " Nanolamps": "Clicked" DNA Conjugates with Photon Upconverting Nanoparticles as Highly Emissive Biomaterial**, *ChemPlusChem*, 2012, 77, 129-134

Eidesstattliche Erklärung

Ich erkläre hiermit an Eides statt, dass ich die vorliegende Arbeit ohne unzulässige Hilfe Dritter und ohne Benutzung anderer als der angegebenen Hilfsmittel angefertigt habe; die aus anderen Quellen direkt oder indirekt übernommenen Daten und Konzepte sind unter Angabe des Literaturzitats gekennzeichnet. Weitere Personen waren an der inhaltlich materiellen Herstellung der vorliegenden Arbeit nicht beteiligt. Insbesondere habe ich hierfür nicht die entgeltliche Hilfe eines Promotionsberaters oder anderer Personen in Anspruch genommen. Niemand hat von mir weder unmittelbar noch mittelbar geldwerte Leistungen für Arbeiten erhalten, die im Zusammenhang mit dem Inhalt der vorgelegten Dissertation stehen. Diese Arbeit wurde bisher weder im In- noch im Ausland in gleicher oder ähnlicher Form einer anderen Prüfungsbehörde vorgelegt.

Ort, Datum   Unterschrift